TÉCNICO LISBOA

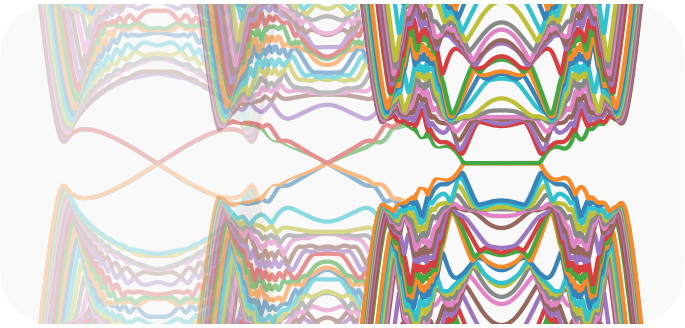

Quasi-Disorder Effects in Topological Superconductors

Maria Francisca Galego Fonseca de Alvarez Madeira

Thesis to obtain the Master of Science Degree in

Engineering Physics

Supervisor: Prof. Pedro Domingos Santos do Sacramento

Examination Committee

Chairperson: Prof. Pedro Miguel Félix Brogueira
Supervisor: Prof. Pedro Domingos Santos do Sacramento
Members of the Committee: Prof. Pedro José Gonçalves Ribeiro
Prof. Eduardo Filipe Vieira De Castro

May 2022

In loving memory of my dear friend Susana.

Acknowledgments

First I want to thank my supervisor, for all the guidance, the patience, for always being available, and for teaching me a lot in these last years. I also thank him for suggesting such an interesting research topic and for guiding me through it with great dedication and enthusiasm.

I also want to thank my family, for their unconditional support, for always allowing and supporting me in pursuing my goals, and for being so understanding during this whole journey. I also thank my boyfriend and my friends - their presence and support was beyond indispensable throughout this work.

This work has been partially supported by *Fundação para a Ciência e Tecnologia* under the project (1801P.01102.1.01) QMSP2021 - VeraoComCiencia CEFEMA - IST-ID.

Resumo

Estudamos os efeitos da desordem de Aubry-André e desordem de Anderson para um modelo de um supercondutor topológico bidimensional com um campo magnético externo. São estudados os casos de um supercondutor de emparelhamento tipo p e um supercondutor não centrossimétrico com mistura de emparelhamentos de tipo p e s e com acoplamento spin-órbita de Rashba. Revemos as propriedades topológicas do sistema sem desordem, que dependem da direção do campo magnético (perpendicular ou paralelo ao plano do supercondutor). O sistema desordenado é estudado tanto no espaço real como num espaço misto. Quando o campo magnético é paralelo, estudamos os efeitos de quasi-desordem e desordem, aplicada tanto nas fronteiras como no interior do supercondutor, e discutimos os seus efeitos na localização do sistema, densidade de estados e nas funções de onda, numa abordagem no espaço real. Ainda no espaço real mostramos que, para um campo magnético perpendicular, a introdução de quasi-desordem leva ao aparecimento de novas regiões topológicas, caracterizadas por um valor inteiro do número de Chern. Numa abordagem no espaço misto, identificamos novos regimes com o aparecimento de novas bandas planas de Majorana e também novos estados de fronteira de Majorana unidirecionais, com a introdução de quasi-desordem. Mostramos que as bandas planas de Majorana têm uma fase Berry quantizada de π e indentificamo-la como um invariante topológico. Duas transições topológicas são identificadas e os valores dos expoentes críticos z e ν são obtidos. A natureza fractal dos estados é discutida tanto para desordem de Anderson como para desordem de Aubry-André.

Palavras-chave: Quasi-desordem, supercondutor topológico, bandas planas de Majorana, número de Chern, expoentes críticos, multifractalidade

Abstract

We study the effects of Aubry-André disorder and Anderson disorder in a model of a two-dimensional topological superconductor with an applied external magnetic field. The cases of a p-wave superconductor and a noncentrosymmetric superconductor with mixed p- and s-wave pairing and Rashba spin orbit coupling are studied. We review the topological properties of the clean system, which depend on whether the applied magnetic field is perpendicular or parallel to the plane of the superconductor. The disordered system is studied both in real space and in a mixed space. When the applied magnetic field is parallel, we study both edge and bulk quasi-disorder and Anderson disorder and discuss the effects on the localization of the system, density of states, and direct effect on the wave functions, on a real space approach. Also on a real space approach we show that, for a perpendicular magnetic field, the introduction of quasi-disorder leads to the appearance of new topological regimes, characterized by an integer value of the Chern number. In a mixed space approach we identify new regimes with the appearance of new Majorana flat bands and also new unidirectional Majorana edge states, as quasi-disorder is introduced. We show the Majorana flat bands have a quantized Berry phase of π and identify this as a topological invariant. Two topological transitions are identified and the values of the critical exponents z and ν are obtained. The fractal nature of the eigenstates is discussed both for Anderson disorder and Aubry-André disorder.

Keywords: Quasi-disorder, topological superconductor, Majorana flat bands, Chern number, critical exponents, multifractality

Contents

Acknowledgments v
Resumo vii
Abstract ix
List of Tables xiii
List of Figures xiii
List of Abbreviations xxi

1 Introduction **1**
1.1 State of the art 1
1.2 Thesis outline 3

2 Fundamental Concepts **5**
2.1 Topology in condensed matter physics 5
2.1.1 Berry Phase 5
2.1.2 Chern Number 6
2.1.3 Edge states and the bulk-edge correspondence 7
2.1.4 The SSH model and the winding number 7
2.2 Superconductivity 9
2.2.1 Bogoliubov-de Gennes equations 9
2.2.2 Superconducting pairing term 10
2.2.3 Particle-Hole Symmetry and Majorana fermions 11
2.2.4 The Kitaev toy model 11
2.3 Disordered systems 12
2.3.1 Participation Ratio 13
2.3.2 Multifractality of wave functions 14
2.3.3 Scaling properties near a phase transition 14

3 Clean two-dimensional topological superconductor **17**
3.1 Model Hamiltonian 17
3.2 Superconductor under a perpendicular magnetic field 19
3.3 Superconductor under a parallel magnetic field 23
3.3.1 Winding Number and Majorana Flat Bands 24
3.3.2 Domain of Flat Band Existence 26
3.3.3 Unidirectional Majorana Edge States 28

4 Disordered two-dimensional topological superconductor **31**
4.1 Quasi-disorder and Anderson disorder effects in real space 32
4.1.1 Edge disorder 32
4.1.2 Bulk disorder 37
4.1.3 Quasi-disorder induced topology: Chern number 47
4.2 Quasi-disorder and Anderson disorder effects in mixed space 53
4.2.1 Energy spectra evolution and density of states 53
4.2.2 Quasi-disorder induced Majorana Flat Bands 59
4.2.3 Scaling of the density of states: critical exponents 62
4.2.4 Fractal analysis 68

5 Discussion, conclusions and future work **73**

Bibliography **77**

A Symmetry Classification of Topological Systems **85**

B Numerical Methods **87**
B.1 Recursive Green's Function 87
B.2 Chern Number in real space 89

C Evolution of energy spectra with a quasi-periodic potential **93**

List of Tables

4.1 Values of the critical exponents $\lambda_{C,1}$ and $\lambda_{C,2}$ for the system sizes $\{76, 100, 175, 200, 400, 800\}$. 61

4.2 Values of z and ν obtained numerically for the topological transition in the clean case. . . 64

4.3 Values of z and ν obtained numerically for the topological transitions in the disordered case. 67

A.1 The symmetry classes of single particle Hamiltonians, in terms of time reversal-symmetry, particle-hole symmetry, chiral symmetry, and number of dimensions. The presence of symmetry is denoted by "+1" or "-1" depending on whether the symmetry operator squares to +1 or -1. "0" denotes the absence of symmetry. The last three columns indicate the type of topological invariant that characterizes the system with regards to the dimension d. Table taken from [91]. 85

List of Figures

2.1 Top: Dispersion relations for different values of t_0 and t_1: a) $t_0 = 1, t_1 = 0.6$; b) $t_0 = t_1 = 1$; c) $t_0 = 0.6, t_1 = 1$. Bottom: The corresponding paths of the endpoints of the vectors $\mathbf{h}(k)$ as k sweeps the Brillouin zone. Image adapted from [65]. 8

3.1 Scheme of a two-dimensional system in a cylinder geometry with a) an applied perpendicular magnetic field, b) an applied parallel magnetic field. 18

3.2 Phase diagram for the Chern number as a function of μ and B_z, with $t = 1$ and a) $\Delta_s = 0$, a) $\Delta_s = 0.3$. (Note that the gap-closing points are independent of d, but the phase diagram is only valid are in a regime where $|d| > |\Delta_s|$.) 20

3.3 Phase diagram for the winding numbers $I(k_y = 0, \pi)$ as a function of μ and B_z, with $t = 1$ and $\Delta_s = 0$ and for $d > 0$. 21

3.4 Phase diagram for ($B_z, B_y > 0$) for the Chern number obtained numerically at $\mu = 0$, $\mu = 1$ and $\mu = -3.5$ for $\Delta_s = 0$. 22

3.5 Bulk energy spectrum. 23

3.6 Energy spectrum evolution for a system with 76 sites in y and edges at $y = 0$ and $y = 75$ for different values of B_y vs. absolute value of the winding number $\mathcal{W}$ and normalized Berry phase $\gamma/(2\pi)$ as a function of k_x. The values of the parameters are $t = 1$, $d = t/6$, $\mu = 3d - 4t$ and $B_y = d$ (left), $B_y = 2d$ (middle), $B_y = 3d$ (right). 25

3.7 a) Domain of MFBs (shaded region) for B_y vs. k_x for the parameter values $t = 1$, $d = t/6$, $\mu = -3.5$. b) Closeup of a) in the region $B_y \in [-1, 1]$. The three dashed lines represent the values $B_y = d$ (blue), $B_y = 2d$ (red) and $B_y = 3d$ (red) which correspond to the values of B_y of the energy spectra presented in figure 3.6. 27

3.8 Domain of MFBs (shaded region) for B_y vs. k_x. The graphs a), b) and c) have $B_x = 0$ while the graphs d), e) and f) have $B_x \neq 0$, represented by red dashed lines. The values of the parameters are a) $t = 1, \mu = 3, d = 0.2, B_x = 0$. b) $t = 1, \mu = 0, d = 0.3, B_x = 0$. c) $t = 1, \mu = -2, d = 0.1, B_x = 0$; d), e) and f) are the same as a), b) and c), respectively, except for d) $B_x = 0.7$, e) $B_x = 1$, f)$B_x = 1.3$. 28

3.9 Left: Energy spectrum for a system with 76 sites in y and edges at $y = 0$ and $y = 75$ for the parameter values $t = 1$, $d = t/6$, $\mu = 3d - 4t$, $By = 4d$, $\alpha = 0.2d$. Right: representation of the unidirectional edge modes in the superconductor with a cylindrical geometry. 29

4.1 Typical edge states of the clean system, at $t = 1$, $d = t/6$, $\mu = -3.5$ and a) $B_y = 0.5d$, b) $B_y = 3.5d$, c) $B_y = 4d$, $\alpha = 0.2d, \Delta_s = 0.3d$. 32

4.2 a) IPR averaged over the lowest 10 positive energy states and highest 10 negative energy states, vs. Anderson edge disorder strength λ (Type I). b) IPR averaged over the remaining states vs. disorder strength λ. The results are averaged over 10 disorder configurations. 33

4.3 Disordered edge states for $t = 1$, $d = t/6$, $\mu = -3.5$, $B_y = 4d$, $\alpha = 0.2d$ and $\Delta_s = 0.3d$, subject to Anderson edge disorder. The wavefunctions have energies a) $E = 8 \times 10^{-4}$, b) $E = 8 \times 10^{-4}$ and c) $E = 9 \times 10^{-4}$. 34

4.4 Disordered edge states for $t = 1$, $d = t/6$, $\mu = -3.5$, $B_y = 4d$, $\alpha = 0.2d$ and $\Delta_s = 0.3d$, subject to Anderson edge disorder. Here the states are shown at fixed values of x, perpendicularly to the direction of the edges, showing the impact of edge disorder on the bulk layers. 34

4.5 a) IPR averaged over the lowest 10 positive energy states and highest 10 negative energy states, vs. Aubry-André edge disorder strength λ (Type II). b) IPR averaged over the remaining states vs. disorder strength λ. The results are averaged over 10 disorder configurations. 35

4.6 Disordered edge states for $t = 1$, $d = t/6$, $\mu = -3.5$, $B_y = 4d$, $\alpha = 0.2d$ and $\Delta_s = 0.3d$ subject to Aubry-André edge disorder. The wavefunctions have energies a) $E = 2.8 \times 10^{-3}$, b) $E = 1.7 \times 10^{-3}$, c) $E = 9 \times 10^{-4}$. 36

4.7 Disordered edge states for $t = 1$, $d = t/6$, $\mu = -3.5$, $B_y = 4d$, $\alpha = 0.2d$ and $\Delta_s = 0.3d$, subject to Aubry-André edge disorder. Here the states are shown at fixed values of x, perpendicularly to the direction of the edges, showing the impact of edge disorder on the bulk layers. 36

4.8 a) IPR averaged over the lowest 10 positive energy states and highest 10 negative energy states, vs. Anderson disorder strength λ (Type III). b) IPR averaged over the remaining states vs. disorder strength λ. The results are averaged over 10 disorder configurations. . 38

4.9 Disordered states for $t = 1$, $d = t/6$, $\mu = -3.5$, $B_y = 4d$, $\alpha = 0.2d$ and $\Delta_s = 0.3d$ subject to Anderson disorder (Type III). The wavefunctions have energies a) $E = 2.86 \times 10^{-4}$, b) $E = 4.1 \times 10^{-5}$ and c) $E = 2.91 \times 10^{-3}$. 38

4.10 Total density of states, for the energy range $E \in [-4.5, 4.5]$ obtained with the Recursive Green's Function method for several values of Anderson disorder strength λ (Type III). The values of the parameters are a) $B_y = 0.5d$, b) $B_y = 3.5d$, c) $B_y = 4d, \alpha = 0.2d, \Delta_s = 0.3d$. The DOS is obtained for an average of 20 initial random states and disorder configurations, and for a value of $\eta = 0.08$ (equation B.11). 39

4.11 a) IPR averaged over the lowest 10 positive energy states and highest 10 negative energy states, vs. Anderson disorder strength λ (Type IV). b) IPR averaged over the remaining states vs. disorder strength λ. The results are averaged over 10 disorder configurations. . 39

4.12 a) Average IPR of the whole system for Anderson disorder and fits of functions of the form $y = C_1 \exp\{C_2 x\}$ in the range $\lambda \in [1.5, 3]$. b) Average IPR of the whole system for Anderson disorder with x periodicity and fits of functions of the form $y = C_1 x + C_2$ in the range $\lambda \in [0.5, 3]$. 40

4.13 Total density of states of the system, for the energy range $E \in [-4.5, 4.5]$ obtained with the Recursive Green's Function method for several values of Anderson disorder strength λ (Type IV). The values of the parameters are a) $B_y = 0.5d$, b) $B_y = 3.5d$, c) $B_y = 4d, \alpha = 0.2d, \Delta_s = 0.3d$. The DOS is obtained for an average of 20 initial random states and disorder configurations, and for a value of $\eta = 0.08$ (equation B.11). 41

4.14 Disordered states for $t = 1$, $d = t/6$, $\mu = -3.5$ and $B_y = 3.5d$, subject to Anderson disorder with $x-$periodicity (Type IV). The wavefunctions have energies a) $E = 3.07\times10^{-3}$, b) $E = 4.79 \times 10^{-3}$ and c) $E = 2.61 \times 10^{-3}$. 41

4.15 a) IPR averaged over the first 10 positive energy states and last 10 negative energy states, vs. quasi-disorder strength λ (Type V). b) IPR averaged over the remaining states vs. quasi-disorder strength λ. The results are averaged over 10 disorder configurations. . . . 42

4.16 Total density of states of the system, for the energy range $E \in [-0.5, 0.5]$, obtained with the Recursive Green's Function method for several values of λ. Each column concerns the case of a) Anderson disorder (Type III), b) Anderson disorder with x periodicity (Type IV) and c) Aubry-André disorder (Type V), and each row concerns the parameter values (1) $B_y = 0.5d$, (2) $B_y = 3.5d$, (3) $B_y = 4d, \alpha = 0.2d, \Delta_s = 0.3d$. The DOS is obtained for an average of 20 initial random states and disorder configurations, and for a value of $\eta = 0.02$ (equation B.11). 43

4.17 Total density of states of the system, for the energy range $E \in [-4.5, 4.5]$ obtained with the Recursive Green's Function method for several values of Aubry-André disorder strength λ (Type V). The values of the parameters are a) $B_y = 0.5d$, b) $B_y = 3.5d$, c) $B_y = 4d, \alpha = 0.2d, \Delta_s = 0.3d$. The DOS is obtained for an average of 20 initial random states and disorder configurations, and for a value of $\eta = 0.08$ (equation B.11). 44

4.18 Disordered states for $t = 1$, $d = t/6$, $\mu = -3.5$ and $B_y = 0.5d$, subject to Aubry-André disorder (Type V). The wavefunctions have energies a) $E = 5.44\times10^{-3}$, b) $E = 1.34\times10^{-3}$ and c) $E = 3.23 \times 10^{-2}$. 44

4.19 First positive energy state for a system of size 41×41 vs. disorder strength of the quasi-periodic potential with $\phi = 0$, for the system with open boundary conditions along y (green) and periodic conditions along y (black). The values of the parameters are $t = 1$, $d = t/6$, $\mu = -3.5$ and $B_y = 0.5d$. 45

4.20 Example of wavefunctions with Aubry-André disorder (Type V), at a fixed value $x = 8$, for the system of size 41×41. a) Extended wavefunction at $E = 0.28$, $\lambda = 0$, b) critical wavefunction at $E = 0.51$, $\lambda = 1.6$, c) localized wavefunction at $E = 0.32$, $\lambda = 2.5$. 46

4.21 Phase diagrams of a system with 20x20 sites, indexed by the Chern number C, for several values of disorder strength λ and perpendicular magnetic field B_z. Obtained for the average over 10 disorder configurations. The values of the parameters are $t = 1$, $d = 0.6$ and $\mu = 0$ (top), $d = 0.6$ and $\mu = 1$ (middle), $d = 1/6$ and $\mu = 3d - 4t = -3.5$ (bottom). . 47

4.22 Phase diagram of a system with 40x40 sites, indexed by the Chern number C, for several values of disorder strength λ and perpendicular magnetic field B_z. Obtained for the average over 10 disorder configurations. The values of the parameters are $t = 1$, $d = t/6$, $\mu = -3.5$. 48

4.23 Phase diagrams of a system with 20x20 sites, indexed by the Chern number C, for a) Anderson disorder (without x periodicity) with $t = 1$, $d = 0.6$, $\mu = 1$ and b) Aubry-André disorder with $t = 1$, $d = t/6$, $\mu = 4.5$. 49

4.24 Values of the Chern number C vs. quasi-disorder strength λ for the system sizes 20×20, 30×30 and 41×41 and for the parameter values $t = 1$, $\mu = 0$, $d = 0.6$, $B_z = 0.4$ (left), $\mu = 1$, $d = 0.6$, $B_z = 1.1$ (middle) and $\mu = -3.5$, $d = 1/6$, $B_z = 0.3$ (right). The results were averaged over 10 disorder configurations (10 random values of ϕ in the quasi-periodic potential). 50

4.25 In-gap states at the topological phase with $C = -1$ for $\mu = 1$, $d = 0.6$, $B_z = 1.1$, and $\lambda = 1.1, \phi = 0$ in the quasi-periodic Aubry-André potential. The left panel (1) shows a state at $E = -4.45 \times 10^{-2}$ (top) and a one-dimensional cut of the wavefunction at $x = 20$ (bottom). The right panel (2) shows a state at $E = 4.1 \times 10^{-6}$ (top) and a one-dimensional cut of the wavefunction at $x = 20$ (bottom). The middle panel locates the value of λ within the topological phase (top) and locates the states (1) and (2) in the energy spectrum of the system (bottom). 51

4.26 In-gap states at the topological phase with $C = -1$ for $\mu = -3.5$, $d = 1/6$, $B_z = 0.3$, and $\lambda = 1.05, \phi = 0$ in the quasi-periodic Aubry-André potential. The left panel (1) shows a state at $E = 10^{-3}$ (top) and a one-dimensional cut of the wavefunction at $x = 20$ (bottom). The right panel (2) shows a state at $E = 5 \times 10^{-2}$ (top) and a one-dimensional cut of the wavefunction at $x = 20$ (bottom). The middle panel locates the value of λ within the topological phase (top) and locates the states (1) and (2) in the energy spectrum of the system (bottom). 51

4.27 First positive energy state for a system of size 41×41 vs. disorder strength of the quasi-periodic potential, for the case $\phi = 0$, and for the parameters $\mu = -3.5$, $d = 1/6$, and $B_z = 0.3$ The phases with $C = 0$ are represented in green, and the phases with $C = -1$ are represented in blue. 52

4.28 Energy spectra evolution with Anderson disorder for a) $B_y = 0.5d$, b) $B_y = d$, c) $B_y = d$, $\alpha = 0.2d$, $\Delta_s = 0.5d$, d) $B_y = 4d$, $\alpha = 0.2d$, $\Delta_s = 0.3d$. 54

4.29 Density of states evolution with Anderson disorder for $E \in [-0.4, 0.4]$, for the parameter values a) $B_y = 0.5d$, b) $B_y = d$, c) $B_y = d$, $\alpha = 0.2d$, $\Delta_s = 0.5d$, d) $B_y = 4d$, $\alpha = 0.2d$, $\Delta_s = 0.3d$. 55

4.30 Energy spectra evolution with Aubry-André disorder a) $B_y = 0.5d$, b) $B_y = d$, c) $B_y = d$, $\alpha = 0.2d$, $\Delta_s = 0.5d$, d) $B_y = 4d$, $\alpha = 0.2d$, $\Delta_s = 0.3d$. A more detailed evolution of the spectra, as well as more cases with different parameter values, can be found in the appendix section. 56

4.31 Density of states evolution with Aubry-André disorder for $E \in [-0.4, 0.4]$, for the parameter values a) $B_y = 0.5d$, b) $B_y = d$, c) $B_y = d$, $\alpha = 0.2d$, $\Delta_s = 0.5d$, d) $B_y = 4d$, $\alpha = 0.2d$, $\Delta_s = 0.3d$. 57

4.32 a) Edge states of the clean system with size $N_y = 200$ and magnetic field $B_y = 0.5d$, at $k_x = 0$ (zero energy state) and $k_x = 0.02\pi$ (finite energy state). b) Flat band zero energy states of the quasi-disordered system at $B_y = 0.5d$, $\lambda = 1.4$. 58

4.33 a) MES for $E = 0$, $k_x = 0$ and with no disorder, for a system with $N_y = 200$ and parameters corresponding to figure 4.30 d). b) State at $E = 0$, $k_x = 0$ with quasi-periodic potential of strength $\lambda = 1.2$ and a random value of ϕ. The state has a flipped velocity, as is seen in the energy spectrum. 58

4.34 Energy spectrum evolution for a system with 76 sites in y for different values of λ vs. Berry phase normalized by 2π as a function of k_x, for a random value of ϕ in the quasi-disorder potential. The values of the parameters are $t = 1$, $d = t/6$, $\mu = 3d - 4t$, $By = 0.5d$ and $\lambda = 1.4$ (left), $\lambda = 1.6$ (middle), $\lambda = 1.8$ (right). 60

4.35 Energy spectrum evolution for a system with 76 sites in y for different values of λ vs. Berry phase normalized by 2π as a function of k_x, for a random value of ϕ in the quasi-disorder potential. The values of the parameters are $t = 1$, $d = t/6$, $\mu = 3d - 4t$, $By = d$ and $\lambda = 1.4$ (left), $\lambda = 1.6$ (middle), $\lambda = 1.8$ (right). 60

4.36 a) Values of ρ_γ for the case $t = 1$, $d = t/6$, $\mu = 3d - 4t$ and $B_y = 0.5d$ (figure 4.30 a)) vs. quasi-disorder strength λ. Obtained for a system with 76 sites in y. b) Value of the DOS at $E = 0$ for the same parameter values as in a), vs. quasi-disorder strength λ, and the contribution for $\rho(E = 0)$ which comes from the Majorana flat bands in the corresponding regime. 61

4.37 a) Density of states $\rho(E)$ at the critical value of the magnetic field, $B_{y,C}$, and fit of a function of the form of equation 4.20 to the energy range E $\in [0.005, 0.025]$ (black dashed line). Obtained for a system with PBC with size $N_y = 400$, and using a number of k_x points $N_k = 629$. b) Energy spectrum for the same parameter values and the same system size as in a), with PBC. The energy region E $\in [-0.025, 0.025]$ is highlighted. 63

4.38 Density of states for $E \in [0.02, 0.09]$ and several values of B_y close to the critical value, $B_{y,C}$, scaled according to equation 2.47 for $z = 1.08$ and $\nu = 0.95$. 64

4.39 a) Density of states $\rho(E)$ at the critical value of the disorder strength, $\lambda_{C,1} = 1.225$, and fit of a function of the form of equation 4.20 to the energy range E $\in [0.005, 0.025]$ (black dashed line). Obtained for a system with PBC with size $N_y = 800$, and using a number of k_x points $N_k = 629$ and averaged over 10 disorder configurations. b) Energy spectrum for the same parameter values and the same system size as in a), with PBC and $\phi = 0$ in the quasi-periodic potential. The energy region E $\in [-0.025, 0.025]$ is highlighted. 65

4.40 a) Density of states $\rho(E)$ at the critical value of the disorder strength, $\lambda_{C,2} = 1.805$, and fit of a function of the form of equation 4.20 to the energy range E $\in [0.005, 0.025]$ (black dashed line). Obtained for a system with PBC with size $N_y = 800$, and using a number of k_x points $N_k = 629$ and averaged over 10 disorder configurations. b) Energy spectrum for the same parameter values and the same system size as in a), with PBC and $\phi = 0$ in the quasi-periodic potential. The energy region E $\in [-0.025, 0.025]$ is highlighted. 65

4.41 Density of states for $E \in [0.005, 0.025]$ and several values of λ close to the critical values, a) $\lambda_{C,1} = 1.225$ and b) $\lambda_{C,2} = 1.805$, scaled according to Equation 2.47 for a) $z = 1.27$, $\nu = 0.95$ and b) $z = 1.23$, $\nu = 1.00$. 66

4.42 Results of τ vs. q, for several values of Anderson disorder strength, λ, for a) $k_x = 0.02\pi$ and b) $k_x = 0.2\pi$. The IPR is averaged for the states within the energy range $E \in [0.05, 1]$. 68

4.43 Values of τ at different values of q and disorder strength λ, for $k_x = 0.02\pi$ (●) and $k_x = 0.2\pi$ (▲). The IPR is averaged for the states within the energy range $E \in [0.05, 1]$. 69

4.44 Results of τ vs. q, for several values of quasi-periodic disorder strength, λ, for a) $k_x = 0.02\pi$ and b) $k_x = 0.2\pi$. The IPR is averaged for the states within the energy range $E \in [0.05, 1]$. 70

4.45 Values of τ at different values of q and disorder strength λ, for $k_x = 0.02\pi$ (●) and $k_x = 0.2\pi$ (▲). The IPR is averaged for the states within the energy range $E \in [0.05, 1]$. 71

4.46 Example of wavefunctions on the different phases, at a fixed value $k_x = 0.02\pi$, for a system with 200 sites in y. a) Extended wavefunction at $E = 0.63$, $\lambda = 0$, b) critical wavefunction at $E = 0.67$, $\lambda = 1.6$, c) localized wavefunction at $E = 0.7$, $\lambda = 2.6$. Obtained for random values of ϕ in the quasi-periodic potential. Note that for each figure the scale of the y axis changes by a factor of 10. 71

C.1 Energy spectrum evolution for a system with 76 sites in y and edges at $y = 0$ and $y = 75$ for different values of λ as a function of k_x, for $\phi = 0$ in the quasi-periodic potential. The values of the parameters are $t = 1$, $d = t/6$, $\mu = 3d - 4t$, $B_y = 0$. 93

C.2 Energy spectrum evolution for a system with 76 sites in y and edges at $y = 0$ and $y = 75$ for different values of λ as a function of k_x, for $\phi = 0$ in the quasi-periodic potential. The values of the parameters are $t = 1$, $d = t/6$, $\mu = 3d - 4t$, $By = 0.5d$. 94

C.3 Energy spectrum evolution for a system with 76 sites in y and edges at $y = 0$ and $y = 75$ for different values of λ as a function of k_x, for $\phi = 0$ in the quasi-periodic potential. The values of the parameters are $t = 1$, $d = t/6$, $\mu = 3d - 4t$, $B_y = d$. 94

C.4 Energy spectrum evolution for a system with 76 sites in y and edges at $y = 0$ and $y = 75$ for different values of λ as a function of k_x, for $\phi = 0$ in the quasi-periodic potential. The values of the parameters are $t = 1$, $d = t/6$, $\mu = 3d - 4t$, $B_y = 3d$. 95

C.5 Energy spectrum evolution for a system with 76 sites in y and edges at $y = 0$ and $y = 75$ for different values of λ as a function of k_x, for $\phi = 0$ in the quasi-periodic potential. The values of the parameters are $t = 1$, $d = t/6$, $\mu = 3d - 4t$, $B_y = d$, $\alpha = 0.2d$, $\Delta_s = 0.5d$. . 95

C.6 Energy spectrum evolution for a system with 76 sites in y and edges at $y = 0$ and $y = 75$ for different values of λ as a function of k_x, for $\phi = 0$ in the quasi-periodic potential. The values of the parameters are $t = 1$, $d = t/6$, $\mu = 3d - 4t$, $B_y = 4d$, $\alpha = 0.2d$, $\Delta_s = 0.3d$. . 96

List of Abbreviations

BdG Bogoliubov-de Gennes.

CS Chiral Symmetry.

DOS Density of States.

IPR Inverse Participation Ratio.

MES Majorana Edge State.

MFB Majorana Flat Bands.

OBC Open Boundary Conditions.

PBC Periodic Boundary Conditions.

PHS Particle Hole Symmetry.

PR Participation Ratio.

RGF Recursive Green's Function.

TRS Time Reversal Symmetry.

1

Introduction

1.1 State of the art

The search and study of topological properties of matter has proved fruitful in recent years in research in materials science and condensed matter physics. Superconductors have long been a focus of interest due to their promising applications. Superconductors with intrinsic topological properties, in particular, have recently attracted theoretical and experimental interest due to phenomena associated with surface or edge Majorana modes, which appear from an interplay between topology and bulk-boundary correspondence [1–3]. These Majorana zero modes emerge with non-Abelian exchange statistics and are sought after due to their promising expected applications in quantum computing, being candidates for the building blocks of a quantum qubit [4, 5].

It has been theoretically predicted that Majorana states appear as flat dispersion bands in gapless superconducting phases, such as in the d_{xy}+p-wave pairing noncentrosymmetric superconductor in two dimensions with preserved time-reversal symmetry [6, 7], or for a p-wave topological superconductor in two dimensions, with broken time reversal symmetry by an applied magnetic field parallel to the two-dimensional plane of the system [8]. Flat bands also emerge on the surface of three-dimensional noncentrosymmetric superconductors, with spin-orbit coupling and which preserve time-reversal symmetry [9, 10]. It is predicted that flat bands can increase the critical temperature for superconductivity, and even give rise to room-temperature superconductivity. The difference between an isolated flat band and a flat band with band touchings has also been recently discussed [11]. It was shown that isolated flat bands are not needed to achieve a higher superconducting temperature, and that band touchings can actually increase it.

There are several possibilities for the experimental detection of Majorana states in condensed matter systems. Examples of the fundamental signatures which make their detection possible are an expected zero-bias peak in the conductance, tunneling processes, and thermal metal-insulator transitions [1]. A well known possibility for the experimental realization of Majorana modes envolves proximity induced superconductivity [12], through superconductor-semiconductor heterostructures [13] in which a semiconductor is placed on top of a superconductor. An experimental realization involving a nanowire device [14] provided experimental evidence of the existence of Majorana zero modes. Localized zero energy

edge modes were also detected experimentally [15], using scanning tunneling microscopy, in a ferromagnetic chain placed on top of a conventional s-wave superconductor, and these were understood as Majorana modes.

The study of perturbations in condensed matter systems, namely through the introduction of disorder, is a central issue, which appears as a double edged sword. On one hand, introducing disorder can destroy some phases and their properties, preventing their experimental observation. In this sense, the study of their robustness becomes crucial. On the other hand, disorder can by itself lead to new phenomena or stabilize previously existing phases. One type of disorder that has been attracting interest in the research field is quasi-periodic disorder. The Aubry-André model [16] is the best known example of a one-dimensional quasi-periodic system, and describes a chain subject to a quasi-periodic potential which is incommensurate with the lattice. Unlike the case of Anderson disorder [17], the quasi-periodic potential induces a delocalization-localization transition for a finite value of quasi-disorder strength. At the transition point, the system has fractal properties, with the energy spectrum of the model giving rise to the well known Hofstadter butterfly [18], and the system exhibiting critical wavefunctions. Localization by the effect of incommensurability is also found in other systems, for example in coupled Aubry-André chains or two-dimensional lattices subject to Aubry-André potentials [19], or in Moiré-type systems [20, 21]. Moiré systems, in which two incommensurate lattices are connected, or in which layers of lattices are put in contact and rotated, have been getting increasing interest. A noticeable example of a system of such type is the two dimensional twisted bilayer graphene [22–26].

Besides localization, several interesting phenomena are found in systems with a quasi-periodic nature, in transport, critical behaviour, and topological properties [27–32]. Results regarding the interplay between quasi-periodic disorder and topology suggest that the two can coexist. One dimensional quasi-periodic optical lattices have been predicted to host topological phases usually assigned to two dimensions, with the appearance of edge states [30]. Quasicrystals were shown, not only theoretically but also experimentally, to also exhibit topological properties and edge states [31] which are topologically protected in one dimension by topological invariants assigned in higher dimensions. Some possible experimental realizations of quasi-periodic systems include setups of ultracold atoms [33, 34], optical lattices [35, 36] or photonic systems [31, 37].

An example of the study of coexisting quasi-disorder and superconductivity, which is remarkable in the context of this work, is the one dimensional Kitaev chain with Aubry-André modulation [38–44]. The introduction of p-wave pairing in the Aubry-André model leads to the appearance of a region of critical (fractal) states. Remarkably, the transitions between localized and critical regimes have been studied and were found to deviate from the known Aubry-André universality class [40, 41]. A model of a topological superconductor, consisting in a one dimensional wire with spin orbit coupling, subject to a magnetic field and in contact with a bulk superconductor, was also studied with a quasi periodic-potential. It was found that topological regions appear [45] for finite values of the quasi-periodic potential.

While the study of quasi-disorder in topological superconductors is still in expansion, the effects of uncorrelated disorder have been more widely studied. In particular, since the edge of real materials can be intrinsically disordered, and taking into account the bulk-edge correspondence in topological super-

conductors, the study of edge disorder becomes a topic of interest. Superconductors without inversion symmetry have been studied both in weak and strong non-magnetic and magnetic edge disorder [46]. It was found that edge states are robust against against weak and moderately strong non magnetic disorder, but vulnerable for magnetic disorder, which can also lead to the appearance of new, weakly localized in-gap states. Another topic of interest is the study of possible stabilization, destruction or induction of topological phases in superconductors. For instance, it is found that a two dimensional superconductor with spin-orbit coupling and in the presence of a magnetic field can have induced or changed topological order in the presence of randomly displaced magnetic impurities with orientational correlation [47].

In this work we study a model of a two-dimensional superconductor with spin triplet p-wave pairing, or mixed p and s-wave pairings with Rashba spin-orbit coupling, in the presence of a magnetic field which breaks time reversal symmetry. Some materials which are candidates for realizing triplet pairing superconductivity include Sr_2RuO_4 [48], UPt_3 [49] and $Cu_xBi_2Se_3$ [50]. In the presence of s-wave pairing and Rashba spin orbit coupling, the model describes a noncentrosymmetric superconductor, of which are examples $CePt_3Si$ [51], $CeIrSi_3$ [52] and $CeRhSi_3$ [53]. In the noncentrosymmetric regime the breaking of inversion symmetry allows for the mixture of spin-triplet and spin-singlet pairings. This mixing is expected to lead to novel phenomena such as higher than usual values of the upper critical field [54, 55].

The clean model has been studied and is known to possess diverse topological properties. If time-reversal symmetry is preserved, the model displays gapless Majorana edge states and is characterized by a $\mathbf{Z}_2$ invariant. The observed properties when time-reversal symmetry is broken by an external magnetic field are found to be very dependent on its direction in relation to the two-dimensional superconducting plane. If the magnetic field is such that it is perpendicular to the plane of the superconductor, the model has a rich phase diagram indexed by the Chern number [56]. When the magnetic field is parallel to the plane of the system, interesting phenomena, such as Majorana flat bands or Majorana unidirectional states, appear on phases with a gapless bulk [8]. We are interested in studying the effects of quasi-disorder in these regimes, on topological and localization properties. Besides Aubry-André disorder, we will also consider Anderson disorder as a comparison to the effects of quasi-periodicity.

1.2 Thesis outline

The rest of the thesis is organized as follows:

- In **chapter 2**, the concepts fundamental to the work are briefly discussed. We go over some of the basics of topology, superconductivity and some theoretic and analytical aspects of disordered systems.

- In **chapter 3** the model for the clean superconductor (without disorder) is presented, and the phenomena observed first under a perpendicular and secondly under a parallel magnetic field are discussed. This chapter reviews results that have already been established. Exceptions are the observed dependence of the Chern number on a magnetic field with simultaneous parallel and

perpendicular contributions, and the regions where Majorana flat bands appear under a parallel magnetic field, which are new obtained results.

- In **chapter 4**, the results obtained for the disordered model are presented. The chapter is divided in two main sections. In section **4.1** the superconductor is studied on a real space approach.
  - In section **4.1.1** we introduce edge disorder in the real space system. The cases of Anderson edge disorder and Aubry-André edge disorder are analyzed, the IPR is obtained and the effect on the edge states is discussed.
  - In section **4.1.2** the case of bulk disorder is considered, and three types of disorder are taken into account: Anderson disorder, Anderson disorder uniform in the x direction, and Aubry-André disorder uniform in the x direction. The IPR is obtained and the low energy wavefunctions are studied. The density of states (DOS) is obtained with the Recursive Green's Function (RGF) method in the various regimes (details of the numerical method are presented in the appendix section).
  - In section **4.1.2** we study the same types of bulk disorder on the system under a perpendicular magnetic field and obtain the Chern number in real space (details of the numerical method are presented in the appendix section). We show that quasi-disorder leads to the appearance of topological phases in new regimes.

  In section **4.2** the model is studied in a mixed space and under a parallel magnetic field.
  - In **4.2.1** we show and discuss the evolution of the energy spectra and density of states when Anderson disorder or Aubry-André disorder are introduced.
  - Quasi-disorder induced Majorana flat bands (MFBs) are studied in section **4.2.2**. The Berry phase is obtained numerically using twisted boundary conditions and we show it is quantized in the MFB regime. The contribution of the flat bands to the DOS is discussed and two topological transitions are presented.
  - In **4.2.3** a scaling analysis near the identified phase transitions is made. We briefly discuss a topological transition in the clean system and derive the values of the critical exponents. We then obtain the critical exponents for the identified transitions in the quasi-disordered case and show that the critical exponents deviate from the known universality classes.
  - In **4.2.4** we obtain the IPR and discuss the nature of the wavefunctions, distinguishing between single-fractal and multifractal regimes, for Anderson and Aubry-André disorder. We make a study for different system sizes and see the tendency in the thermodynamic limit.
- We conclude in **chapter 5**, and possible future directions are discussed.

2

Fundamental Concepts

2.1 Topology in condensed matter physics

In a broad sense, topology is a mathematical field which aims to study whether objects can be continuously deformed into each other. In condensed matter physics, our ”objects” are actually Hamiltonians or states which we aim to classify in different topological classes. In general topological properties are classified by finding a number - topological invariant - that does not change under a continuous deformation of the geometry of the system in parameter space and thus characterizes the topology [4]. A transition between different topological regimes always implies a closing of the bulk gap (as long as interaction effects are not considered). If two Hamiltonians describing gapped systems can be deformed into each other without ever closing the bulk gap, such systems are said to be topologically equivalent.

2.1.1 Berry Phase

Let us suppose we have a system described by a Hamiltonian $\mathcal{H}(\mathbf{R})$ which depends on a set of parameters $\mathbf{R}$. The eigenstates $\mid \psi_n \rangle$ obey the Schrödinger equation

$$\mathcal{H}(\mathbf{R}) \mid \psi_n \rangle = E_n(\mathbf{R}) \mid \psi_n \rangle. \tag{2.1}$$

The *Berry connection* $\boldsymbol{\mathcal{A}_n}(\mathbf{R})$ is defined as

$$\boldsymbol{\mathcal{A}_n}(\mathbf{R}) = i \langle \psi_n(\mathbf{R}) \mid \boldsymbol{\partial}_{\mathbf{R}} \psi_n(\mathbf{R}) \rangle \tag{2.2}$$

and measures the rate of change of the wavefunctions with regards to the set of parameters $\mathbf{R}$ (vanishing if $\boldsymbol{\partial}_{\mathbf{R}} \mid \psi_n(\mathbf{R}) \rangle = 0$). The Berry connection is a gauge-dependent quantity. If we perform a transformation $\mid \psi_n(\mathbf{R}) \rangle \rightarrow e^{i\phi_n(\mathbf{R})} \mid \psi_n(\mathbf{R}) \rangle$ in the eigenstates then $\boldsymbol{\mathcal{A}_n}(\mathbf{R})$ must transform as $\boldsymbol{\mathcal{A}_n}(\mathbf{R}) \rightarrow \boldsymbol{\mathcal{A}_n}(\mathbf{R}) - \boldsymbol{\partial}_{\mathbf{R}} \phi_n(\mathbf{R})$. The *Berry phase* γ_n can be written as the line integral of the Berry connection over a path in parameter space:

$$\gamma_n = \int_{\mathcal{C}} \boldsymbol{\mathcal{A}_n}(\mathbf{R}) \cdot d\mathbf{R}. \tag{2.3}$$

Defining $\mathbf{R_i}$ and $\mathbf{R_f}$ as the initial and final points on a certain path (not neccessarily closed), we can see that for the same phase transformation of the eigenstates defined above, the Berry phase would be changed by $\phi(\mathbf{R_f}) - \phi(\mathbf{R_i})$. In the case of a closed path, in which $\mathbf{R_f} = \mathbf{R_i}$, the phase transformation is required to be single valued, as it was noted by Berry [57] and thus we must have $\phi(\mathbf{R_f}) - \phi(\mathbf{R_i}) = 2\pi n$ with n an integer. Therefore, in a closed path $\mathcal{C}$, the Berry phase is a gauge-invariant quantity.

In general, the Berry phase can take any real value. In the presence of certain symmetry constraints, the Berry phase can become quantized to 0 or π and carry topological information (at the value of π). This quantization can happen in the presence of inversion or chiral symmetries, also leading to the quantization of polarization [58].

2.1.2 Chern Number

The Chern number was understood as a topological invariant in condensed matter physics by Thouless, Kohmoto, Nightingale and den Nijs (and thus is also called the TKNN integer), when the mathematical relation between the Hall conductivity and the Chern number was found for the integer quantum Hall effect [59]. Earlier, von Klitzing, Dorda, and Pepper had made the important experimental discovery [60] that for a two-dimensional, non interacting electron gas in a strong magnetic field, the Hall conductivity is quantized in units of e^2/h:

$$\sigma_{xy} = \frac{e^2}{h}\nu, \tag{2.4}$$

with ν an integer. It was later shown that the integer ν is actually related to the (total) Chern number, as

$$\sigma_{xy} = \frac{e^2}{h}\sum_n C^{(n)} \tag{2.5}$$

where $C^{(n)}$ denotes the Chern number of the n-th band. Equation 2.5 is also called the TKNN formula.

Let us then turn to the definition of the Chern number. Before defining it, we must first introduce another relevant (gauge-invariant) quantity, the *Berry curvature*:

$$\mathbf{\Omega_n} = \nabla_{\mathbf{R}} \times \boldsymbol{\mathcal{A}}_{\boldsymbol{n}}(\mathbf{R}). \tag{2.6}$$

If the parameter space has some periodicity in $\mathbf{R}$, then we can write

$$\int_{\mathcal{C}} \boldsymbol{\mathcal{A}}_{\boldsymbol{n}}(\mathbf{R}) \cdot d\mathbf{R} = \int_{\mathcal{S}} \mathbf{\Omega_n}(\mathbf{R}) \cdot \mathbf{dS} \tag{2.7}$$

where $\mathcal{S}$ is a surface enclosed by the path $\mathcal{C}$, (being also the system's unit cell). The Chern number of the n-th band is then defined as

$$C^{(n)} = \frac{1}{2\pi}\int_{\mathcal{S}} \mathbf{\Omega_n}(\mathbf{R}) \cdot \mathbf{dS}. \tag{2.8}$$

The total Chern number C is obtained by summing equation 2.8 over the filled energy bands, and a finite value of C signals the system has a topological nature. The Chern number requires time-reversal

symmetry breaking to have a nonzero value, and remains constant as long as the gap in the bulk energy of the system is open. If the gap closes, and then opens with a new value of C, a topological transition occurs.

2.1.3 Edge states and the bulk-edge correspondence

In addition to characterizing the phases by topological invariants, there are surface or edge modes resulting from the topology that may appear. Physically, a finite system will have a singularity at the boundary stemming from the difference in topological nature between the system and its environment, which results in the appearance of gapless edge states localized at such boundaries [61, 62]. It is then said that a bulk-edge correspondence exists, since the nontrivial topology of the bulk is revealed at the edges. A variety of such states exist, depending on the symmetries and dimension of the systems [63].

2.1.4 The SSH model and the winding number

The Su-Schrieffer-Heeger (SSH) model, which was developed to illustrate the behaviour of electrons in a polyacetylene molecule [64], is a remarkable example of a simple topological system where the bulk-edge correspondence can be easily visualized. In this section we present the dimerized model briefly and introduce an important topological invariant of one-dimensional systems with chiral symmetry, the winding number.

The SSH model describes a one dimensional lattice where each unit cell has two sites, A and B, with the intracell and intercell hopping terms differing in amplitude. The tight-binding Hamiltonian is given by [65] :

$$\mathcal{H} = t_0 \sum_{n=1}^{N} (|n, A\rangle\langle n, B|) + t_1 \sum_{n=1}^{N-1} (|n+1, A\rangle\langle n, B|) + \text{ h.c.} \tag{2.9}$$

where t_0 and t_1 are the intracell and intercell hoppings, respectively, and the states $|n, A\rangle$ or $|n, B\rangle$ describe the sites A or B in the cell n. By considering a periodic one dimensional chain and performing a Fourier transform to momentum space, we obtain the Bloch Hamiltonian

$$\mathcal{H}(k) = \begin{pmatrix} 0 & t_0 + t_1^* e^{-ik} \\ t_0^* + t_1 e^{ik} & 0 \end{pmatrix}, \tag{2.10}$$

from which we can obtain the eigenvalues

$$E(k) = \pm|t_0 + t_1^* e^{-ik}| = \pm\sqrt{t_0^2 + t_1^2 + 2t_0 t_1 \cos(k)} \quad \text{if } t_0,\, t_1 \in \mathbb{R}. \tag{2.11}$$

There are therefore two bands, one at positive and other at negative energy, and the spectrum has a gap as long as $t_0 \neq t_1$. The energy spectrum is shown in figure 2.1 for some values of t_0 and t_1. To simplify, t_0 and t_1 are taken to be real. The cases of $t_0 > t_1$ and $t_0 < t_1$ are symmetric in the bulk energy spectrum which can be easily seen by inspection of equation 2.11, but are topologically distinct. This can be observed by either investigating the eigenstates in the real space description of a chain with open boundary conditions or by calculating a topological invariant of the Hamiltonian. In fact, it can be noted

that the Hamiltonian belongs to the BDI class according to the symmetry classification (see Appendix A) and thus a topological invariant can be defined for $d = 1$. The Hamiltonian respects a chiral symmetry, and thus for a unitary matrix $\mathcal{S}$ obeys

$$\mathcal{S}\mathcal{H}(\mathbf{k})\mathcal{S}^{\dagger} = -\mathcal{H}(\mathbf{k}). \tag{2.12}$$

In the SSH model the matrix $\mathcal{S}$ coincides with the third Pauli matrix, σ_z.

The Hamiltonian matrix of a general two band system takes the form:

$$\mathcal{H}(k) = h_0\sigma_0 + \mathbf{h}(k)\cdot\boldsymbol{\sigma}. \tag{2.13}$$

If the said system respects a chiral symmetry as in 2.12, then the Hamiltonian can be rotated to an off-diagonal base, through the same transformation that diagonalizes the chiral matrix $\mathcal{S}$:

$$\mathcal{H}(k) = \begin{pmatrix} 0 & h(k) \\ h^*(k) & 0 \end{pmatrix}. \tag{2.14}$$

A topological invariant, known as winding number, can then be calculated as:

$$\mathcal{W} = \frac{1}{2\pi\mathrm{i}}\int_0^{2\pi} dk\,\frac{d}{dk}\log h(k). \tag{2.15}$$

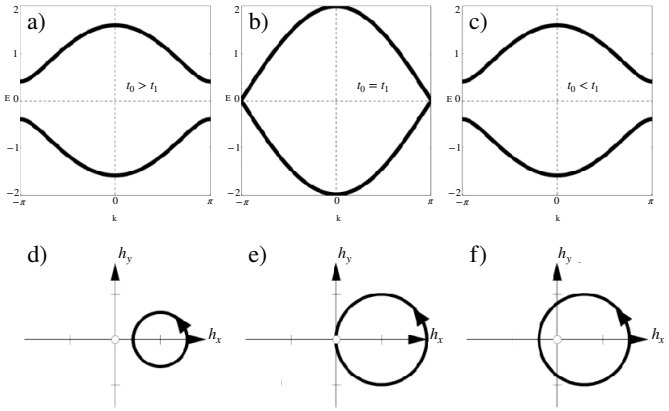

Figure 2.1: Top: Dispersion relations for different values of t_0 and t_1: a) $t_0 = 1, t_1 = 0.6$; b) $t_0 = t_1 = 1$; c) $t_0 = 0.6, t_1 = 1$. Bottom: The corresponding paths of the endpoints of the vectors $\mathbf{h}(k)$ as k sweeps the Brillouin zone. Image adapted from [65].

For the SSH model $h_0 = h_z = 0$, and $\mathbf{h}(k) = (h_x, h_y, 0)$ with $h_x = t_0 + t_1\cos(k)$ and $h_y = t_1\sin(k)$ such that $h(k) = h_x - \mathrm{i}h_y$ in 2.14. As k sweeps through the Brillouin zone, the vector $\mathbf{h}(k)$ describes a closed path in the (h_x, h_y) plane. The winding number $\mathcal{W}$ counts how many times this path circles the origin. The winding number is then 0 in the case where the intracell hopping dominates over the intercell ($|t_1| > |t_0|$) and 1 otherwise ($|t_1| < |t_0|$), as can be seen in figure 2.1. In the insulating phase, the path of $\mathbf{h}(k)$ always avoids the origin. For a general two-band insulator the path is not necessarily a circle, but must be a closed loop because of the periodicity of the bulk momentum space Hamiltonian. To change

the value of the winding number, we need to either close the bulk gap (by deforming the path through the origin in the (h_x, h_y) plane) or break the chiral symmetry of the system (lifting the path out of the (h_x, h_y) plane). The chiral symmetry assures the path of the $\mathbf{h}(k)$ vector stays in the (h_x, h_y) plane.

Let us now turn again to the real space description to illustrate how the non trivial topology is manifested in the edges [61, 62]. A stationary state $|n\rangle = (a_n\ b_n)^T$ with energy E obeys the equations:

$$\begin{aligned} E a_n &= t_0 b_n + t_1^* b_{n-1}, \\ E b_n &= t_1 a_{n+1} + t_0^* a_n. \end{aligned} \tag{2.16}$$

Considering a semi-infinite chain starting at $n = 0$, the system admits a zero energy state if:

$$a_n = \left(-\frac{t_0^*}{t_1}\right)^n a_0, \quad b_n = 0, \tag{2.17}$$

where $n \geq 0$. The state is localized at the left edge and decays along the chain, living in the A sublattice. This is only possible if $|t_1| > |t_0|$, coinciding with the topological phase characterized by $\mathcal{W} = 1$. If we instead consider a semi-infinite chain ending at $n = N$, for $n \leq N$ there is a zero energy state which exists in the B sublattice:

$$b_n \left(-\frac{t_0}{t_1^*}\right)^{N-n} b_N, \quad a_n = 0. \tag{2.18}$$

Thus for a large finite chain two localized zero energy states exist in the topological phase, and each of them occupies a different sublattice space, A or B. This is a simple example of the bulk-boundary correspondence; if $|t_1| < |t_0|$ then the localized edge states are not present in the system.

2.2 Superconductivity

Superconductivity has been widely studied ever since its experimental discovery in 1911 [66]. The phenomenology behind it was first understood in 1950 by Ginzburg and Landau, which developed a theory based on symmetry considerations [67]. Shortly after, in 1957, Bardeen, Cooper, and Schrieffer (BCS) developed a theory which could explain the microscopics of superconductivity [68]. The theory relies on the fact that electrons can interact in an attractive way through lattice distortion, forming Cooper pairs. *Topological superconductors* are superconductors which have a superconducting bulk and topologically protected gapless boundary states.

2.2.1 Bogoliubov-de Gennes equations

Let us consider a general description of a superconductor in $\boldsymbol{k}$-space. In terms of the creation $c^\dagger_{\mathbf{k},\alpha}$ and annihilation $c_{\mathbf{k},\beta}$ field operators, where α, β denote spin projections, the effective Hamiltonian can be written as

$$\mathcal{H} = \frac{1}{2} \sum_{\boldsymbol{k},\alpha,\beta} \left(c^\dagger_{\boldsymbol{k}\alpha}, c_{-\boldsymbol{k}\alpha}\right) \mathcal{H}_{4\times4}(\boldsymbol{k}) \begin{pmatrix} c_{\boldsymbol{k}\beta} \\ c^\dagger_{-\boldsymbol{k}\beta} \end{pmatrix} \tag{2.19}$$

with

$$\mathcal{H}_{4\times4}(\mathbf{k}) = \begin{pmatrix} \mathcal{E}_{\alpha\beta}(\boldsymbol{k}) & \Delta_{\alpha\beta}(\boldsymbol{k}) \\ \Delta^{\dagger}_{\alpha\beta}(\boldsymbol{k}) & -\mathcal{E}^{t}_{\alpha\beta}(-\boldsymbol{k}) \end{pmatrix}. \tag{2.20}$$

In this expression $\mathcal{E}_{\alpha\beta}(\boldsymbol{k})$ denotes the normal state Bloch Hamiltonian, and $\Delta_{\alpha\beta}(\boldsymbol{k})$ is the superconducting pairing term. Both terms are 2×2 matrices due to the sum in the spin indices. Also, $\left(\hat{c}^{\dagger}_{\boldsymbol{k}\alpha}, \hat{c}_{-\boldsymbol{k}\alpha}\right)$ is a short notation for the vector $\left(\hat{c}^{\dagger}_{\boldsymbol{k}\uparrow}, \hat{c}^{\dagger}_{\boldsymbol{k}\downarrow}, \hat{c}_{-\boldsymbol{k}\uparrow}, \hat{c}_{-\boldsymbol{k}\downarrow}\right)$, and the operators obey the usual fermionic statistics:

$$\begin{aligned} \{\hat{c}^{\dagger}_{\mathbf{k}\alpha}, \hat{c}_{\mathbf{k}'\beta}\} &= \delta_{\alpha\beta}\delta_{\mathbf{k}\mathbf{k}'}, \\ \{\hat{c}^{\dagger}_{\mathbf{k}\alpha}, \hat{c}^{\dagger}_{\mathbf{k}'\beta}\} &= \{\hat{c}_{\mathbf{k}\alpha}, \hat{c}_{\mathbf{k}'\beta}\} = 0. \end{aligned} \tag{2.21}$$

The Bogoliubov-de Gennes equations [69] are obtained by requiring that an operator $\hat{\gamma}(\mathbf{k})$ that destroys an excitation with energy E obeys $[\hat{\gamma}, \mathcal{H}] = E\hat{\gamma}$. The operator $\hat{\gamma}(\mathbf{k})$ then diagonalizes the Hamiltonian, and describes the excitations of quasiparticles called the *Bogoliubov quasiparticles*. $\hat{\gamma}(\mathbf{k})$ and $\hat{\gamma}^{\dagger}(-\mathbf{k})$ are defined by [61]

$$\begin{aligned} \hat{\gamma}(\mathbf{k}) &= \sum_{\alpha} \left[u^{*}_{\alpha}(\mathbf{k})\hat{c}_{\mathbf{k}\alpha} + v^{*}_{\alpha}(\mathbf{k})\hat{c}^{\dagger}_{-\mathbf{k}\alpha} \right], \\ \hat{\gamma}^{\dagger}(-\mathbf{k}) &= \sum_{\alpha} \left[u_{\alpha}(-\mathbf{k})\hat{c}^{\dagger}_{-\mathbf{k}\alpha} + v_{\alpha}(-\mathbf{k})\hat{c}_{\mathbf{k}\alpha} \right] \end{aligned} \tag{2.22}$$

and from imposing the commutation relations with $\mathcal{H}$, we obtain the the Bogoliubov-de Gennes equations:

$$\begin{aligned} E u_{\mu}(\mathbf{k}) &= \sum_{\alpha} \left[\mathcal{E}_{\mu\alpha} u_{\alpha}(\mathbf{k}) + \Delta_{\mu\alpha}(\mathbf{k}) v_{\alpha}(\mathbf{k}) \right], \\ E v_{\mu}(\mathbf{k}) &= \sum_{\alpha} \left[\Delta^{\dagger}_{\mu\alpha}(\mathbf{k}) u_{\alpha}(\mathbf{k}) - \mathcal{E}^{*}_{\mu\alpha}(-\mathbf{k}) v_{\alpha}(\mathbf{k}) \right]. \end{aligned} \tag{2.23}$$

The operator $\hat{\gamma}(\mathbf{k})$ annihilates the ground state of a superconductor,

$$\hat{\gamma}(\mathbf{k})|0\rangle = 0 \tag{2.24}$$

implying that the negative energy states are fully occupied.

2.2.2 Superconducting pairing term

The pairing term $\Delta_{\alpha\beta}(\mathbf{k})$, which we will now write as $\Delta(\mathbf{k})$, is related to the electron interaction, and it describes the simultaneous creation or destruction of two particles. The pairing potential obeys $\Delta(\mathbf{k}) = -\Delta^{T}(-\mathbf{k})$ which is required from the nature of fermionic interactions (equation 2.21).

For *singlet* pairing, i.e when the Cooper pair is in a singlet state, then Δ must be *even* in $\mathbf{k}$, and

therefore antisymmetric in spin space. In terms of a even function $\psi(\mathbf{k})$ we can write

$$\Delta(\mathbf{k}) = i\hat{\sigma}_y \psi(\mathbf{k}) = \begin{pmatrix} 0 & \psi(\mathbf{k}) \\ -\psi(\mathbf{k}) & 0 \end{pmatrix}. \tag{2.25}$$

On the other hand, for *triplet* pairing, the pairing term must be *odd* in $\mathbf{k}$. Then the matrix Δ will be symmetric in the spin indices, and using an odd vectorial function $d(\mathbf{k})$, we may write [70]

$$\begin{aligned} \Delta(\mathbf{k}) &= i(\mathbf{d}(\mathbf{k}) \cdot \hat{\boldsymbol{\sigma}})\hat{\sigma}_y \\ &= \begin{pmatrix} -d_x(\mathbf{k}) + id_y(\mathbf{k}) & d_z(\mathbf{k}) \\ d_z(\mathbf{k}) & d_x(\mathbf{k}) + id_y(\mathbf{k}) \end{pmatrix}. \end{aligned} \tag{2.26}$$

The symmetry of Cooper pairs is then classified into spin-singlet even-parity and spin-triplet odd-parity, and even or odd pairing refers to the orbital part of the amplitude. s-wave and d-wave pairings belong to the first case and p-wave pairing is included in the latter. In systems which are noncentrosymmetric, the inversion symmetry is broken and it is possible to have parity mixing in the pair potential $\Delta(\mathbf{k})$, which takes the form

$$\Delta(\mathbf{k}) = i\left(\psi(\mathbf{k}) + \mathbf{d}(\mathbf{k}) \cdot \hat{\boldsymbol{\sigma}}\right)\hat{\sigma}_y. \tag{2.27}$$

2.2.3 Particle-Hole Symmetry and Majorana fermions

A Bogoliubov-de Gennes Hamiltonian $\mathcal{H}(\mathbf{k})$ obeys a particle-hole symmetry, or charge conjugation operation. This symmetry expresses the redundancy of the Hamiltonian in the sense that the components of the vector $\left(\hat{c}^\dagger_{\boldsymbol{k}\alpha}, \hat{c}_{-\boldsymbol{k}\alpha}\right)$ are not independent and that the positive and negative energy states come in pairs. Mathematically, this symmetry can be expressed by:

$$\mathcal{P}\mathcal{H}(\mathbf{k})\mathcal{P}^\dagger = -\mathcal{H}^*(-\mathbf{k}) \tag{2.28}$$

where $\mathcal{P}$ coincides with the first Pauli matrix operating in particle-hole space. The particle-hole symmetry implies that for a wavefunction $\Psi(\mathbf{k})$ with energy E, the state $\mathcal{P}\Psi^*(-\mathbf{k})$ has energy $-E$ [61]. Thus, for a non degenerate state with $E = 0$, we have $\Psi(\mathbf{k}) = \mathcal{P}\Psi^*(-\mathbf{k})$, and this implies for the excitation operators 2.22 that:

$$\gamma(\mathbf{k}) = \gamma^\dagger(-\mathbf{k}). \tag{2.29}$$

In this case, the excitation then describes a Majorana mode, since the creation and annihilation operators coincide.

2.2.4 The Kitaev toy model

Let us now turn to a real space description and use Kitaev's model for a one-dimensional p-wave superconductor [71] to illustrate how isolated Majorana modes can arise in topological superconductors. The creation and annihilation fermionic operators $\hat{c}^\dagger_j$ and $\hat{c}_j$ at a local site j can be written in terms of Majorana operators $\hat{\gamma}_{j,1}$ and $\hat{\gamma}_{j,2}$ as

$$\begin{cases} \hat{c}_j = \frac{1}{2}(\hat{\gamma}_{j,1} + i\hat{\gamma}_{j,2}), \\ \hat{c}_j^\dagger = \frac{1}{2}(\hat{\gamma}_{j,1} - i\hat{\gamma}_{j,2}). \end{cases} \tag{2.30}$$

Mathematically, the fermionic operators $\hat{c}_j^\dagger$ and $\hat{c}_j$ are split into their real and imaginary parts. Inverting equation 2.30 is is possible to see that the operators are hermitian and satisty the relations

$$\{\hat{\gamma}_i, \hat{\gamma}_j\} = 2\delta_{ij}. \tag{2.31}$$

The model introduced by Kitaev describes a one dimensional chain of spinless fermions with p-wave pairing, and its Hamiltonian reads

$$\mathcal{H} = -\mu \sum_j^N \hat{c}_j^\dagger \hat{c}_j - t \sum_j^{N-1} \left(\hat{c}_j^\dagger \hat{c}_{j+1} + \hat{c}_{j+1}^\dagger \hat{c}_j \right) - \Delta \sum_j^{N-1} \left(\hat{c}_{j+1}^\dagger \hat{c}_j^\dagger + \hat{c}_j \hat{c}_{j+1} \right) \tag{2.32}$$

where μ is the chemical potential, t is the hopping parameter and Δ is the pairing amplitude. By rewriting the Hamiltonian 2.32 in terms of the Majorana operators 2.30, and taking the parameter values $\mu = 0$, $t = \Delta$, the resulting Hamiltonian is given by

$$\mathcal{H} = \sum_j^{N-1} \hat{\gamma}_{j,2} \hat{\gamma}_{j+1,1}. \tag{2.33}$$

It is possible to see that the operators $\hat{\gamma}_{1,1}$ and $\hat{\gamma}_{N,2}$ are absent from the rewritten Hamiltonian. There are therefore two zero energy Majorana modes that emerge localized at the ends of the Kitaev chain, reflecting the topological nature of the phase. These states are present as long as $|\mu| < 2t$ (where the bulk gap remains open) [61, 62]. The two Majorana operators $\hat{\gamma}_{1,1}$ and $\hat{\gamma}_{N,2}$ can be combined in a new non-local fermionic operator,

$$\tilde{c}_N = \frac{1}{2} \left(\hat{\gamma}_{N,2} + i\hat{\gamma}_{1,1} \right), \tag{2.34}$$

which can be occupied with a zero energy cost, making the ground state two-fold degenerate, corresponding to the cases of an even or odd number of electrons [72].

2.3 Disordered systems

Disorder effects may have several origins: impurities, quasi-periodic potentials, lattice distortions, among others. Some types of disorder are random and unavoidable in real life materials, while others can be introduced artificially. In any case, disordered systems are responsible for interesting and exotic phenomena that do not happen in ordered systems. The most remarkable is perhaps the localization of wavefunctions in disordered systems with broken translational invariance [73]. In such cases, the presence of disorder causes wavefunctions to be localized, which means that for a given energy and disorder strength, the quantum states can be either localized or delocalized (extended) - and therefore a transition exists between localized and metallic phases, which is known as an *Anderson transition* [74].

Different types of trivial systems were grouped in three main universal Anderson transition classes

(coinciding with the Wigner–Dyson random matrix theory description), in which the spin rotation and time reversal symmetries are the two criteria. These are the unitary (systems with broken time reversal symmetry), the orthogonal (systems which preserve time reversal symmetry and spin rotation symmetry) and the symplectic classes (systems with broken time reversal symmetry and preserved spin rotation symmetry) [17]. These classes are also called class A, AI and AII, respectively (see Appendix A). The dimension of the system d is also an important criteria to classify a system's response to static disorder [47]. In one dimensional systems, $d = 1$, all states are localized for any finite value of uncorrelated disorder. An important exception exists at correlated spatial disorder, such as the case of a quasi-periodic Aubry-André potential [16] where intermediate regimes for which wavefunctions are not extended states but are also not fully localized - *critical* states - appear. For two dimensional systems, $d = 2$, the behaviour is found to be very dependent on the symmetry class. In systems that respect both time reversal and spin rotation symmetries (orthogonal class), results show that the system is composed only of localized states in the presence of disorder. For $d = 2$ systems with time reversal symmetry but no spin rotation symmetry (symplectic class), there is a region of extended states, and a delocalized-localized Anderson transition is present for some value of the disorder strength. For broken time reversal symmetry (unitary class), there is one critical state for which the localization displays a linear divergence with the system size. If both TRS and spin rotation symmetries are broken, this behaviour is found not only for one state, but for a band of states, which can be extended or display critical behaviour. For $d = 3$ there is a region in energy space of extended states, separated from the localized region by a mobility edge which moves as a function of the disorder strength.

It is important to note that this initial classification coinciding with the Wigner-Dyson classification is incomplete, and it is now understood that there exist more symmetry classes of disordered systems. A complete symmetry classification includes seven additional classes, characterized by the chiral or particle hole symmetries [75]. In other cases, the system's response to disorder may also depend on the type of disorder itself, making the symmetry classification insufficient.

2.3.1 Participation Ratio

The participation ratio is a useful quantity to quantify the localization of wavefunctions. For a given eigenstate labelled by m, we define the participation ratio (PR) as

$$\mathcal{PR}_m = \frac{1}{\sum_i |\psi_i^m|^4} \tag{2.35}$$

where ψ_i^m denotes the amplitude of the eigenstate m at site i. If a state is perfectly localized, then $\sum_i |\psi_i^m|^4 = 1$ and $\mathcal{PR}_m = 1$. If a state is perfectly delocalized such that it is evenly distributed over N sites then we can expect $\sum_i |\psi_i^m|^4 = \frac{1}{N}$ and $\mathcal{PR}_m = N$. Sometimes it can be more useful to work with the inverse participation (IPR) ratio, which is just the inverse of the quantity defined in equation 2.35:

$$\mathcal{IPR}_m = \sum_i |\psi_i^m|^4 \tag{2.36}$$

so that for perfectly localized states $\mathcal{IPR}_m \sim 1$ and for delocalized states $\mathcal{IPR}_m \sim 1/N$. For large systems ($N \to \infty$) we can see that $\mathcal{IPR}_m \to 0$ for delocalized states.

Finally, we note that the (inverse) participation ratio is a specific case of a wider definition, a generalized (inverse) participation ratio

$$\mathcal{IPR}_m(q) = \sum_i |\psi_i^m|^{2q} \tag{2.37}$$

$$\mathcal{PR}_m(q) = \frac{1}{\sum_i |\psi_i^m|^{2q}} \tag{2.38}$$

with $q = 2$.

2.3.2 Multifractality of wave functions

One of the effects of Anderson transitions is the emergence of multifractality, which is characterized by fluctuations of eigenstates. These fluctuations are manifested in the generalized inverse participation ratio (Equation 2.37), which, at criticality, behaves as [76, 77]

$$\mathcal{IPR}(q) \sim L^{\tau(q)} \tag{2.39}$$

where L is the system size and the exponent $\tau(q)$ is defined in terms of a generalized dimension $D(q)$ as $\tau(q) = D(q)(q-1)$. In a metallic phase, $D(q) = d$ and for an insulating phase $D(q) = 0$. Wavefunction multifractality is characterized by a q dependent value of $D(q)$, whereas the cases of a constant $D(q)$ are single fractals [17]. Some important aspects can be derived [77] regarding the behaviour of the functions $\tau(q)$ and $D(q)$:

- $\tau(q)$ is monotonically increasing and has a negative curvature:

$$\frac{d\tau(q)}{dq} > 0, \frac{d^2\tau(q)}{dq^2} \leq 0. \tag{2.40}$$

- $D(q)$ is positive, monotonically decreasing and bounded by its value at infinity, $D(q \to \pm\infty)$:

$$\frac{dD(q)}{dq} \leq 0, \quad 0 \leq D_\infty \leq D(q) \leq D_{-\infty} \tag{2.41}$$

- $\tau(q)$ has slopes which are asymptotically constant and obtained from the values of $D(q)$ at infinity.

2.3.3 Scaling properties near a phase transition

Near a critical point where the characteristic length of the system diverges, the density of states follows a behaviour which is found to be universal. In this section, we follow references [78] and [79]. The number of states $\mathcal{N}$ below an energy E in a d-dimensional system with size L is a function of the (dimensionless) parameters L/ξ and E/E_0:

$$\mathcal{N}(E, L) = f\left(\frac{L}{\xi}, \frac{E}{E_0}\right), \tag{2.42}$$

where ξ and E_0 are the characteristic length and energy scales, which are related by the dynamical exponent z as $E_0 \sim \xi^{-z}$. The density of states per unit volume, $\rho(E)$, is given by

$$\rho(E) = \frac{1}{L^d}\frac{d\mathcal{N}(E, L)}{dE} \tag{2.43}$$

and using equation 2.42 and the relation between E_0 and ξ, we obtain

$$\rho(E) = \frac{1}{L^d E_0} f'(E, L) \sim \frac{\xi^z}{L^d} f'(E, L). \tag{2.44}$$

The number of states $\mathcal{N}(E, L)$ should be proportional to L^d, and we can write

$$\mathcal{N}(E, L) = (L/\xi)^d g(E\xi^z), \tag{2.45}$$

where g is the part of the function f (equation 2.42) that depends explicitly on E. Inserting equation 2.45 on 2.44 gives

$$\rho(E) = \frac{\xi^z}{L^d} f'(E, L) = \xi^{z-d} g'(E\xi^z) = \xi^{z-d} g'(|E|\xi^z), \tag{2.46}$$

where the last equality comes from the fact that $\rho(E)$ must be symmetric around $E = 0$. Around a critical point, the length scale ξ diverges. Defining the distance to a critical point λ_C as $\delta = \frac{|\lambda - \lambda_C|}{\lambda_C}$, ξ is expected to diverge as $\xi \sim \delta^{-\nu}$, so that around the critical point $\rho(E)$ can be written as

$$\rho(E) = \delta^{(d-z)\nu} g'(|E|\delta^{-z\nu}), \tag{2.47}$$

and right at the critical point (where $\delta = 0$) the dependence on ξ should be lost, so that $\rho(E)$ behaves as

$$\rho(E) \sim |E|^{\frac{d}{z}-1}. \tag{2.48}$$

The dynamical critical exponent z and the correlation length exponent ν also dictate the closing of the bulk gap. Near a quantum phase transition, as a critical point λ_C is approached, the gap behaves as [80]

$$\Delta \sim |\lambda - \lambda_C|^{z\nu}, \tag{2.49}$$

thus the dominant term in the parameter λ has an exponent $z\nu$. If the gap closes at a value of momentum k_0, at the value of the critical parameter λ_C the dominant term in the dispersion relation obeys

$$E(\lambda = \lambda_C) \sim |k - k_0|^z. \tag{2.50}$$

3

Clean two-dimensional topological superconductor

3.1 Model Hamiltonian

We start by presenting the model for a two-dimensional superconductor, with spin-orbit coupling, an external magnetic field, and with both spin triplet p-wave pairing and spin singlet s-wave pairing. In momentum space, the BdG Hamiltonian matrix is written as

$$\mathcal{H}(\mathbf{k}) = \begin{pmatrix} \xi(\mathbf{k}) + \mathbf{B}\cdot\boldsymbol{\sigma} & \Delta(\mathbf{k}) \\ \Delta^{\dagger}(\mathbf{k}) & -\xi^{T}(-\mathbf{k}) - \mathbf{B}\cdot\boldsymbol{\sigma}^{*} \end{pmatrix} \tag{3.1}$$

in a basis $(\boldsymbol{c}_{\mathbf{k}}^{\dagger}, \boldsymbol{c}_{-\mathbf{k}}) = (c_{\mathbf{k}\uparrow}^{\dagger}, c_{\mathbf{k}\downarrow}^{\dagger}, c_{-\mathbf{k}\uparrow}, c_{-\mathbf{k}\downarrow})$ with $c_{\mathbf{k}s}^{\dagger}$ ($c_{\mathbf{k}s}$) the creation (annihilation) operator for an electron with momentum $\boldsymbol{k} = (k_x, k_y)$ and spin s. In the BdG Hamiltonian, $\xi(\boldsymbol{k}) = \epsilon_{\boldsymbol{k}}\sigma_0 + \mathbf{s}\cdot\boldsymbol{\sigma}$, where $\epsilon_{\mathbf{k}} = [-2t(\cos k_x + \cos k_y) - \mu]\sigma_0$ is the kinetic term, with t the nearest-neighbour hopping integral and μ the chemical potential, $\mathbf{s}\cdot\boldsymbol{\sigma} = -\alpha(-\sin k_y, \sin k_x, 0)\cdot\boldsymbol{\sigma} = -\alpha[-\sin k_y\sigma_x + \sin k_x\sigma_y]$ is the spin-orbit term with $\mathbf{s}$ the spin-orbit vector. The term $\mathbf{B}\cdot\boldsymbol{\sigma}$ describes the Zeeman coupling of the electrons with an external magnetic field $\mathbf{B}$ and $\hat{\Delta}(\mathbf{k}) = [\Delta_s + \mathbf{d}(\mathbf{k})\cdot\sigma](i\sigma_y)$ is the superconducting gap function. The pairing vector is chosen as $\mathbf{d} = d(-\sin k_y, \sin k_x, 0)$. The simultaneous existence of s and p-wave terms is possible in the noncentrosymmetric regime with a nonzero spin-orbit term, which breaks the parity symmetry.

It is also of interest to write the Hamiltonian in real space. We can define $c_{\mathbf{r}s}^{\dagger}(c_{\mathbf{r}s})$ the creation (annihilation) operator for an electron at site $\mathbf{r} = (x, y)$ [1] of a square lattice, with spin s, such that $c_{\mathbf{r}s} = \frac{1}{\sqrt{N}}\sum_{\mathbf{k}} e^{-i\mathbf{k}\cdot\mathbf{r}} c_{\mathbf{k}s}$ with $N = N_x \times N_y$ the total number of sites and N_x and N_y the number of sites in the x and y directions, respectively. The Hamiltonian then reads

$$H = H_K + H_{SO} + H_Z + H_{SC} \tag{3.2}$$

with H_K the kinetic term, H_{SO} the spin-orbit term, H_Z the Zeeman term and H_{SC} the superconducting term. In real space these can then be written as, respectively,

$$H_K = -2t\sum_{rs}\sum_{\hat{e}_r}\left(c_{\mathbf{r}+\hat{\mathbf{e}}_r s}^{\dagger} c_{\mathbf{r}s} + c_{\mathbf{r}-\hat{\mathbf{e}}_r s}^{\dagger} c_{\mathbf{r}s}\right) - \mu\sum_{rs} c_{\mathbf{r}s}^{\dagger} c_{\mathbf{r}s} \tag{3.3}$$

[1] We note that throughout this work we will use x and y as discrete variables, ranging from 0 to $N_x - 1$ or $N_y - 1$, respectively.

$$H_{SO} = \frac{\alpha}{2}\sum_{r}\left(c^{\dagger}_{\mathbf{r}+\hat{\mathbf{e}}_x\uparrow}c_{\mathbf{r}\downarrow} - c^{\dagger}_{\mathbf{r}-\hat{\mathbf{e}}_x\uparrow}c_{\mathbf{r}\downarrow} + i\left(c^{\dagger}_{\mathbf{r}-\hat{\mathbf{e}}_y\uparrow}c_{\mathbf{r}\downarrow} - c^{\dagger}_{\mathbf{r}+\hat{\mathbf{e}}_y\uparrow}c_{\mathbf{r}\downarrow}\right) + \text{H.c.}\right) \tag{3.4}$$

$$H_Z = \sum_{rss'}(\mathbf{B}\cdot\sigma)_{ss'}c^{\dagger}_{rs}c_{rs'} \tag{3.5}$$

$$H_{SC} = \Delta_s\sum_{r}\left(c^{\dagger}_{\mathbf{r}\uparrow}c^{\dagger}_{\mathbf{r}\downarrow} + \text{H.c.}\right) + \frac{d}{2}\sum_{r}\left(c^{\dagger}_{\mathbf{r}+\hat{\mathbf{e}}_x\uparrow}c^{\dagger}_{\mathbf{r}\uparrow} - c^{\dagger}_{\mathbf{r}-\hat{\mathbf{e}}_x\uparrow}c^{\dagger}_{\mathbf{r}\uparrow} + i\left(c^{\dagger}_{\mathbf{r}-\hat{\mathbf{e}}_y\uparrow}c^{\dagger}_{\mathbf{r}\uparrow} - c^{\dagger}_{\mathbf{r}+\hat{\mathbf{e}}_y\uparrow}c^{\dagger}_{\mathbf{r}\uparrow}\right) + \text{H.c.}\right). \tag{3.6}$$

The case of study is that of a system with periodic boundary conditions along the x direction and open boundary conditions in the y direction, such as in a cylinder geometry, as represented in figure 3.1. In this case, we can also write the Hamiltonian in a mixed space, where a Fourier transform to the reciprocal space is only done in the x direction.

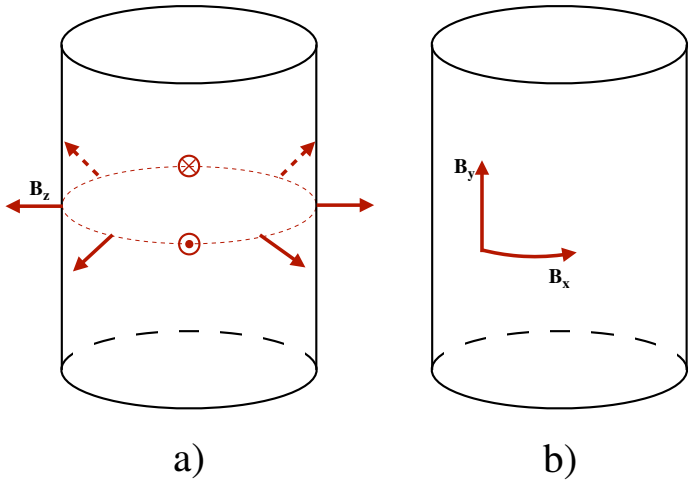

Figure 3.1: Scheme of a two-dimensional system in a cylinder geometry with a) an applied perpendicular magnetic field, b) an applied parallel magnetic field.

To write the Hamiltonian in such way, we define $c_{\mathbf{k}s} = \frac{1}{\sqrt{N_y}}\sum_y e^{ik_y y}c_{k_x,y,s}$ and [81]

$$H_{(k_x,y)} = \sum_{k_x,y}\left(c^{\dagger}_{k_x,y,\uparrow}c^{\dagger}_{k_x,y,\downarrow}c_{-k_x,y,\uparrow}c_{-k_x,y,\downarrow}\right)\hat{\mathcal{H}}_{(k_x,y)}\begin{pmatrix} c_{k_x,y,\uparrow} \\ c_{k_x,y,\downarrow} \\ c^{\dagger}_{-k_x,y,\uparrow} \\ c^{\dagger}_{-k_x,y,\downarrow}\end{pmatrix}. \tag{3.7}$$

$\hat{\mathcal{H}}_{(k_x,y)}$ is a 4×4 matrix that can be written as

$$\hat{\mathcal{H}}_{(k_x,y)} = \begin{pmatrix}\hat{A} & \hat{B} \\ \hat{C} & \hat{D}\end{pmatrix}, \tag{3.8}$$

with $\hat{A}$, $\hat{B}$, $\hat{C}$ and $\hat{D}$ given by

$$\hat{A} = \begin{pmatrix} -2t\cos k_x - \mu + B_z - t\eta_+ & \mathrm{i}\alpha \sin k_x + \frac{\alpha}{2\mathrm{i}}\eta_- + B_x - \mathrm{i}B_y \\ \mathrm{i}\alpha \sin k_x + \frac{\alpha}{2\mathrm{i}}\eta_- + B_x + \mathrm{i}B_y & -2t\cos k_x - \mu - B_z - t\eta_+ \end{pmatrix}, \tag{3.9}$$

$$\hat{B} = \begin{pmatrix} \mathrm{i}d\sin k_x + \frac{d}{2\mathrm{i}}\eta_- & \Delta_s \\ -\Delta_s & \mathrm{i}d\sin k_x - \frac{d}{2\mathrm{i}}\eta_- \end{pmatrix}, \tag{3.10}$$

$$\hat{C} = \begin{pmatrix} -\mathrm{i}d\sin k_x + \frac{d}{2\mathrm{i}}\eta_- & -\Delta_s \\ \Delta_s & -\mathrm{i}d\sin k_x - \frac{d}{2\mathrm{i}}\eta_- \end{pmatrix}, \tag{3.11}$$

$$\hat{D} = \begin{pmatrix} 2t\cos k_x + \mu - B_z + t\eta_+ & -\mathrm{i}\alpha \sin k_x + \frac{\alpha}{2\mathrm{i}}\eta_- - B_x - \mathrm{i}B_y \\ \mathrm{i}\alpha \sin k_x + \frac{\alpha}{2\mathrm{i}}\eta_- - B_x + \mathrm{i}B_y & 2t\cos k_x + \mu + B_z + t\eta_+ \end{pmatrix}, \tag{3.12}$$

and $c_y^\dagger \eta_\pm c_y = c_y^\dagger c_{y+1} \pm c_{y+1}^\dagger c_y$.

When $\mathbf{B} = 0$, the system respects the time-reversal symmetry (TRS) $\mathcal{T} = (\sigma_0 \otimes \mathrm{i}\sigma_y)K$ and the particle-hole symmetry (PHS) $\mathcal{P} = (\sigma_x \otimes \sigma_o)K$, with K the complex conjugate operator, such that

$$\begin{aligned} \mathcal{P}^{-1}\mathcal{H}(\mathbf{k})\mathcal{P} &= -\mathcal{H}^*(-\mathbf{k}) \\ \mathcal{T}^{-1}\mathcal{H}(\mathbf{k})\mathcal{T} &= \mathcal{H}^*(-\mathbf{k}) \end{aligned} \tag{3.13}$$

and $\mathcal{T}^2 = -1$, $\mathcal{P}^2 = 1$. Therefore the Hamiltonian belongs to the DII symmetry class, and if $|d| > |\Delta_s|$ the system has a nontrivial $\mathbf{Z}_2$ number, displaying gapless counter-propagating Majorana edge states (MESs) [8, 56].

We are interested in studying the system when the external magnetic field is finite, therefore in regimes where the time-reversal symmetry $\mathcal{T}$ is broken. However, the system exhibits different topological properties whether the applied magnetic field is perpendicular or parallel to the system, as will be now discussed.

3.2 Superconductor under a perpendicular magnetic field

First we consider the case in which the external magnetic field is perpendicular to the system, $\mathbf{B} = (0, 0, B_z)$ (figure 3.1 a)). The eigenvalues of the Hamiltonian are given by

$$E(\mathbf{k}) = \pm\sqrt{\epsilon_\mathbf{k}^2 + \Delta_s^2 + B_z^2 + (\mathbf{d}\cdot\mathbf{d}) + (\mathbf{s}\cdot\mathbf{s}) \pm 2\sqrt{\Delta_s^2(\mathbf{d}\cdot\mathbf{d} + B_z^2) + \epsilon_\mathbf{k}^2(\mathbf{s}\cdot\mathbf{s} + B_z^2) - 2\Delta_s\epsilon_\mathbf{k}(\mathbf{d}\cdot\mathbf{s}) + [(\mathbf{d}\times\mathbf{s})_z]}}. \tag{3.14}$$

For the present choice of the vectors $\mathbf{d}$ and $\mathbf{s}$, $[(\mathbf{d}\times\mathbf{s})_z] = 0$. The gap of the system closes when the lowest energy band's gap closes. This happens when

$$\epsilon_\mathbf{k}^2 + \Delta_s^2 + B_z^2 + (\mathbf{d}\cdot\mathbf{d}) + (\mathbf{s}\cdot\mathbf{s}) = 2\sqrt{\Delta_s^2(\mathbf{d}\cdot\mathbf{d} + B_z^2) + \epsilon_\mathbf{k}^2(\mathbf{s}\cdot\mathbf{s} + B_z^2) - 2\Delta_s\epsilon_\mathbf{k}(\mathbf{d}\cdot\mathbf{s})}, \tag{3.15}$$

which is equivalent to

$$\begin{aligned} &\epsilon_{\mathbf{k}}^2 + \Delta_s^2 = B_z^2 + \left(1 + \left(\frac{\alpha}{d}\right)^2\right)(\mathbf{d}\cdot\mathbf{d}), \\ &\epsilon_{\mathbf{k}} d\mathbf{d} = \Delta_s \alpha \mathbf{d}. \end{aligned} \tag{3.16}$$

When $d \neq 0$ this is verified when either

$$\epsilon_{\mathbf{k}} = \frac{\Delta_s}{d}\alpha \quad \wedge \quad \left(1 + \left(\frac{\alpha}{d}\right)^2\right)[\mathbf{d}\cdot\mathbf{d} - \Delta_s^2] + B_z^2 = 0 \tag{3.17}$$

or

$$\epsilon_{\mathbf{k}}^2 + \Delta_s^2 = B_z^2 \quad \wedge \quad \mathbf{d} = \mathbf{s} = 0. \tag{3.18}$$

If the magnetic field B_z is zero, only the equations 3.17 can be verified. If B_z is finite and $d > \Delta_s$ the equations 3.17 can not be verified for any values of $\mathbf{k}$, and we can only have gapless points when equations 3.18 are met. Since $\mathbf{d}$ and $\mathbf{s}$ are zero at $\mathbf{k} = (0,0), (0,\pi), (\pi,0), (\pi,\pi)$, we have a gap closing if one of the equations is satisfied:

$$(-4t-\mu)^2 + \Delta_s^2 = B_z^2, \quad \mu^2 + \Delta_s^2 = B_z^2, \quad (4t-\mu)^2 + \Delta_s^2 = B_z^2. \tag{3.19}$$

Equations 3.19 define the boundaries between regions in which the system has different topological properties. At the gap closing points the system undergoes topological transitions between phases with different Chern numbers. Two phase diagrams are presented in figure 3.2 for the values $\Delta_s = 0$ and $\Delta_s = 0.3$.

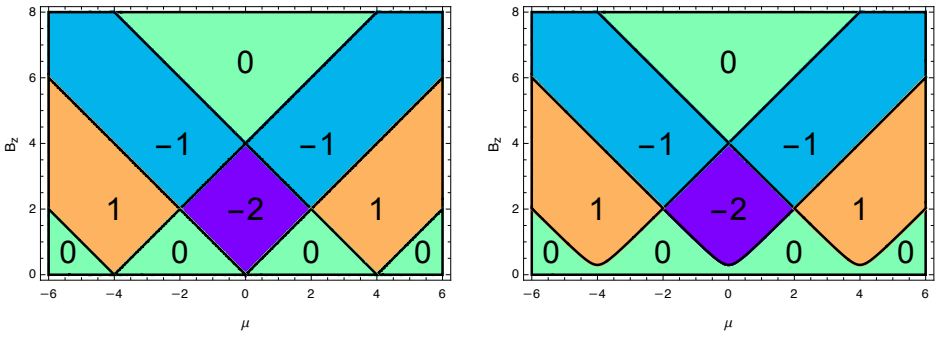

Figure 3.2: Phase diagram for the Chern number as a function of μ and B_z, with $t = 1$ and a) $\Delta_s = 0$, a) $\Delta_s = 0.3$. (Note that the gap-closing points are independent of d, but the phase diagram is only valid are in a regime where $|d| > |\Delta_s|$.)

The regimes with a Chern number of zero and $B_z < 2$, $|\mu| < 4t$ exhibit edge states, besides having $C = 0$. This can be explained by one additional topological invariant. Let us then define it. The Hamiltonian obeys a particle hole symmetry $\mathcal{P} = (\sigma_x \otimes \sigma_0)$ with

$$\mathcal{P}\mathcal{H}(\mathbf{k})\mathcal{P}^\dagger = -\mathcal{H}^*(-\mathbf{k}). \tag{3.20}$$

For the values $k_y = 0$ and $k_y = \pi$, the Hamiltonian obeys $\mathcal{H}^*(-\mathbf{k}) = \mathcal{H}(\mathbf{k})$ and thus anticommutes with $\mathcal{P}$, $\{\mathcal{H}(\mathbf{k}), \mathcal{P}\} = 0$. Therefore the basis which diagonalizes $\mathcal{P}$ anti-diagonalizes the Hamiltonian, and we may write

$$\mathcal{H}(k_x) = \begin{pmatrix} 0 & q(k_x) \\ q^\dagger(k_x) & 0 \end{pmatrix}_{k_y=0,\pi} \tag{3.21}$$

with the matrix $q(k_x)$ given by

$$q(k_x) = \begin{pmatrix} -\epsilon_{\mathbf{k}} - B_z + id\sin k_x & \Delta_s - i\alpha\sin k_x \\ -\Delta_s + i\alpha\sin k_x & -\epsilon_{\mathbf{k}} + B_z + id\sin k_x \end{pmatrix}, \tag{3.22}$$

where $\epsilon_{\boldsymbol{k}} = [-2t(\cos k_x \pm 1) - \mu]$ for $k_y = 0$ or π, respectively. We can then define a winding number $I(k_y)$ as [82]

$$I(k_y) = \frac{1}{4\pi i}\int_{-\pi}^{\pi} dk_x \,\mathrm{tr}\left[q^{-1}(k_x)\partial_{k_x} q(k_x) - q^{\dagger -1}(k_x)\partial_{k_x} q^\dagger(k_x)\right], \quad k_y = 0, \pi. \tag{3.23}$$

The phase diagram for $I(0)$ and $I(\pi)$ is presented in figure 3.3.

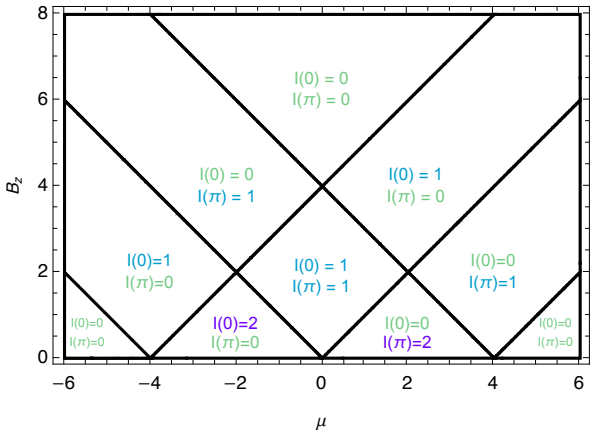

Figure 3.3: Phase diagram for the winding numbers $I(k_y = 0, \pi)$ as a function of μ and B_z, with $t = 1$ and $\Delta_s = 0$ and for $d > 0$.

The additional winding number $I(k_y)$ carries information about the edge states in the system. It is found that for a cylindrical system with OBC along the x direction and PBC along the y direction the number of zero-energy edge states at $k_y = 0$ or $k_y = \pi$ coincides with the respective absolute value of $I(k_y)$. This result translates to the case which is discussed in this work (OBC along y and PBC along x), since the energy spectrum in 3.14 remains unchanged for the transformation $k_x \leftrightarrow k_y$ for $[(\mathbf{d} \times \mathbf{s})_z] = 0$. Therefore, the winding numbers $I(0)$ and $I(\pi)$ can successfully predict the number of edge states at $k_x = 0$ or $k_x = \pi$, respectively. In figure 3.3, we see that for some phases the Chern number is zero but either $I(0)$ or $I(\pi)$ are equal to 2, and the phase is topologically nontrivial. Gapless edge states will emerge inside such phases, despite being characterized by $C = 0$, in contrast with the regions where the Chern number is zero and $I(k_y = 0, \pi) = 0$. In this case, there are no gapless edge states.

We now briefly turn to the discussion of an added parallel magnetic field, while inside the phases

depicted in figure 3.2 for $\Delta_s = 0$, to discuss the robustness of the edge states. If a magnetic field in the y direction is added, B_y, the winding numbers $I(0)$ and $I(\pi)$ become meaningless since the relation $\mathcal{H}^*(-\mathbf{k}) = \mathcal{H}(\mathbf{k})$ is broken. However, for an added magnetic field in the x direction, B_x, $I(k_y)$ remains well defined. In a system with PBC in y and OBC in x, the added magnetic field in the y direction, B_y, destroys the edge states by opening a gap at zero energy, while the edge states are found to be robust under a magnetic field in the x direction. In this case the gapless edge states are protected by the topological invariant $I(k_y)$, as is discussed in ref. [56]. Let us now turn to the geometry of interest, a cylinder geometry with PBC in x and OBC in y. An added magnetic field B_y still forbids the definition of $I(k_y)$, but keeps the zero-energy edge states at $k_x = 0$ and $k_x = \pi$ stable, while a magnetic field in the x direction destroys such states. Hence $I(k_y)$ is only useful to understand the gapless edge states in the present problem geometry if $\mathbf{B} = (0, 0, B_z)$, which is understandable since an added parallel magnetic field breaks the invariance of the bulk energy spectra under the transformation $k_x \leftrightarrow k_y$. This also suggests that the gapless edge states in the present problem geometry should be protected by an analogous winding number defined from the same symmetry, say, $I(k_x)$, reflecting the behaviour of the edge states under B_y or B_x. However, the relation $\mathcal{H}^*(-\mathbf{k}) = \mathcal{H}(\mathbf{k})$ is broken for any value of k_x, making it impossible to define an invariant in the same way as $I(k_y)$.

Despite the fact that $I(k_y)$ loses its meaning if any magnetic field B_y is applied, this is not true for the Chern number. Figure 3.4 shows the phase diagram for the Chern number as a function of B_z and B_y at three different values of μ. It was found that in this case the Chern number depends only on the value of $\sqrt{B_y^2 + B_z^2}$. Also note that the diagram only concerns values of $B_z > 0$, excluding the points where $B_z = 0$ and $B_y \neq 0$.

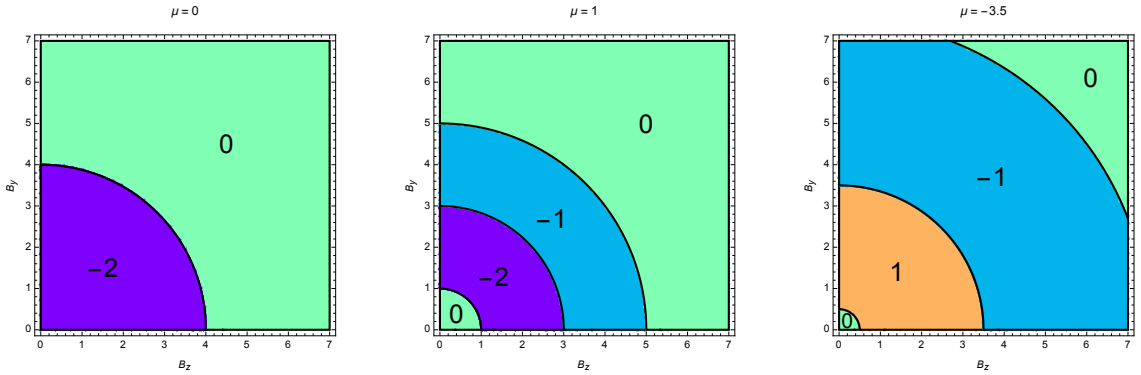

Figure 3.4: Phase diagram for $(B_z > 0, B_y)$ for the Chern number obtained numerically at $\mu = 0$, $\mu = 1$ and $\mu = -3.5$ for $\Delta_s = 0$.

3.3 Superconductor under a parallel magnetic field

Now let us consider the case in which the applied magnetic field is parallel to the system, $\mathbf{B} = (B_x, B_y, 0)$. Taking now the s-wave term Δ_s and the spin-orbit term α to be zero, the eigenvalues of the Hamiltonian are given by

$$E(\mathbf{k}) = \pm\sqrt{\mathbf{d}\cdot\mathbf{d} + \epsilon_{\mathbf{k}}^2 + \mathbf{B}\cdot\mathbf{B} \pm 2\sqrt{\epsilon_{\mathbf{k}}^2(\mathbf{B}\cdot\mathbf{B}) + (\mathbf{B}\cdot\mathbf{d})^2}}. \tag{3.24}$$

The gap closing points $E(\mathbf{k}) = 0$ are the solutions of the equation

$$\mathbf{d}\cdot\mathbf{d} + \epsilon_{\mathbf{k}}^2 + \mathbf{B}\cdot\mathbf{B} = 2\sqrt{\epsilon_{\mathbf{k}}^2(\mathbf{B}\cdot\mathbf{B}) + (\mathbf{B}\cdot\mathbf{d})^2}, \tag{3.25}$$

which is equivalent to the two equations being simultaneously satisfied

$$\begin{aligned} \mathbf{d}\cdot\mathbf{d} + \epsilon_{\mathbf{k}}^2 &= \mathbf{B}\cdot\mathbf{B}, \\ (\mathbf{B}\cdot\mathbf{B})(\mathbf{d}\cdot\mathbf{d}) &= (\mathbf{B}\cdot\mathbf{d})^2. \end{aligned} \tag{3.26}$$

Equations 3.26 simplify if we consider the magnetic field aligned with one of the axes. Let us take the magnetic field aligned with the y direction, $\mathbf{B} = (0, B_y, 0)$. In this case, the second equation simplifies to $\sin k_y = 0$ which implies the bulk gap will close at $k_{y,0} = n\pi$, $n \in \mathbb{Z}$, provided there are values of k_x that satisfy the equations

$$d^2 \sin^2 k_x + (-2t(\cos k_x \pm 1) - \mu)^2 = B_y^2. \tag{3.27}$$

Considering the geometry of the problem (figure 3.1) is mostly interesting to study the case where $\mathbf{B}$ is aligned in the y direction, since there will be gap closings along the k_x axis.

In figure 3.5 the bulk energy spectrum is presented for several parameter values with $\mathbf{B} = (0, B_y, 0)$.

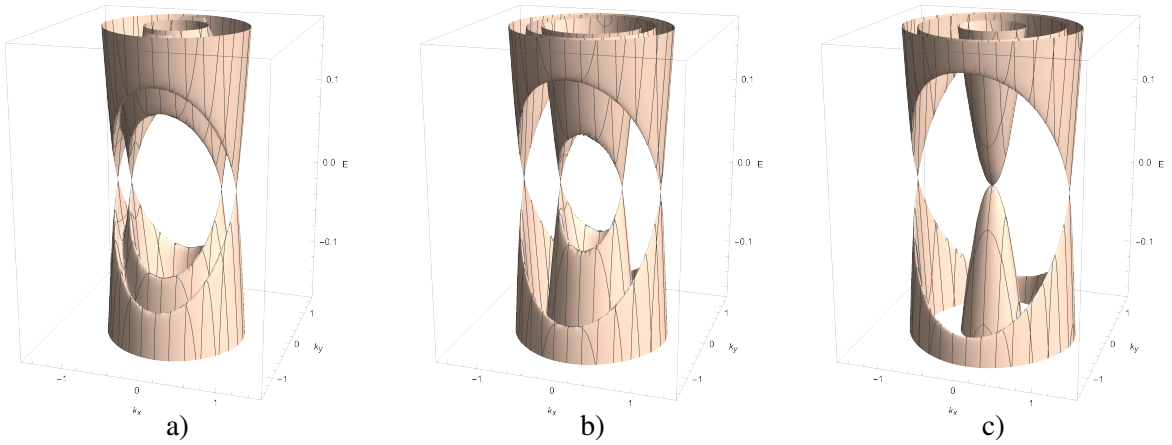

Figure 3.5: Bulk energy spectrum for $t = 1$, $d = t/6$, $\mu = 3d - 4t$ and a) $B_y = d$, b) $B_y = 2d$, c) $B_y = 3d$ for $k_x \in [-\pi/2, \pi/2]$ and for the energy range $E \in [-d, d]$.

3.3.1 Winding Number and Majorana Flat Bands

Let us consider a generic parallel magnetic field of the form $\mathbf{B} = (B_x, B_y, 0)$. In this case the system no longer respects time-reversal symmetry. We can, however, take k_x as a fixed parameter of the Hamiltonian and find a set of symmetries that are only satisfied in the y direction. It is found that the Hamiltonian respects the symmetries

$$\begin{aligned} \mathcal{T}_{k_y}^{-1}\mathcal{H}(k_x, k_y)\mathcal{T}_{k_y} &= \mathcal{H}(k_x, -k_y) \\ \mathcal{P}_{k_y}^{-1}\mathcal{H}(k_x, k_y)\mathcal{P}_{k_y} &= -\mathcal{H}(k_x, -k_y) \end{aligned} \tag{3.28}$$

where $\mathcal{T}_{k_y} = (\sigma_z \otimes \sigma_z)K$ and $\mathcal{P}_{k_y} = (\sigma_y \otimes \sigma_y)K$ are, respectively, defined as a "time-reversal-like" symmetry and a "particle-hole-like" symmetry (here K is the complex conjugate operator) [8] with $\mathcal{T}_{k_y}^2 = \mathcal{P}_{k_y}^2 = 1$. From these we can define a third chiral-like symmetry, $\mathcal{S}_{k_y} = \mathcal{T}_{k_y}\mathcal{P}_{k_y}$:

$$\mathcal{S}_{k_y}^{-1}\mathcal{H}(k_x, k_y)\mathcal{S}_{k_y} = -\mathcal{H}(k_x, k_y). \tag{3.29}$$

Since we have that $\mathcal{T}_{k_y}^2 = \mathcal{P}_{k_y}^2 = 1$, the Hamiltonian belongs to the BDI symmetry class and, since the problem is effectively reduced to one dimension, the system can be characterized by an integer topological invariant. We can then take a similar approach to what is done to define $I(k_y)$ in the case $\mathbf{B} = (0, 0, B_z)$, by writing the Hamiltonian in the basis where $\mathcal{S}_{k_y}$ is diagonal. The Hamiltonian then takes the anti-diagonal form

$$\tilde{\mathcal{H}}_{k_x}(k_y) = \begin{pmatrix} 0 & A_{k_x}(k_y) \\ A_{k_x}^{\dagger}(k_y) & 0 \end{pmatrix} \tag{3.30}$$

with

$$A_{k_x}(k_y) = \begin{pmatrix} -\epsilon_{\boldsymbol{k}} & d\sin k_y + id\sin k_x + iB_y - B_x \\ -d\sin k_y + id\sin k_x - iB_y - B_x & -\epsilon_{\boldsymbol{k}} \end{pmatrix}. \tag{3.31}$$

We can now define a quantity $\theta(k_y)$ for which we can calculate a winding number, $\mathcal{W}$:

$$z(k_y) = e^{i\theta(k_y)} = \frac{\mathrm{Det}\left[A_{k_x}(k_y)\right]}{\left|\mathrm{Det}\left[A_{k_x}(k_y)\right]\right|}, \tag{3.32}$$

and the winding number is obtained as

$$\begin{aligned} \mathcal{W} &= -\frac{i}{\pi}\int_{ky=0}^{ky=\pi}\frac{dz(k_y)}{z(k_y)} = \\ &= \frac{i}{\pi}\left[\log\left(\frac{sgn(\mathcal{M}(k_y=0))}{sgn(\mathcal{M}(k_y=\pi))}\right)\right] \end{aligned} \tag{3.33}$$

with

$$\mathcal{M}(k_x, k_y) = [\mu + 2t(\cos k_x + \cos k_y)]^2 + d^2\sin^2 k_x - B_y^2 + B_x^2. \tag{3.34}$$

From equation 3.33 it is found that $|\mathcal{W}| = 1$ in the regimes where $\mathcal{M}(k_x, k_y = 0)$ and $\mathcal{M}(k_x, k_y = \pi)$ have opposite signs, $\mathcal{M}(k_x, k_y = 0)\,\mathcal{M}(k_x, k_y = \pi) < 0$. In the regimes with $|\mathcal{W}| = 1$ the system has

a topological nature and Majorana flat bands appear, as is shown in figure 3.6. We can also see from equation 3.34 that $\mathcal{M}(k_x, k_y = 0)$ and $\mathcal{M}(k_x, k_y = \pi)$ can only have opposite signs if $|B_y| > |B_x|$, which means this is a necessary condition for the appearance of MFBs.

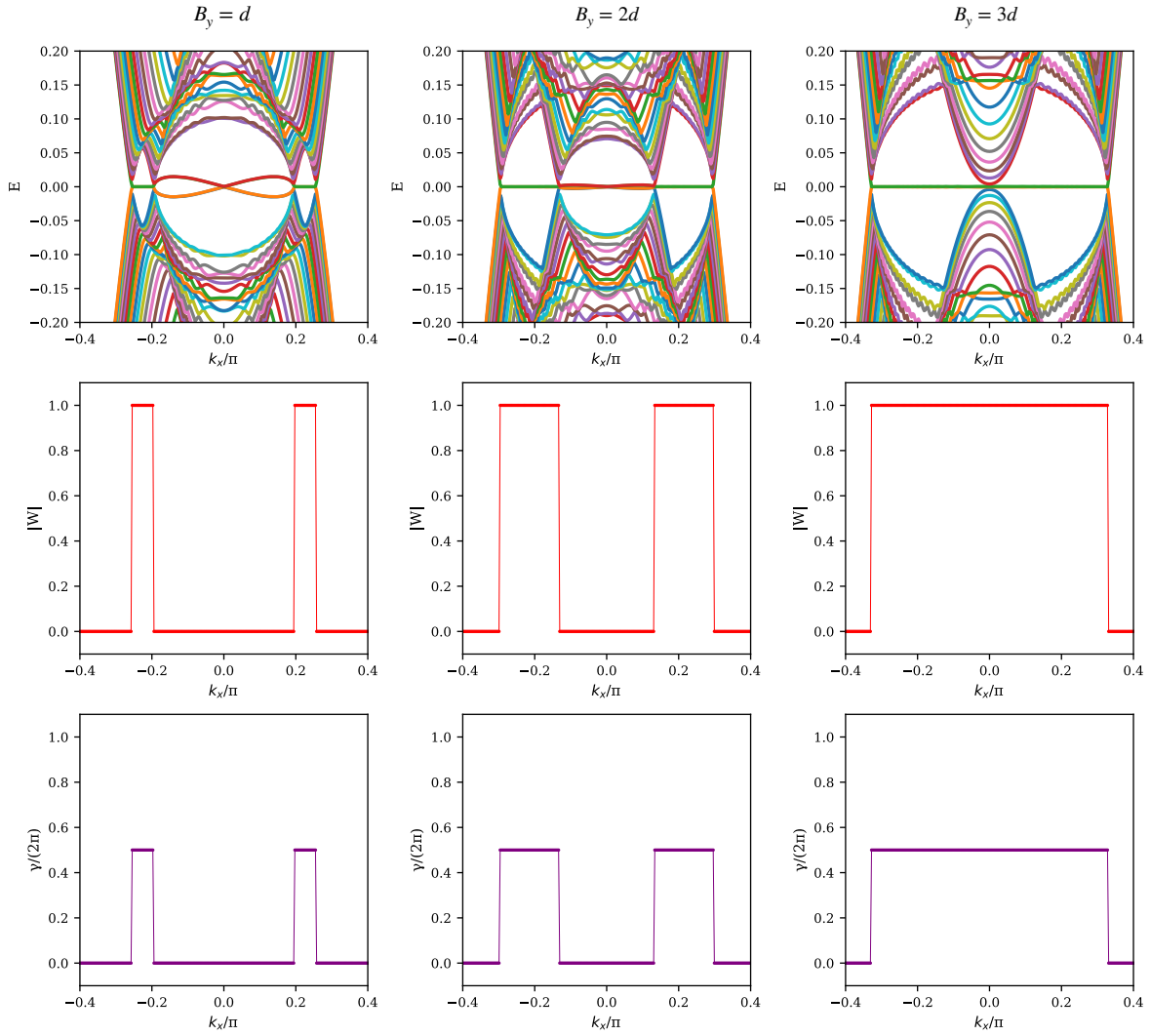

Figure 3.6: Energy spectrum evolution for a system with 76 sites in y and edges at $y = 0$ and $y = 75$ for different values of B_y vs. absolute value of the winding number $\mathcal{W}$ and normalized Berry phase $\gamma/(2\pi)$ as a function of k_x. The values of the parameters are $t = 1$, $d = t/6$, $\mu = 3d - 4t$ and $B_y = d$ (left), $B_y = 2d$ (middle), $B_y = 3d$ (right).

The chiral-like symmetry that protects the flat bands is broken by either a non-zero s-wave pairing term Δ_s or a non-zero spin-orbit term α. A finite perpendicular magnetic field B_z is also found to break the chiral-like symmetry. This means that, while a broken time-reversal symmetry is necessary for MFBs to exist, the magnetic field must be in-plane with the system, and also subject to the condition $|B_y| > |B_x|$ (if we consider OBCs in the y direction and PBCs in the x direction).

Besides being characterized by a nontrivial value of the winding number $\mathcal{W}$, the regimes with Majorana flat bands also reveal a quantized value of the Berry phase. The Berry phase is calculated numerically by discretizing the Brillouin zone in N points in the y direction, with $k_y \in [-\pi, \pi]$. For each

fixed value of k_x, a link variable is defined as $U(k_{y_i}) = \det[\mathbf{U}(k_{y_i})]$, with $\mathbf{U}(k_{y_i})$ a matrix with elements

$$\mathbf{U}_{n,m}(k_{y_i}) = \psi_n^*(k_{y_i})\psi_m(k_{y_{i+1}}) \tag{3.35}$$

where the indices n and m take values between 1 and $\mathcal{N}$ with $\mathcal{N} = 4$ being the size of the Hamiltonian matrix (equation 3.1) and the number of eigenvectors, denoted by ψ, for each pair (k_x, k_y). The Berry phase can then be calculated as [65, 83]

$$\gamma = -\mathrm{i}\sum_{i=1}^{N} \log U(k_{y_i}). \tag{3.36}$$

It was shown in [8] that MFBs induce a nearly quantized zero bias conductance (ZBC) in a junction between a normal lead and a p-wave superconductor. When B_y is such that the gap closes and MFBs appear, the ZBC becomes nearly quantized at a value of $\frac{2e^2}{h}N_c$, with $N_c = 4$, where N_c is the number of channels in the normal lead. This result was obtained in the presence of on-site Gaussian disorder, suggesting robustness of MFBs against perturbations.

3.3.2 Domain of Flat Band Existence

As stated above, flat bands appear in the regime where $\mathcal{M}(k_x, k_y = 0)\,\mathcal{M}(k_x, k_y = \pi) < 0$ with $\mathcal{M}(k_x, k_y)$ given by equation 3.34. We will now prove that, while we will consider a reduced parameter range, the appearance of zero-energy bands is not exclusive to the latter.

From equation 3.34, we can note that we always have $\mathcal{M}(k_x, k_y = 0) < \mathcal{M}(k_x, k_y = \pi)$ if $\mu < -2t\cos k_x$ and $\mathcal{M}(k_x, k_y = 0) > \mathcal{M}(k_x, k_y = \pi)$ if $\mu \geq -2t\cos k_x$. So the conditions for the flat bands to exist can be summarized in (with $\tilde{B}^2 = B_y^2 - B_x^2$ and $|B_y| > |B_x|$):

- (1) $\mu \geq 2t$

$$\begin{gathered}
\mathcal{M}(k_x, k_y = 0) > 0 \wedge \mathcal{M}(k_x, k_y = \pi) < 0 \Leftrightarrow \\
\left[\mu + 2t(\cos k_x + 1)\right]^2 + d^2 \sin^2 k_x - \tilde{B}^2 > 0 \wedge \left[\mu + 2t(\cos k_x - 1)\right]^2 + d^2 \sin^2 k_x - \tilde{B}^2 < 0 \Leftrightarrow \\
\left[\mu + 2t(\cos k_x + 1)\right]^2 + d^2 \sin^2 k_x > \tilde{B}^2 \wedge \left[\mu + 2t(\cos k_x - 1)\right]^2 + d^2 \sin^2 k_x < \tilde{B}^2 \Leftrightarrow \\
\left[\mu + 2t(\cos k_x + 1)\right]^2 + d^2 \sin^2 k_x > \tilde{B}^2 > \left[\mu + 2t(\cos k_x - 1)\right]^2 + d^2 \sin^2 k_x
\end{gathered} \tag{3.37}$$

- (2) $\mu \leq -2t$

$$\begin{gathered}
\mathcal{M}(k_x, k_y = 0) < 0 \wedge \mathcal{M}(k_x, k_y = \pi) > 0 \Leftrightarrow \\
\left[\mu + 2t(\cos k_x - 1)\right]^2 + d^2 \sin^2 k_x - \tilde{B}^2 > 0 \wedge \left[\mu + 2t(\cos k_x + 1)\right]^2 + d^2 \sin^2 k_x - \tilde{B}^2 < 0 \Leftrightarrow \\
\left[\mu + 2t(\cos k_x - 1)\right]^2 + d^2 \sin^2 k_x > \tilde{B}^2 > \left[\mu + 2t(\cos k_x + 1)\right]^2 + d^2 \sin^2 k_x
\end{gathered} \tag{3.38}$$

- (3) $-2t < \mu < 2t$

$$\begin{gathered}([\mu + 2t\,(\cos k_x + 1)]^2 + d^2 \sin^2 k_x > \tilde{B}^2 > [\mu + 2t\,(\cos k_x - 1)]^2 + d^2 \sin^2 k_x) \\ \vee \\ ([\mu + 2t\,(\cos k_x - 1)]^2 + d^2 \sin^2 k_x > \tilde{B}^2 > [\mu + 2t\,(\cos k_x + 1)]^2 + d^2 \sin^2 k_x)\end{gathered} \tag{3.39}$$

For the set of parameters $t = 1$, $d = t/6$, $\mu = 3d - 4t = \frac{t}{2} - 4t = -\frac{7}{2}t$, which will we consider several times throughout this work, we have $\mu < -2t \cos k_x$ for all k_x; therefore we are in the region of the second inequality, and we can plot the values of $\tilde{B}$ vs k_x for which we will have flat bands at a certain region of k_x:

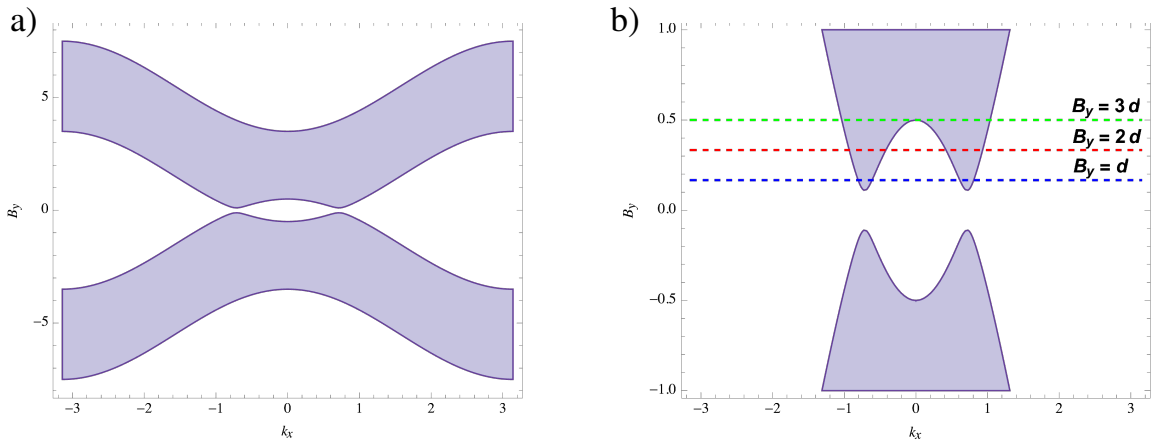

Figure 3.7: a) Domain of MFBs (shaded region) for B_y vs. k_x for the parameter values $t = 1$, $d = t/6$, $\mu = -3.5$. b) Closeup of a) in the region $B_y \in [-1, 1]$. The three dashed lines represent the values $B_y = d$ (blue), $B_y = 2d$ (red) and $B_y = 3d$ (red) which correspond to the values of B_y of the energy spectra presented in figure 3.6.

Since the Majorana flat bands are topologically characterized by a nonzero winding number, equations 3.37, 3.38 and 3.39 also define the regions where the superconductor is in a nontrivial regime with $|\mathcal{W}| = 1$. Furthermore, since MFBs can only appear in a gapless phase, equations 3.37, 3.38 and 3.39 also define regimes of the superconductor where the bulk is gapless as a function of the in-plane magnetic field. In figure 3.8 some other examples are presented, as a function of B_y, for zero and finite B_x (represented by a red dashed line).

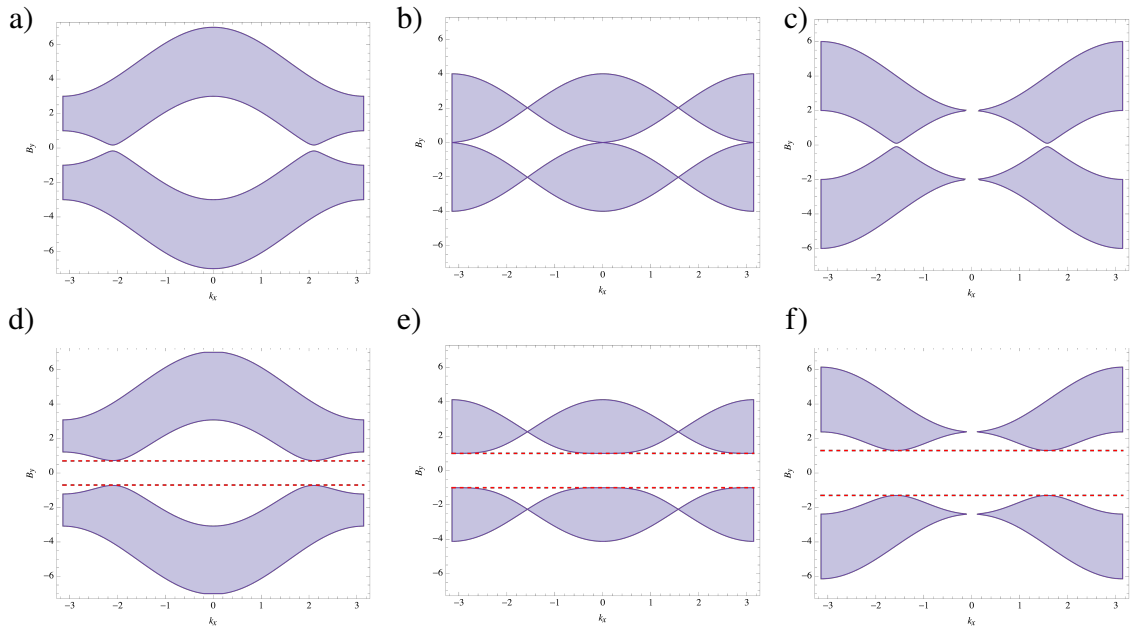

Figure 3.8: Domain of MFBs (shaded region) for B_y vs. k_x. The graphs a), b) and c) have $B_x = 0$ while the graphs d), e) and f) have $B_x \neq 0$, represented by red dashed lines. The values of the parameters are a) $t = 1, \mu = 3, d = 0.2, B_x = 0$. b) $t = 1, \mu = 0, d = 0.3, B_x = 0$. c) $t = 1, \mu = -2, d = 0.1, B_x = 0$; d), e) and f) are the same as a), b) and c), respectively, except for d) $B_x = 0.7$, e) $B_x = 1$, f)$B_x = 1.3$.

3.3.3 Unidirectional Majorana Edge States

As discussed above, the chiral-like symmetry $\mathcal{S}_{k_y}$ is broken by either a finite value of the spin orbit term α or the s-wave pairing term Δ_s. When these terms are introduced, for a certain range of the magnetic field B_y, the Majorana flat bands will acquire a slope and give origin to unidirectional edge modes. Figure 3.9 shows the energy spectrum for $t = 1$, $d = t/6$, $\mu = 3d - 4t$, $\alpha = 0.2d$ and $\Delta_s = 0.3d$, and a visual representation of the unidirectional edge modes in the superconductor along with the magnetic field B_y. As in the case of MFBs, unidirectional MESs induce a nearly quantized ZBC in a junction between a normal lead and a p-wave superconductor, at a value of $\frac{2e^2}{h}$ since there is only one zero energy edge mode in a MES regime [8]. Note that the edge modes create a right moving current on the edges that is balanced by a left moving current on the bulk, so that the net current of the system is zero. Since this is only possible for a gapless system, the unidirectional MESs can only appear if the bulk is gapless.

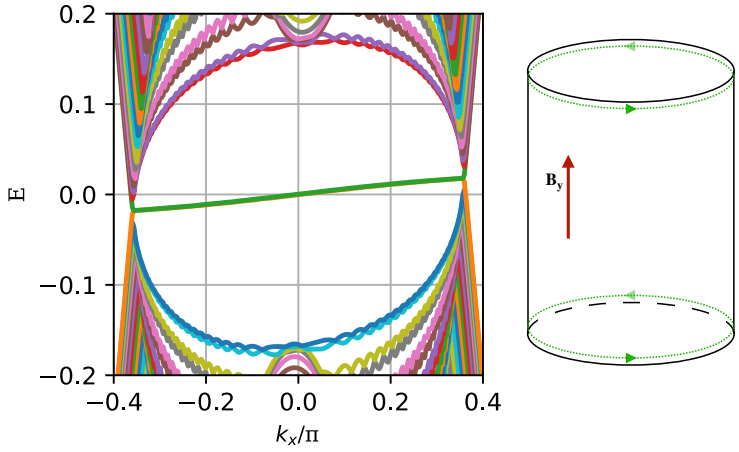

Figure 3.9: Left: Energy spectrum for a system with 76 sites in y and edges at $y = 0$ and $y = 75$ for the parameter values $t = 1$, $d = t/6$, $\mu = 3d - 4t$, $By = 4d$, $\alpha = 0.2d$. Right: representation of the unidirectional edge modes in the superconductor with a cylindrical geometry.

4

Disordered two-dimensional topological superconductor

We now add disorder to the model described in chapter 3. The real space Hamiltonian is now written as

$$H = H_K + H_{SO} + H_Z + H_{SC} + \underline{H_D} \tag{4.1}$$

where H_D is a new term describing the disorder, given by

$$H_D = -\sum_{rs} \Lambda(\mathbf{r}) c^\dagger_{rs} c_{rs}. \tag{4.2}$$

$\Lambda(\mathbf{r})$ is the disorder term, and we consider disorder of two types:

1. Anderson disorder, where the disorder is random at each site and the random values vary (with equal probability) within an interval:
$$\Lambda(\mathbf{r}) \in [-\lambda, \lambda]. \tag{4.3}$$

2. Aubry-André disorder, where the disorder term is a quasi-periodic potential of the form:
$$\Lambda(\mathbf{r}) = \lambda \cos(2\pi\alpha f(\mathbf{r}) + \phi) \tag{4.4}$$
with $f(\mathbf{r})$ a function of the lattice sites, $\alpha = \frac{\sqrt{5}-1}{2}$ the inverse golden ratio, and ϕ a phase between 0 and 2π.

It will also be of interest to study the system in a mixed space, where the Hamiltonian is written as in equation 3.7. If disorder is introduced the matrix $\hat{\mathcal{H}}_{(k_x,y)}$ is modified as

$$\hat{\mathcal{H}}_{(k_x,y)} \to \hat{\mathcal{H}}_{(k_x,y)} + \begin{pmatrix} \hat{E} & 0 \\ 0 & \hat{F} \end{pmatrix} \tag{4.5}$$

where $\hat{E}$ and $\hat{F}$ are 2×2 matrices given by

$$\hat{E} = \begin{pmatrix} -\Lambda(y) & 0 \\ 0 & -\Lambda(y) \end{pmatrix}, \quad \hat{F} = \begin{pmatrix} \Lambda(y) & 0 \\ 0 & \Lambda(y) \end{pmatrix} \tag{4.6}$$

and $\Lambda(y)$ is the disorder term which can be of the form of either equation 4.3 or equation 4.4, with the exception that the potential can only vary in the y direction.

4.1 Quasi-disorder and Anderson disorder effects in real space

The effects of Aubry-André and Anderson disorder are studied in a real space system. Different spatial configurations are considered: the case of disorder that is only localized at the edges, as well as disorder that is introduced in all space. The numerical study of the disordered system in real space involves a diagonalization of a matrix of size $(4 \times N_x \times N_y) \times (4 \times N_x \times N_y)$ for each disorder configuration.

4.1.1 Edge disorder

The case where disorder is localized at the edges is especially interesting if we aim to disturb the edge states that appear in the various regimes. We consider disorder localized at $y = 0$ and $y = N_y$ and varying along the x direction, with $(N_x \times N_y)$ being the system size. A system with $41 \times 41 = 1681$ sites (with $N_x = N_y$) is studied, and we consider periodic boundary conditions along x and open boundary conditions along y.

Two types of disorder are considered:

- Type I: Anderson disorder, such as in equation 4.3;
- Type II: Aubry-André disorder such as in equation 4.4 but where the potential is modulated in the x direction, such that

$$\Lambda(x, y = 0, N_y) = \lambda \cos(2\pi\alpha x + \phi). \tag{4.7}$$

Here we limit ourselves to the cases where the magnetic field **B** is aligned in the y direction and consider either p-wave pairing symmetry or combined s and p-wave pairings when the spin-orbit term is finite. We take the fixed values $t = 1, d = t/6, \mu = 3d - 4t$, and consider three cases in detail: the case in which a magnetic field $B_y = 0.5d$ is added, such that the system is in a phase with a gapped bulk but gapless edge states; an added magnetic field of $B_y = 3.5d$, where the system has a gapless bulk and is in the MFB regime; and the noncentrosymmetric case with $B_y = 4d$ and added $s-$wave pairing and spin-orbit terms, $\Delta_s = 0.3d$ and $\alpha = 0.2d$, where the system has a gapless bulk and MESs.

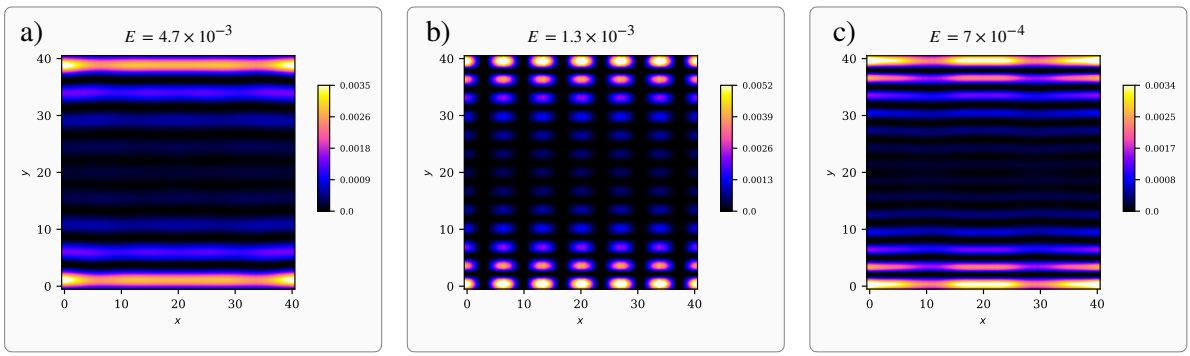

Figure 4.1: Typical edge states of the clean system, at $t = 1$, $d = t/6$, $\mu = -3.5$ and a) $B_y = 0.5d$, b) $B_y = 3.5d$, c) $B_y = 4d$, $\alpha = 0.2d$, $\Delta_s = 0.3d$.

Anderson edge disorder

In figure 4.2 the values of the IPR averaged over the lowest 10 positive energy states and highest 10 negative energy states for the three parameter cases described above are shown in a), and the average value of the IPR for the remaining states is shown in b). Note that as disorder is introduced level crossings will occur, hence the ten lowest energy states will not necessarily be the same as disorder is increased. At some point we can have crossings with bulk states which collapse to lower energies. From inspection of the wavefunctions this effect was found to be negligible in the considered range, and this distinction allows us to see how the edge localized, lower energy states are affected differently from the average of the bulk system. From b) we see that the bulk states, and the system as a whole, are almost unaffected by the introduced edge disorder. Also, from calculations of the DOS (not shown here) we see that the DOS remains almost constant, with only a slight increase at zero energy. This is in agreement with the result in b) showing the bulk states are not greatly affected from disorder at the edges. As it can be confirmed in figure a), the localization happens mostly on lower energy states. From figure a) we also see that for the system with $B_y = 0.5d$ the low energy states become more localized with increased disorder in relation to the states in the MFB and MESs regimes, which appear to be more robust at higher values of disorder.

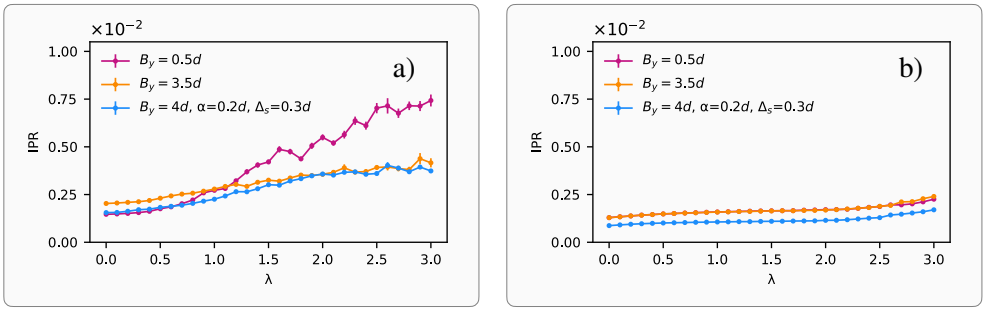

Figure 4.2: a) IPR averaged over the lowest 10 positive energy states and highest 10 negative energy states, vs. Anderson edge disorder strength λ (Type I). b) IPR averaged over the remaining states vs. disorder strength λ. The results are averaged over 10 disorder configurations.

In figure 4.3 we show three wavefunctions which represent low-energy edge states at three different values of disorder, a) $\lambda = 0.5$, b) $\lambda = 1.0$, and c) $\lambda = 2.7$. These states are shown for the noncentrosymmetric case, with $t = 1$, $d = t/6$, $\mu = -3.5$, $B_y = 4d$, $\alpha = 0.2d$ and $\Delta_s = 0.3d$. We also show the wavefunctions at the fixed values of y which correspond to the edges, $y = 0$ and $y = 40$. For the case in a) with $\lambda = 0.5$ we see that the state already lost its periodic modulation along the edges, which is easily seen in the cuts at $y = 0$ and $y = 40$. In b) we see an intermediate state, and in c) the state is already mostly localized on the edge at $y = 40$. We found that initially the edge states follow a similar behaviour in both edges. At higher values of disorder the states become significantly more localized in only one edge. It is equally likely for the states to localize at either edge, since it depends on the random disorder configuration. Note that the figures in a), b) and c) do not necessarily correspond to the evolution of the same state.

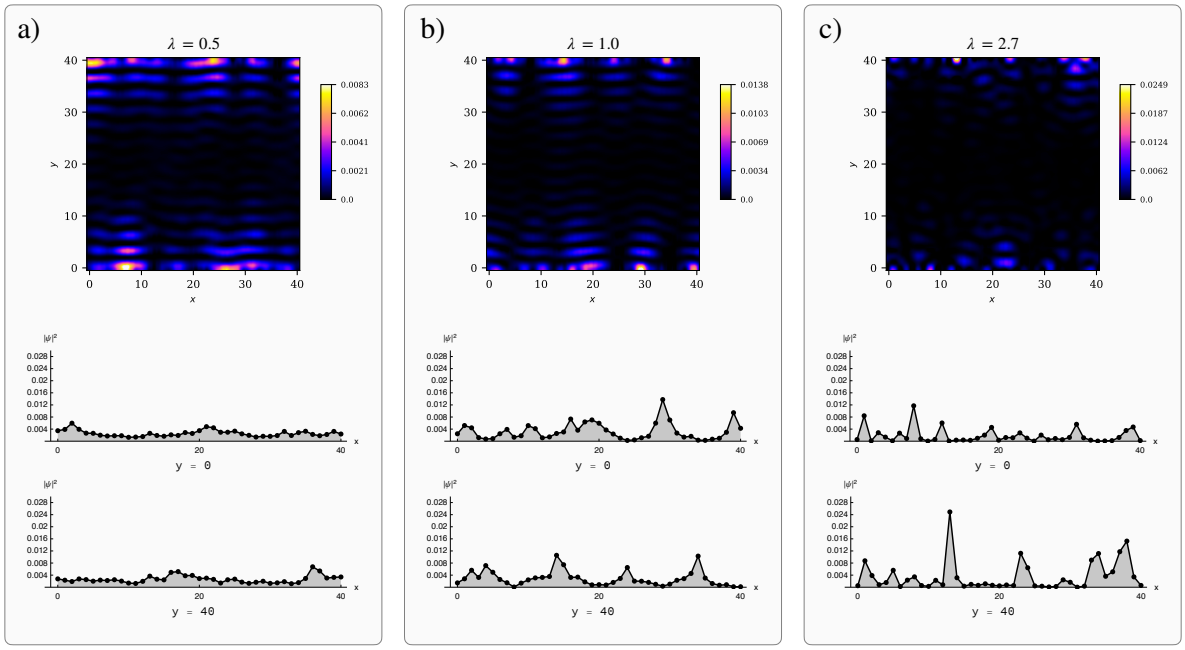

Figure 4.3: Disordered edge states for $t = 1$, $d = t/6$, $\mu = -3.5$, $B_y = 4d$, $\alpha = 0.2d$ and $\Delta_s = 0.3d$, subject to Anderson edge disorder. The wavefunctions have energies a) $E = 8 \times 10^{-4}$, b) $E = 8 \times 10^{-4}$ and c) $E = 9 \times 10^{-4}$.

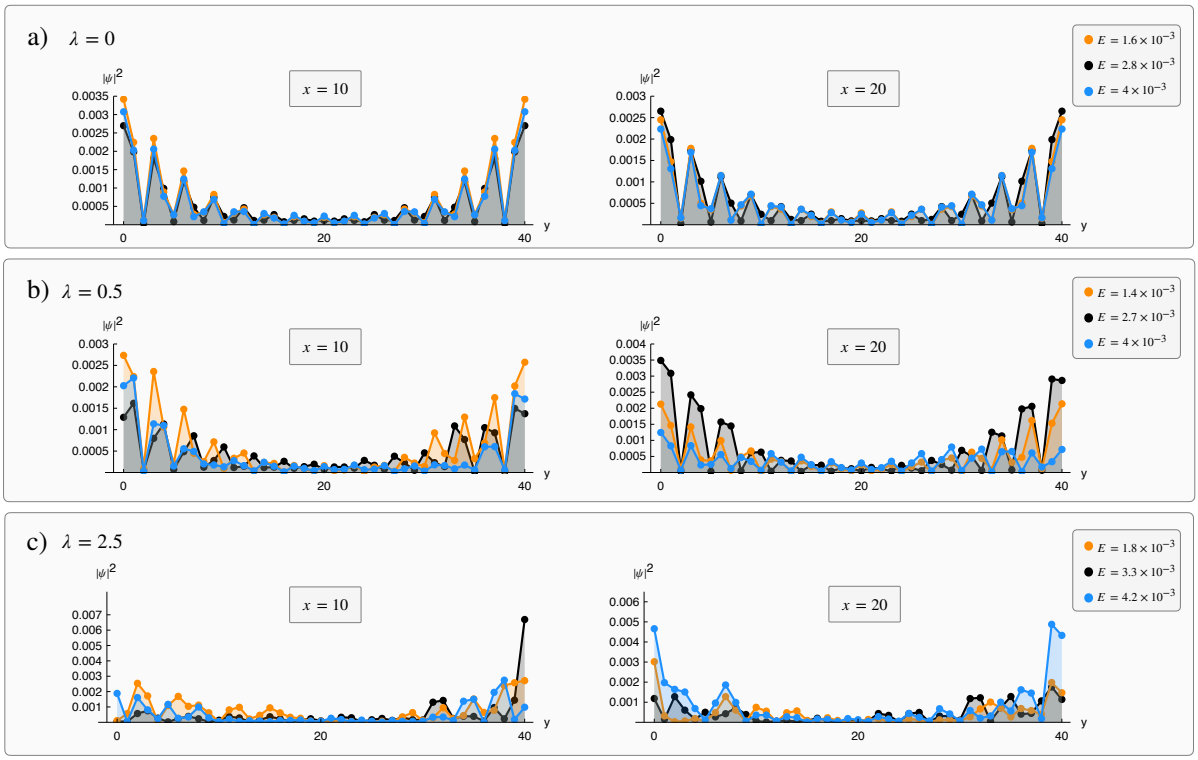

Figure 4.4: Disordered edge states for $t = 1$, $d = t/6$, $\mu = -3.5$, $B_y = 4d$, $\alpha = 0.2d$ and $\Delta_s = 0.3d$, subject to Anderson edge disorder. Here the states are shown at fixed values of x, perpendicularly to the direction of the edges, showing the impact of edge disorder on the bulk layers.

In the clean system the edge states are localized at both edges but decay exponentially (although

with zeros at some sites) towards the bulk in the y direction, while being either constant or with a periodic modulation in the x direction (in which the system obeys periodic boundary conditions), as is seen in figure 4.1. The introduced disorder is modulated along the x direction on the edges, therefore we expect localization to happen on the edge layers in a way that is reminiscent of a periodic system subject to Anderson disorder in one dimension. One question to ask is what effect the edge disorder will have in the y direction. From figure 4.3 we see that the subsequent layers are also affected by the edge disorder. Particularly, in figure 4.3 b), at the values of x in which the wavefunction becomes more localized at the edges, the same effect is seen on the next layers. In c), there is some contribution of the state on the bulk for the values of x not corresponding to that in which the wavefunction becomes more localized at the edges. In figure 4.4 we show the evolution of edge states with disorder for the noncentrosymmetric case, taking fixed values of x and for a) $\lambda = 0$, b) $\lambda = 0.5$, c) $\lambda = 2.5$. At $\lambda = 0$ we see the typical decay towards the bulk. Note that for bigger system sizes we expect this decay to happen closer to the edges and with less penetration on the bulk layers. In b), for $\lambda = 0.5$, we see that the localization of the wavefunction along the edge affects the remaining layers. Taking the wavefunction at $E = 4\times10^{-3}$ (blue), we see that at $\lambda = 0.5$ it remains localized on the edges for $x = 10$, but for $x = 20$ the contribution of the wavefunction drops not only at the edge but also at the layers towards the bulk. For higher values of disorder, as in c) $\lambda = 2.5$, we see that the modulated decay seen previously no longer remains, and that for values of x at which no localization occurs on the edges, the contribution on the bulk can increase. See for instance the wavefunction in c) at $E = 4.2 \times 10^{-3}$ (blue), where at $x = 10$ the wavefunction at $y = 40$ (edge) and the next layer is nearly zero, but the contribution increases for the subsequent layers.

Aubry-André edge disorder

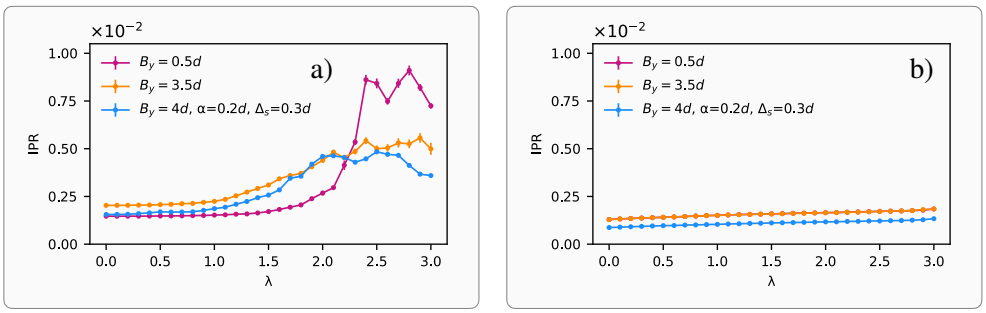

Figure 4.5: a) IPR averaged over the lowest 10 positive energy states and highest 10 negative energy states, vs. Aubry-André edge disorder strength λ (Type II). b) IPR averaged over the remaining states vs. disorder strength λ. The results are averaged over 10 disorder configurations.

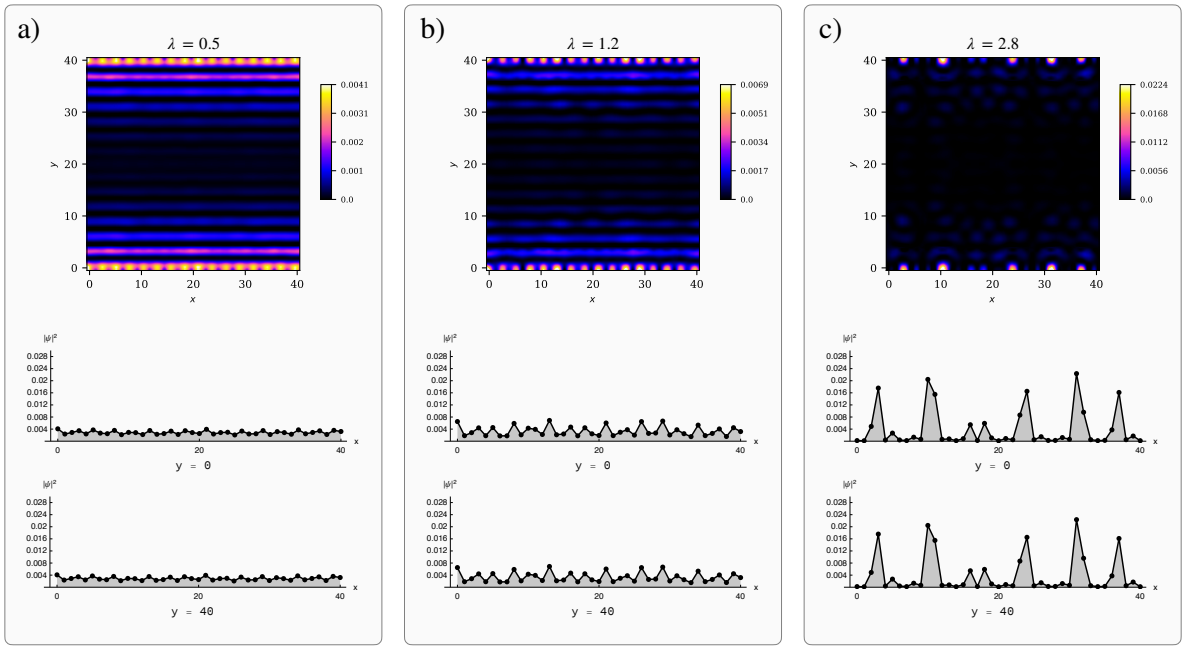

Figure 4.6: Disordered edge states for $t = 1$, $d = t/6$, $\mu = -3.5$, $B_y = 4d$, $\alpha = 0.2d$ and $\Delta_s = 0.3d$ subject to Aubry-André edge disorder. The wavefunctions have energies a) $E = 2.8 \times 10^{-3}$, b) $E = 1.7 \times 10^{-3}$, c) $E = 9 \times 10^{-4}$.

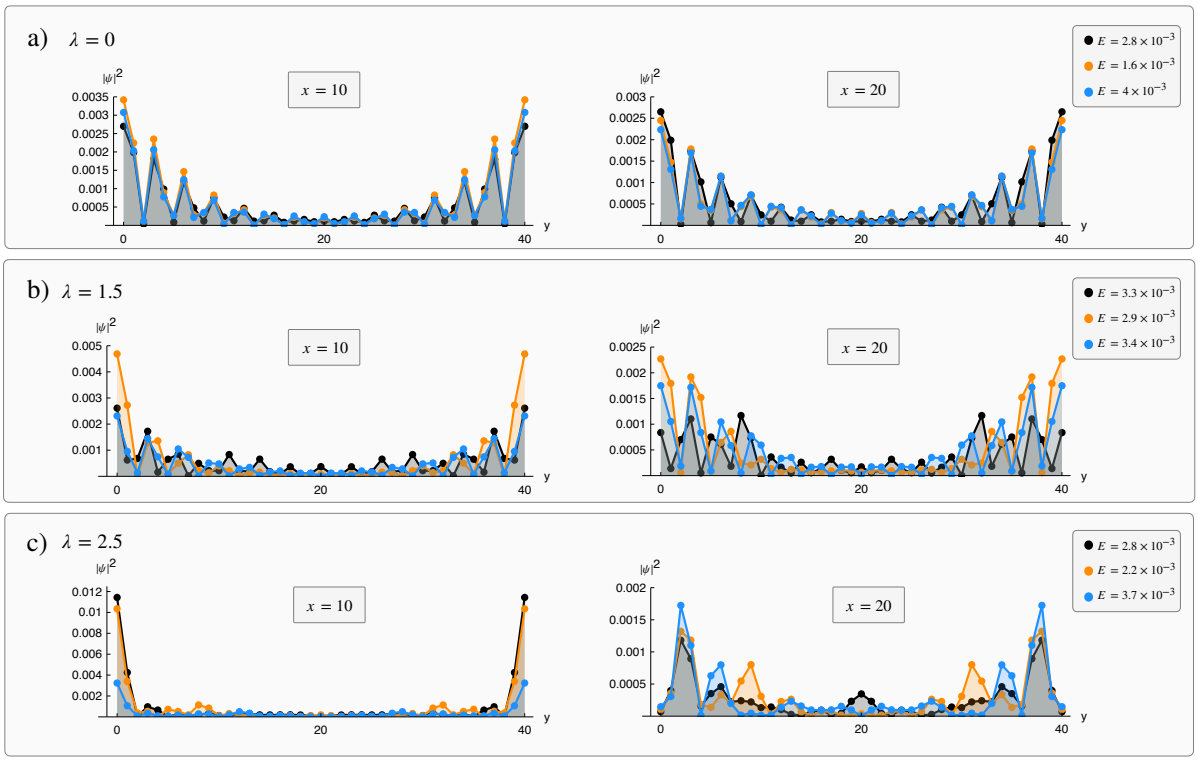

Figure 4.7: Disordered edge states for $t = 1$, $d = t/6$, $\mu = -3.5$, $B_y = 4d$, $\alpha = 0.2d$ and $\Delta_s = 0.3d$, subject to Aubry-André edge disorder. Here the states are shown at fixed values of x, perpendicularly to the direction of the edges, showing the impact of edge disorder on the bulk layers.

In figure 4.5 we show the averaged values of the IPR as before, for a) lower energy states and b) remaining states. Once again, the IPR of the bulk states remains nearly constant, in contrast with the lower energy states. However, the behaviour is different from the case where Anderson disorder was introduced at the edges. Here, the lowest energy states seem mostly unaffected (with constant IPR) until a certain threshold value of disorder. This threshold effect is more prominent in the case with $B_y = 0.5d$. In the two remaining cases the edge states begin to localize at lower values of disorder strength, but are more robust at higher values.

Figure 4.6 shows three wavefunctions which represent low-energy edge states at three different values of disorder, a) $\lambda = 0.5$, b) $\lambda = 1.2$, and c) $\lambda = 2.8$. These states are shown for the noncentrosymmetric case, with $t = 1$, $d = t/6$, $\mu = -3.5$, $B_y = 4d$, $\alpha = 0.2d$ and $\Delta_s = 0.3d$. In the numerical simulations the same value of ϕ was considered at both edges, and, accordingly, the behaviour is mirrored, with the edge states staying localized at both edges for high disorder values. For $\lambda = 0.5$ the state as a whole is mostly unaffected, and the effect of the quasi-periodic disorder is seen on the edge layers. In b), for a higher value of disorder of $\lambda = 1.2$ the state becomes more localized, both along the edges and along the y direction. In c) for $\lambda = 2.8$ the state localizes at several values of x along the edges, and also appears to localize along y. An effect on the bulk layers is also seen, and figure 4.7 allows us to look into it with more detail. As in the Anderson edge disorder case, we show the evolution of edge states with disorder for the same noncentrosymmetric case, taking fixed values of x and for a) $\lambda = 0$, b) $\lambda = 1.5$, c) $\lambda = 2.5$. The wavefunctions at $\lambda = 0$ are the same as those considered in figure 4.4. In b), for $\lambda = 1.5$ and at $x = 10$, the states become more localized towards the edges. For the wavefunction at $E = 3.3 \times 10^{-3}$, at $x = 20$, there is a slight increase of the wavefunction on the bulk layers near the edge. In c), we see that the wavefunctions localize at the edges for $x = 10$. At $x = 20$ we see that, while at the edges and the immediately following layers the value of the wavefunctions is nearly zero, there is a significant contribution on the subsequent bulk layers.

4.1.2 Bulk disorder

We now consider cases were disorder is introduced in the whole system, that is, when the disorder term is present in every site. A system with $41 \times 41 = 1681$ sites (with $N_x = N_y$) is studied. Three types of disorder are considered:

- Type III: Anderson disorder, such as in equation 4.3;
- Type IV: Anderson disorder, such as in equation 4.3 but where the potential varies randomly only in the y direction and is uniform in the x direction;
- Type V: Aubry-André disorder such as in equation 4.4 but where the potential is modulated only in the y direction and is uniform in the x direction, such that

$$\Lambda(x, y) = \lambda \cos(2\pi\alpha y + \phi). \tag{4.8}$$

Anderson bulk disorder

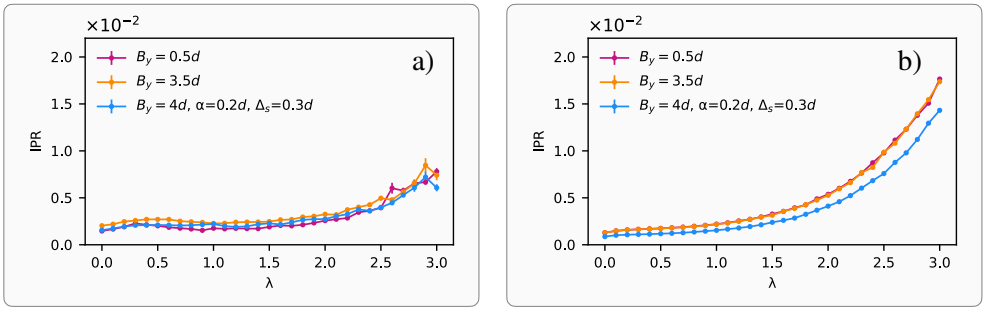

Figure 4.8: a) IPR averaged over the lowest 10 positive energy states and highest 10 negative energy states, vs. Anderson disorder strength λ (Type III). b) IPR averaged over the remaining states vs. disorder strength λ. The results are averaged over 10 disorder configurations.

Figure 4.8 shows the IPR for a) lower energy states and b) remaining states, as a function of Anderson disorder strength λ on all space (Type III). From figure b) we see that the average IPR follows a nearly exponential behaviour as a function of disorder, $\mathcal{IPR} \sim \exp\{\lambda\}$. Comparing figures a) and b) we see that the lowest energy states appear to be more robust if compared with the average response of the system. However, it is necessary to look at the wavefunctions to have a better insight of the disorder effects on the lowest energy states. Figure 4.9 shows three wavefunctions which represent low-energy states at three different values of disorder, a) $\lambda = 0.9$, b) $\lambda = 1.5$, and c) $\lambda = 2.5$. These concern the noncentrosymmetric case, with $t = 1$, $d = t/6$, $\mu = -3.5$, $B_y = 4d$, $\alpha = 0.2d$ and $\Delta_s = 0.3d$.

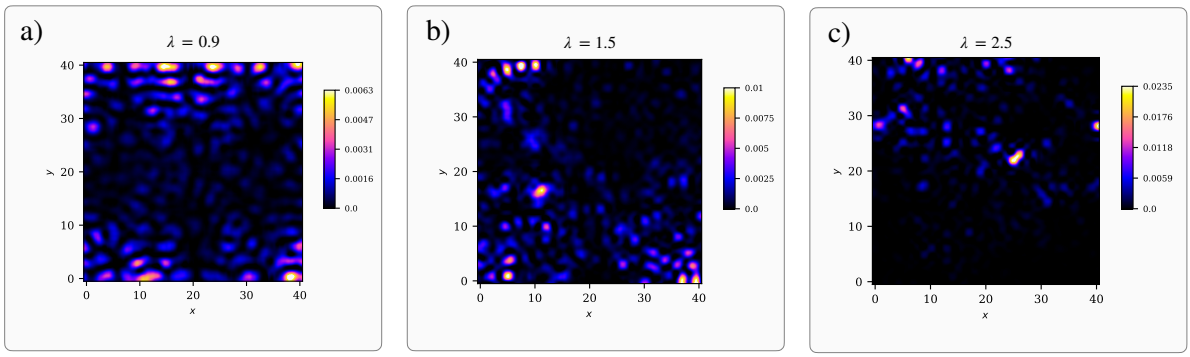

Figure 4.9: Disordered states for $t = 1$, $d = t/6$, $\mu = -3.5$, $B_y = 4d$, $\alpha = 0.2d$ and $\Delta_s = 0.3d$ subject to Anderson disorder (Type III). The wavefunctions have energies a) $E = 2.86 \times 10^{-4}$, b) $E = 4.1 \times 10^{-5}$ and c) $E = 2.91 \times 10^{-3}$.

The figure shows low energy states which become increasingly more localized inside the bulk. From inspection of the wavefunctions we see that the edge states quickly lose their structure for low values of disorder. However, the effect is mostly that of spreading the states towards the bulk. In this case the IPR is not a good measure of the survival of the edge states because they do not become quickly localized, but they are destroyed in the sense that they are removed from the edges. At $\lambda = 2.5$ the state in figure c) is mostly localized around a site but still has some contributions throughout the bulk.

Figure 4.10 shows the total density of states of the system obtained with the RGF method, for $\lambda = 0$ (no disorder), $\lambda = 0.5$, $\lambda = 1.5$ and $\lambda = 2.5$. We see that in all cases there is a large increase of the density of states around zero energy, with a monotonic behaviour. This increase makes the considered fixed interval of eigenstates around zero energy more susceptible to level crossings with the bulk, and in this case the evaluation of figure 4.8 a) must be taken with care.

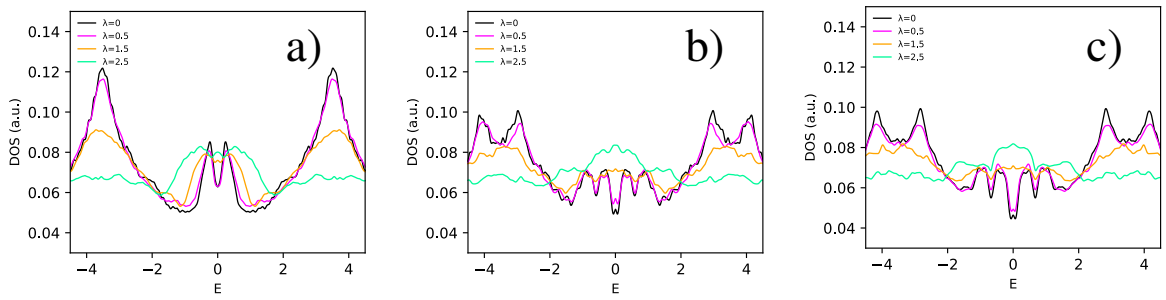

Figure 4.10: Total density of states, for the energy range $E \in [-4.5, 4.5]$ obtained with the Recursive Green's Function method for several values of Anderson disorder strength λ (Type III). The values of the parameters are a) $B_y = 0.5d$, b) $B_y = 3.5d$, c) $B_y = 4d, \alpha = 0.2d, \Delta_s = 0.3d$. The DOS is obtained for an average of 20 initial random states and disorder configurations, and for a value of $\eta = 0.08$ (equation B.11).

Anderson bulk disorder with x periodicity

We now considered a uniform modulation of Anderson disorder in the x direction, that is, we introduce a disordered potential which is random along y but is constant along x (Type IV disorder). This example serves as an intermediate between the previous case in which random disorder was introduced in all space, and the next case in which disorder is quasi-periodic along y and constant along x. Introducing periodicity along x also allows us to make a connection to the analogous system in a mixed reciprocal space (k_x, y) which will be the focus of the second part of the work.

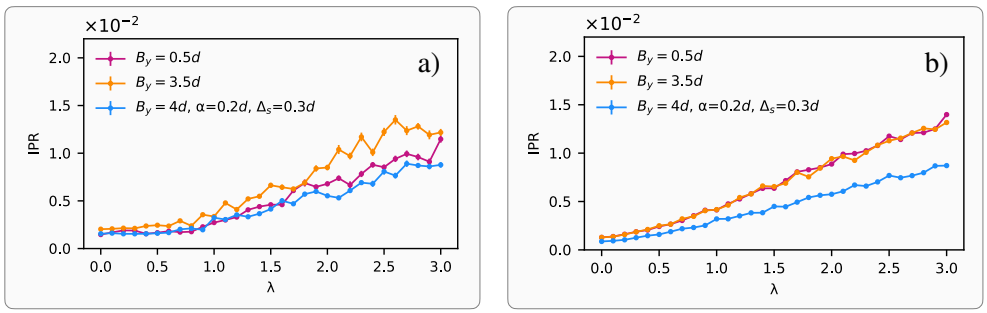

Figure 4.11: a) IPR averaged over the lowest 10 positive energy states and highest 10 negative energy states, vs. Anderson disorder strength λ (Type IV). b) IPR averaged over the remaining states vs. disorder strength λ. The results are averaged over 10 disorder configurations.

Figures 4.11 a) and b) show the IPR of the lowest energy states and of the remaining states, respectively. Contrarily to the previous case, there is no significant difference between the localization

behaviour of the lowest energy states and the bulk-averaged IPR. From b) we see that the average IPR follows a nearly linear behaviour as a function of disorder, as $\mathcal{IPR} \sim \lambda$. This contrasts with the nearly exponential behaviour found previously. In figure 4.12 we show a comparison of the IPR averaged over the whole system for a) Anderson disorder (Type III) and b) Anderson disorder with x periodicity (Type IV), as well as fits to functions of the form a) $y = C_1 \exp\{C_2 x\}$ and b) $y = C_1 x + C_2$.

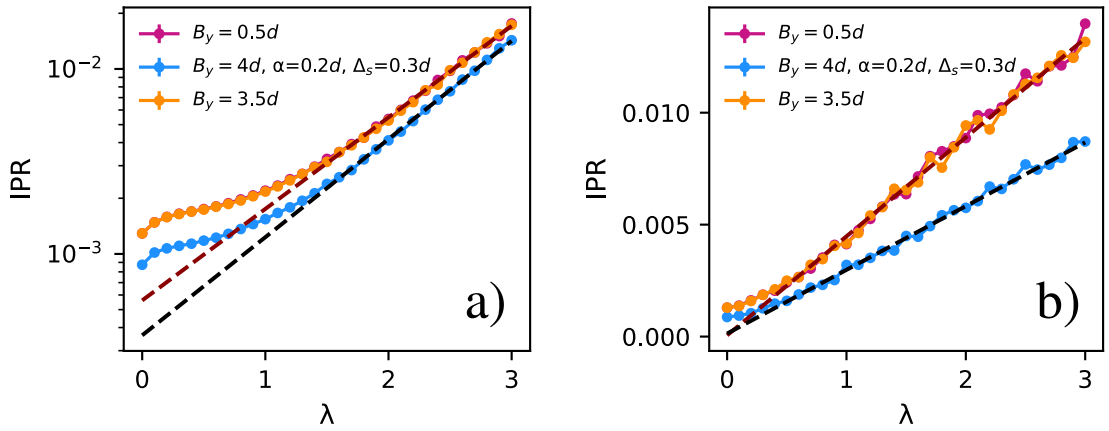

Figure 4.12: a) Average IPR of the whole system for Anderson disorder and fits of functions of the form $y = C_1 \exp\{C_2 x\}$ in the range $\lambda \in [1.5, 3]$. b) Average IPR of the whole system for Anderson disorder with x periodicity and fits of functions of the form $y = C_1 x + C_2$ in the range $\lambda \in [0.5, 3]$.

In a) the fit is done to the range $\lambda \in [1.5, 3]$ and gives the values $(C_1, C_2) = (5.6 \times 10^{-4}, 1.13)$ for $B_y = 0.5d$ and $B_y = 3.5d$, and $(C_1, C_2) = (3.6 \times 10^{-4}, 1.22)$ for $B_y = 4d$, $\alpha = 0.2d$, $\Delta_s = 0.5d$. For $\lambda > 1.5$ the IPR follows an exponential behaviour closely, while for $\lambda < 1.5$ there is a deviation from it. Noticeably, the cases with different values of B_y are superimposed, while the noncentrosymmetric case with spin-orbit coupling and added s-wave pairing has a consistently lower IPR, both in the clean system and as disorder is increased. This behaviour is observed in any considered disorder case, and suggests that the average localization properties of the system are independent of the value of the applied magnetic field, but depend on the values of α and Δ_s. In b), the fit is done to the range $\lambda \in [0.5, 3]$ and gives the values $(C_1, C_2) = (4.4 \times 10^{-3}, 5 \times 10^{-5})$ for $B_y = 0.5d$ and $B_y = 3.5d$[1] and $(C_1, C_2) = (2.8 \times 10^{-3}, 1.4 \times 10^{-4})$ for the noncentrosymmetric case. For $\lambda < 0.5$ there is a deviation from the linear behaviour.

[1] As the cases of $B_y = 0.5d$ and $B_y = 3.5d$ have essentially the same behavior apart from small fluctuations the fits were done to the average of the IPR values.

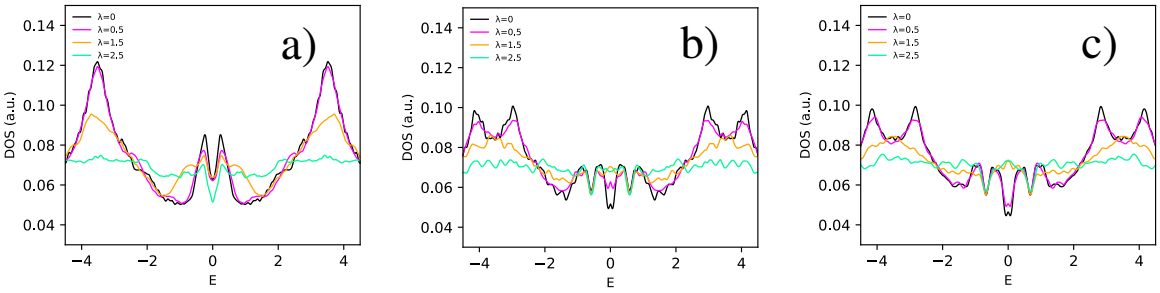

Figure 4.13: Total density of states of the system, for the energy range $E \in [-4.5, 4.5]$ obtained with the Recursive Green's Function method for several values of Anderson disorder strength λ (Type IV). The values of the parameters are a) $B_y = 0.5d$, b) $B_y = 3.5d$, c) $B_y = 4d, \alpha = 0.2d, \Delta_s = 0.3d$. The DOS is obtained for an average of 20 initial random states and disorder configurations, and for a value of $\eta = 0.08$ (equation B.11).

In figure 4.13 the density of states obtained with the RGF method is shown for the three cases of the parameter values considered for the clean system ($\lambda = 0$) and for the disorder values $\lambda = 0.5$, $\lambda = 1.5$ and $\lambda = 2.5$. The behaviour differs from that seen on the true Anderson disorder case in 4.10. The behaviour in a) also differs from that in b) and c). In the latter the DOS around zero energy shows an increase for higher values of disorder while for the first case it decreases, in relation to the clean case.

Let us now look at the system's wavefunctions. In figure 4.14 we show low enegy states for the values of $t = 1$, $d = t/6$, $\mu = -3.5$ and $B_y = 3.5d$ (MFBs regime). The edge states are mostly robust to low values of disorder, as seen in figure a) for $\lambda = 0.4$. In this case a state which was previously symmetric around both edges becomes more localized near the edge in $y = 0$. As λ increases slightly we find that the states are removed from the edges and start to localize inside the bulk. This happens around $\lambda \approx 0.6$. These then become increasingly more localized along y, as we see in b) for $\lambda = 1.6$. For high values of disorder, as in c) for $\lambda = 2.5$, some states become almost completely localized along y, while staying periodic along x. Note that, as disorder removes states from the edges, there is no opening of the bulk gap.

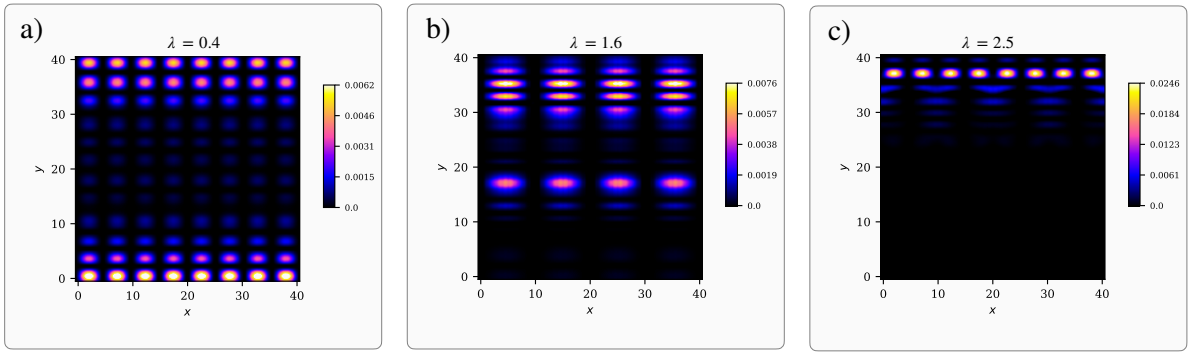

Figure 4.14: Disordered states for $t = 1$, $d = t/6$, $\mu = -3.5$ and $B_y = 3.5d$, subject to Anderson disorder with $x-$periodicity (Type IV). The wavefunctions have energies a) $E = 3.07 \times 10^{-3}$, b) $E = 4.79 \times 10^{-3}$ and c) $E = 2.61 \times 10^{-3}$.

Aubry-André bulk disorder

We now consider Aubry-André bulk disorder (Type V disorder). We consider a modulation along y and a potential which is uniform along x. Figures 4.15 a) and b) show respectively the IPR of the lowest energy states and of the remaining states. We see no significant differences in behaviour between a) and b). As in the case of Aubry-André edge disorder, we see again a threshold behaviour, but here on the whole system: there is a clear change around $\lambda \approx 2$ in b), with a sharp increase in the IPR.

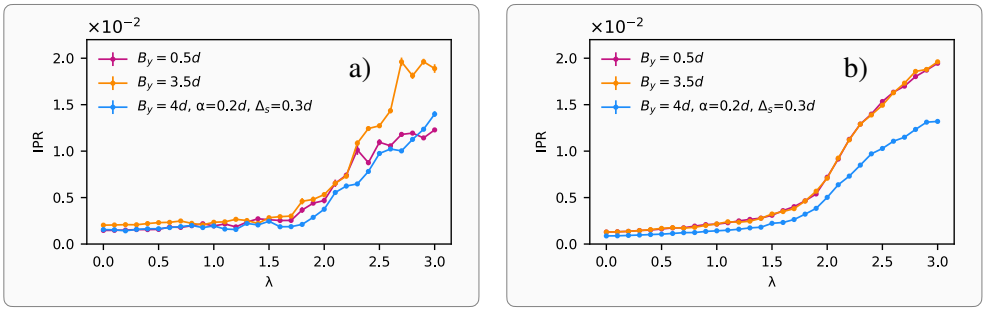

Figure 4.15: a) IPR averaged over the first 10 positive energy states and last 10 negative energy states, vs. quasi-disorder strength λ (Type V). b) IPR averaged over the remaining states vs. quasi-disorder strength λ. The results are averaged over 10 disorder configurations.

The behaviour found for the IPR in figure b) resembles some known results. For the one-dimensional Aubry-André model, the system undergoes an extended-localized transition at $\lambda = 2t$, after which the average IPR shows a marked increase. For the one dimensional p-wave superconductor with an Aubry-André potential the transition point changes to $\lambda = 2(t+d)$ (when the chemical potential is taken as zero), where d is the pairing amplitude, and the average IPR also follows a similar behaviour [43]. However, for a finite value of the chemical potential, the sudden increase in the IPR is found for $\lambda < 2(t+d)$ [44]. In this sense, our result seems to agree: the $p-$wave pairing potential is taken as $d = t/6$ and we see a transition for $\lambda < 2(t+d) = 7t/3 \approx 2.33$. A similar behaviour is also found for a two dimensional model of a square lattice (without superconductivity) [19] with a quasi-periodic potential modulated both in the x and y directions. In figure 4.15 b), we see a slow increase of the IPR before $\lambda \approx 2$. This differs from the aforementioned examples, where this increase is not as clearly seen. This could be due to the appearance of critical wave functions in this range which contribute to an increase of the average IPR. Before the large increase of the IPR, some of the bulk wavefunctions do appear to have a critical nature (in the y direction, staying periodic in the x direction).

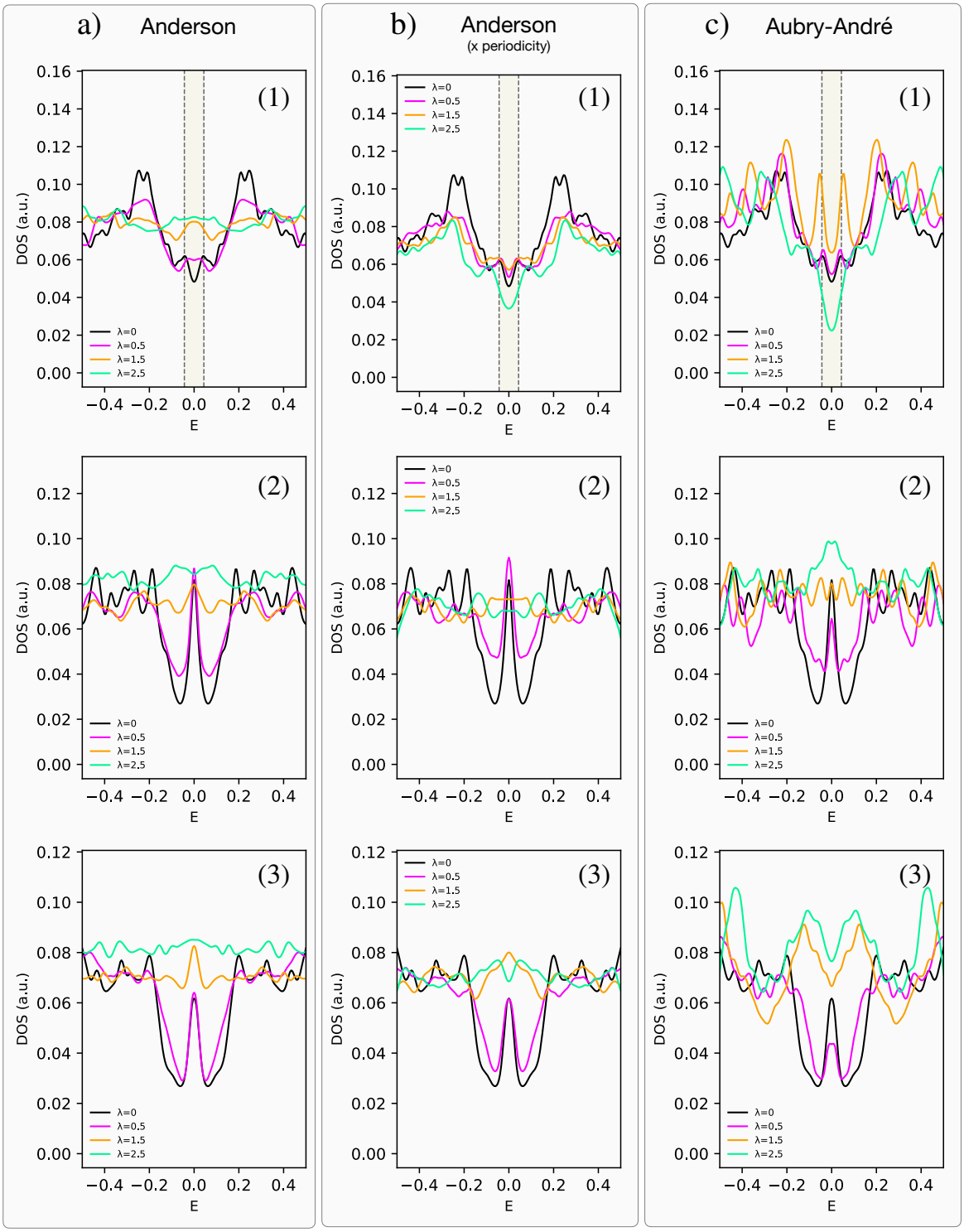

Figure 4.16: Total density of states of the system, for the energy range $E \in [-0.5, 0.5]$, obtained with the Recursive Green's Function method for several values of λ. Each column concerns the case of a) Anderson disorder (Type III), b) Anderson disorder with x periodicity (Type IV) and c) Aubry-André disorder (Type V), and each row concerns the parameter values (1) $B_y = 0.5d$, (2) $B_y = 3.5d$, (3) $B_y = 4d, \alpha = 0.2d, \Delta_s = 0.3d$. The DOS is obtained for an average of 20 initial random states and disorder configurations, and for a value of $\eta = 0.02$ (equation B.11).

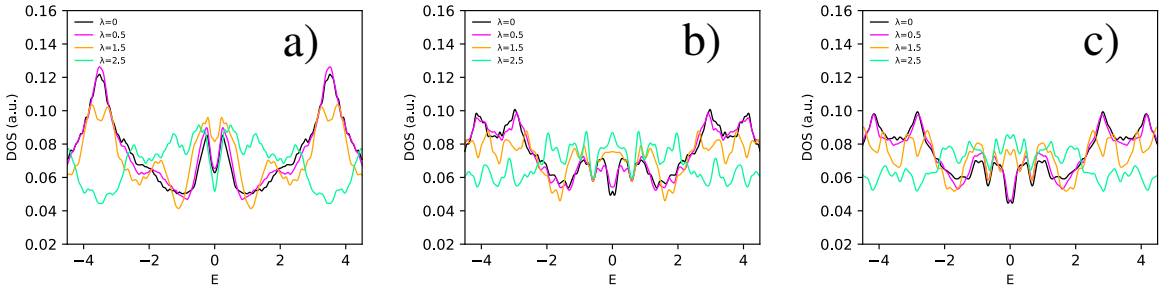

Figure 4.17: Total density of states of the system, for the energy range $E \in [-4.5, 4.5]$ obtained with the Recursive Green's Function method for several values of Aubry-André disorder strength λ (Type V). The values of the parameters are a) $B_y = 0.5d$, b) $B_y = 3.5d$, c) $B_y = 4d, \alpha = 0.2d, \Delta_s = 0.3d$. The DOS is obtained for an average of 20 initial random states and disorder configurations, and for a value of $\eta = 0.08$ (equation B.11).

In figure 4.16 a close-up of the region closer to zero energy $E \in [-0.5, 0.5]$ is presented, for a lower value of η, and for all the considered disorder cases side-by-side to allow a clear comparison. Each column concerns each bulk disorder type - a) Anderson disorder, b) Anderson disorder with x periodicity, c) Aubry-André disorder, and each column concerns each parameter set - (1) $B_y = 0.5d$, (2) $B_y = 3.5d$, and (3) $B_y = 4d, \alpha = 0.2d, \Delta_s = 0.3d$. For (1) the bulk gap of the clean system, which is located around $E \in [-0.044, 0.044]$, is highlighted. In this case, with quasi-disorder, we see first that the DOS increases slightly at $\lambda = 0.5$ around zero energy. For $\lambda = 1.5$ there is a further increase and for $\lambda = 2.5$ the value decreases, with the system being actually gapped. This is not seen in figure 4.16 because of the high value of η considered. In cases (1) and (2) for quasi-disorder we see the same non monotonic behaviour in which the DOS around zero energy first decreases and then increases with disorder.

Figure 4.17 shows the density of states for the energy range $E \in [-4.5, 4.5]$, for $\lambda = 0$ (clean system), $\lambda = 0.5$, $\lambda = 1.5$ and $\lambda = 2.5$.

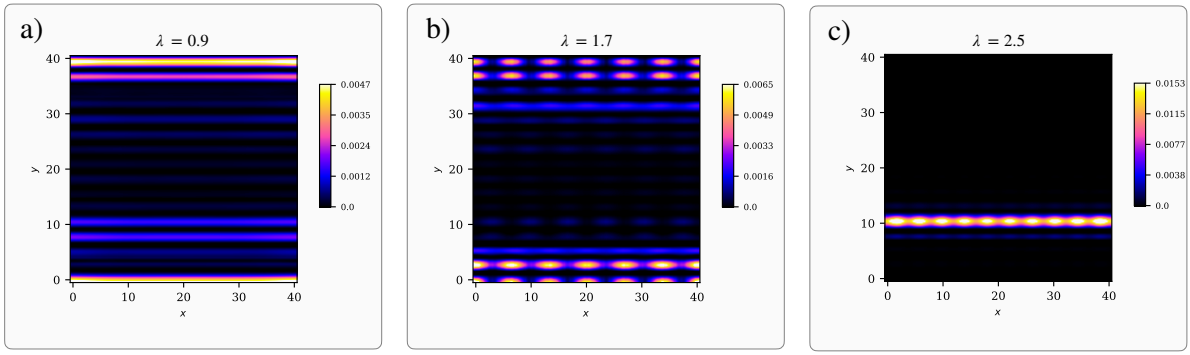

Figure 4.18: Disordered states for $t = 1$, $d = t/6$, $\mu = -3.5$ and $B_y = 0.5d$, subject to Aubry-André disorder (Type V). The wavefunctions have energies a) $E = 5.44 \times 10^{-3}$, b) $E = 1.34 \times 10^{-3}$ and c) $E = 3.23 \times 10^{-2}$.

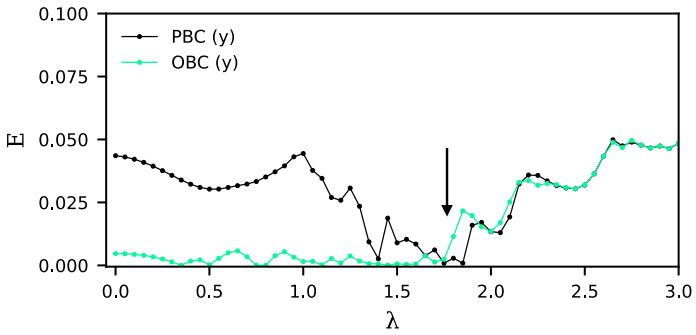

Figure 4.19: First positive energy state for a system of size 41×41 vs. disorder strength of the quasi-periodic potential with $\phi = 0$, for the system with open boundary conditions along y (green) and periodic conditions along y (black). The values of the parameters are $t = 1$, $d = t/6$, $\mu = -3.5$ and $B_y = 0.5d$.

In figure 4.18 we show some of the low energy states at different values of λ, for the parameters $t = 1$, $d = t/6$, $\mu = -3.5$ and $B_y = 0.5d$. In the clean system this corresponds to the case with a gapped bulk but gapless edge states. In agreement with the results obtained for the IPR, the edge states appear to be robust to low values of disorder. In 4.18 a), for $\lambda = 0.9$, the state is not removed from the edge, although we see some critical-like behaviour on the bulk. In b), for $\lambda = 1.7$ there is a deviation from the edges and instead of localizing at the edges the states localize in the subsequent layers, however the states are not completely removed from the edges. In c), for $\lambda = 2.5$ the states become nearly completely localized along y and there are no edge states on the system. As stated previously, we know that for higher values of disorder a bulk gap opens, so we no longer expect edge states at such values.

By looking at the energy spectrum of the system with OBC and PBC along y, we can understand where disorder destroys the edge states in this case. Figure 4.19 shows the lowest positive energy state for the system with periodic boundary conditions in y (black) and periodic boundary conditions in y (green). Around $\lambda \approx 1.8$ the energy of the lowest state in the OBC system is lifted and becomes higher than that of the system with PBC. This signals the opening of the bulk gap around this disorder value. For higher values of disorder the edge states are no longer present in the system, which can be seen from the fact that the energy lowest positive energy state of the OBC becomes nearly identical to that of the system of PBC (the first positive state coincides with the first positive bulk state). This effect (opening of a gap as disorder is increased) is not seen for the other considered parameter values, a magnetic field of $B_y = 3.5d$ or a magnetic field of $B_y = 4d$, Rashba spin orbit coupling $\alpha = 0.2d$ and s-wave pairing $\Delta_s = 0.3d$. In this case the lower energy states are not lifted to higher energies. This does not mean that the edge states remain robust to the perturbations, but only that there is no opening of the bulk gap (remembering these last two cases are gapless phases in the clean system).

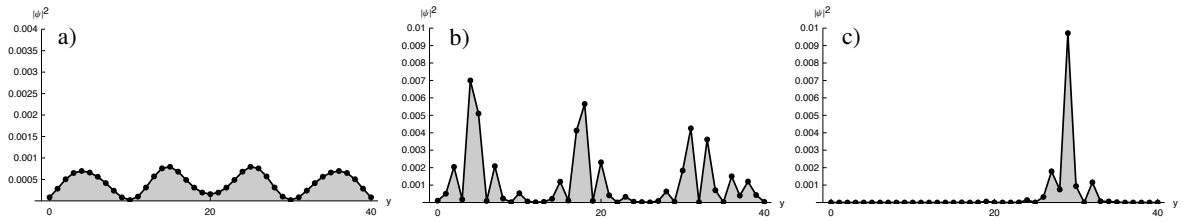

Figure 4.20: Example of wavefunctions with Aubry-André disorder (Type V), at a fixed value $x = 8$, for the system of size 41×41. a) Extended wavefunction at $E = 0.28$, $\lambda = 0$, b) critical wavefunction at $E = 0.51$, $\lambda = 1.6$, c) localized wavefunction at $E = 0.32$, $\lambda = 2.5$.

In figure 4.20 we show bulk states at different values of λ and for a fixed value of $x = 8$: an extended state in a), a critical state in b) and a localized state in c). For some values of λ the states show a critical-like behaviour, as is shown for $\lambda = 1.6$. Note that the critical or localized behaviour is only seen along y, the direction in which the disorder potential is modulated. Along x the states remain periodic (extended) as in 4.18.

4.1.3 Quasi-disorder induced topology: Chern number

We now want to investigate the effects of quasi-disorder on the system with an applied magnetic field in the perpendicular direction, $\mathbf{B} = (0, 0, B_z)$. We consider Anderson and Aubry-André disorder modulated along y and uniform in x, corresponding to disorder of Types IV and V as discussed in Section 4.1.2. To classify the topological nature of the system the Chern number is calculated in real space. The numerical method is detailed in Appendix B.

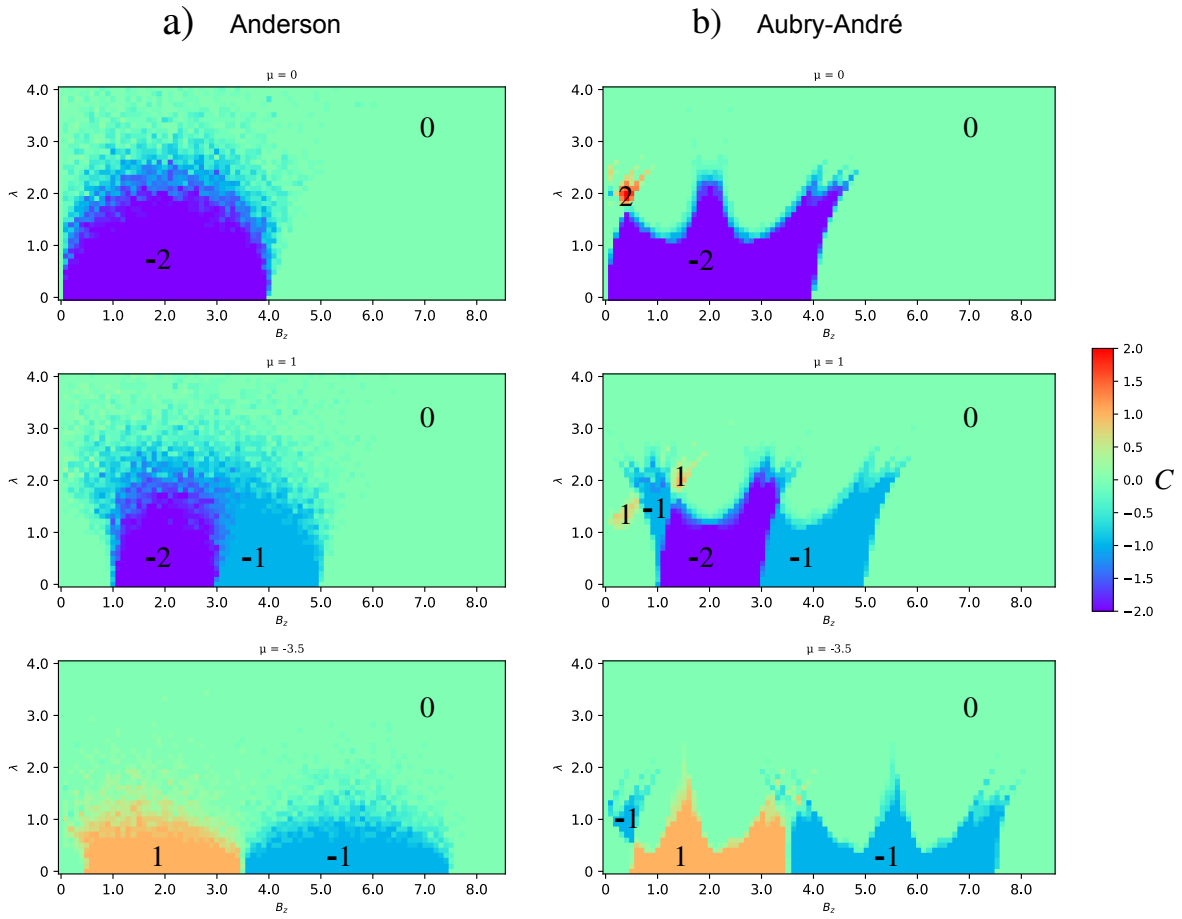

Figure 4.21: Phase diagrams of a system with 20x20 sites, indexed by the Chern number C, for several values of disorder strength λ and perpendicular magnetic field B_z. Obtained for the average over 10 disorder configurations. The values of the parameters are $t = 1$, $d = 0.6$ and $\mu = 0$ (top), $d = 0.6$ and $\mu = 1$ (middle), $d = 1/6$ and $\mu = 3d - 4t = -3.5$ (bottom).

Figure 4.21 shows six phase diagrams for three different values of μ and d (in all cases, t is kept constant and equal to 1) obtained for a system with size 20×20, for a) Anderson disorder and b) Aubry-André disorder, both uniform in the x direction. At $\lambda = 0$, we observe the transitions between different Chern numbers consistent with figure 3.2 at the respective values of μ.

When Anderson disorder is introduced in the system the topological regimes are destroyed as the disorder strength is increased. From the phase diagrams we see that some values of B_z are more robust than others, particularly the values which are halfway inside the topological phases of the clean

system, while the values near the phase boundaries are more vulnerable to the introduced disorder. Unexpectedly, at low values of magnetic field, we see some small traces of topology appear as disorder is increased for values of B_z where the Chern number was previously zero.

Let us now turn to the right panels of the figure, where quasi-periodic disorder is introduced. We obtain phase diagrams with new topological regions. Different types of transitions are illustrated. In the diagram for $\mu = 0$ and $d = 0.6$ (top) we see the appearance of a phase characterized by $C = 2$ around $B_z \in [0.2, 0.5]$. Noticeably, in the clean system no phase with $C = 2$ exists. For $\mu = 1$ and $d = 0.6$ (middle), we see the appearance of two small regions with $C = 1$, that however seem to be averaged out. In the approximate range of $B_z \in [0.3, 1.3]$ there is also a reentrant topological region with $C = -1$. Inside this range, for $B_z < 1$, we have topological transitions $C = 0 \to C = -1$ with increasing λ. For $B_z \in [1, 1.3]$, there is a transition $C = -2 \to C = -1$. At $\mu = -3.5$, $d = 1/6$ (bottom) a new region with $C = -1$ emerges for $B_z \in [0.1, 0.9]$. Inside this range, for $B_z < 0.5$ a transition $C = 0 \to C = -1$ happens with increasing λ. For $B_z \geq 0.5$ there is a previous transition from $C = 1$ to $C = 0$. A close-up of the region with $C = -1$ is presented in figure 4.22 for a system of size 40×40. Transitions from $C = 0$ to a finite value of C also happen at higher values of the magnetic field. This is evident in the case of $\mu = 0$ for $B_z > 4$ and in the case $\mu = 1$ for $B_z > 5$. For a small region of B_z, with the increase of λ we see a reentrant topological phase in a new region.

Furthermore, the topological phases show an interesting response to the increase of quasi-disorder. There is a clear difference in robustness for different values of B_z as quasi-disorder is increased, which originates the seemingly effect of “peaks” and “valleys” in the phase diagram, respectively at more robust and more vulnerable values of B_z.

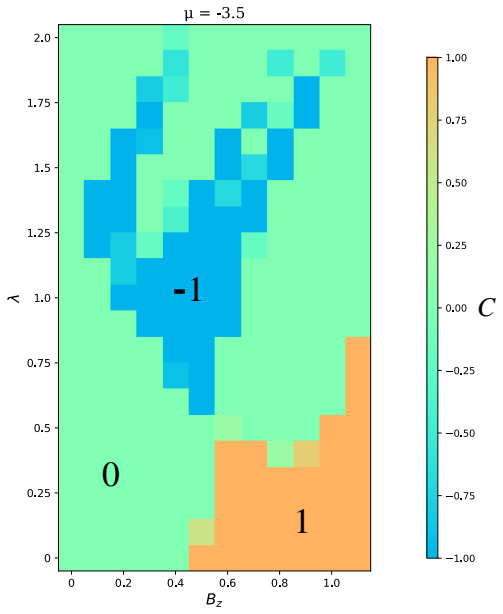

Figure 4.22: Phase diagram of a system with 40x40 sites, indexed by the Chern number C, for several values of disorder strength λ and perpendicular magnetic field B_z. Obtained for the average over 10 disorder configurations. The values of the parameters are $t = 1$, $d = t/6$, $\mu = -3.5$.

It is important to note that here the regimes with low magnetic field and $C = 0$ correspond to regimes with $I(k_y) \neq 0$ before disorder is introduced (as λ assumes a finite value, $I(k_y)$ becomes ill-defined since the translational symmetry in the system is lost). As discussed in section 3.2, in some regions the system has gapless edge states which are explained by a finite value of $I(k_y)$ although the Chern number is zero. This means that the reentrant topological phases with $C \neq 0$ at low magnetic field come from phases that were nontrivial at $\lambda = 0$ due to $I(k_y)$ (except in the case of $\mu = 0$). This could possibly explain some of the topological transitions at small values of B_z as quasi-disorder is introduced, and also the appearance of some topological regions at roughly the same values of B_z in the Anderson case (as it can be observed in the diagrams for $\mu = 1$ and $\mu = -3.5$). On the other hand, we note that the Anderson disorder considered in 4.21 has periodicity in x, as in the considered case of the Aubry-André potential. Thus it could be the case that the appearance of small regions of topology at low magnetic field in the Anderson case, similarly to the Aubry-André case, are a result of this added modulation in x, instead of being related to the invariant $I(k_y)$. Also, when quasi-disorder is introduced in the system, transitions $C = 0 \rightarrow C \neq 0$ are also observed for values of high magnetic field in regions where $I(k_y)$ is zero in the clean case. This behaviour can not be justified by the value of $I(k_y)$, which is zero at high values of B_z before disorder is introduced. This type of transition is also not observed with Anderson disorder with x periodicity.

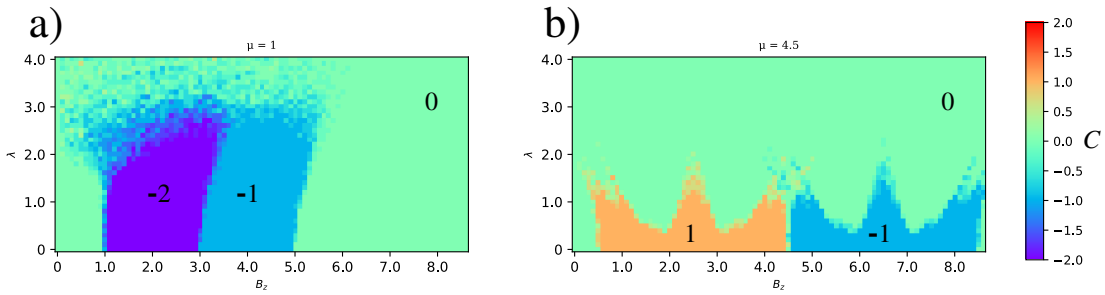

Figure 4.23: Phase diagrams of a system with 20x20 sites, indexed by the Chern number C, for a) Anderson disorder (without x periodicity) with $t = 1$, $d = 0.6$, $\mu = 1$ and b) Aubry-André disorder with $t = 1$, $d = t/6$, $\mu = 4.5$.

To further understand the influence of introducing x periodicity in the Anderson potential and of the finite value of $I(k_y)$ we considered the cases in figure 4.23. Figure 4.23 a) shows the diagram for the parameter values $t = 1$, $d = 0.6$ and $\mu = 1$ with Anderson disorder with no added periodicity. We see that a weak topological region at low magnetic fields also appears, in the regime in which previously $I(k_y) \neq 0$, showing that this effect is independent of the modulation of the disorder potential. Unexpectedly, comparing figure 4.23 a) and the middle panel of figure 4.22 a), we see that the topological phases are more robust to Anderson disorder that is completely random on all space if compared with Anderson disorder with introduced x periodicity. In figure 4.23 b) Aubry-André disorder is introduced in the system with parameters $t = 1$, $d = 1/6$, $\mu = 4.5$. In this case, the regimes at low magnetic field have both a Chern number and a value of $I(k_y)$ of zero in the clean system. Contrary to what happens for $\mu = -3.5$ (figure 4.21 b), bottom panel), where we see the emergence of a new region with $C = -1$, no new topological region appears.

We now want to see how the different critical values of λ scale with the system size. The transitions at fixed values of B_z and μ are now considered for the quasi-periodic disorder case. The results are presented in figure 4.24 for the system sizes 20×20, 30×30 and 41×41 and for $\mu = 0$, $d = 0.6$, $B_z = 0.4$ (left), $\mu = 1$, $d = 0.6$, $B_z = 1.1$ (middle) and $\mu = -3.5$, $d = 1/6$, $B_z = 0.3$ (right). In all cases, $t = 1$. The results show that within the system size range considered the critical values show little variation, and the transitions become more sharp as the size increases. This therefore suggests that the phase diagrams in figure 4.21 obtained for a system size 20×20 should remain valid for larger systems and the phase boundaries should become more defined.

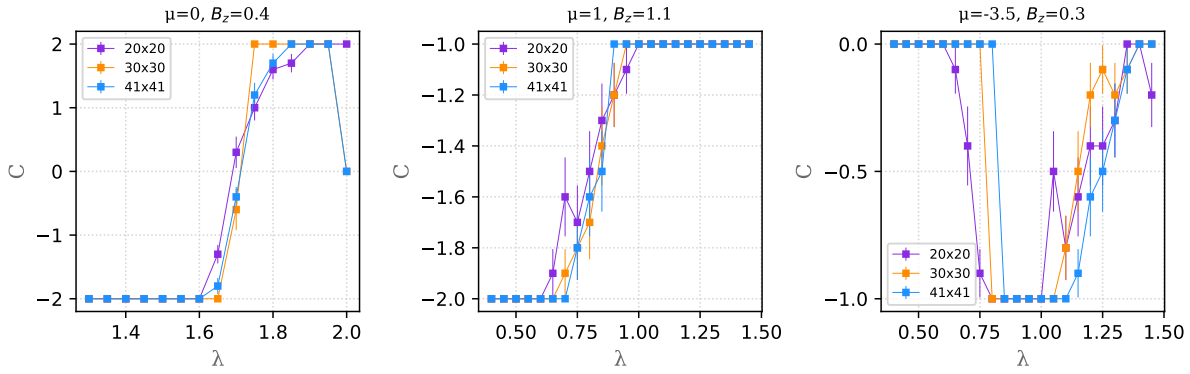

Figure 4.24: Values of the Chern number C vs. quasi-disorder strength λ for the system sizes 20×20, 30×30 and 41×41 and for the parameter values $t = 1$, $\mu = 0$, $d = 0.6$, $B_z = 0.4$ (left), $\mu = 1$, $d = 0.6$, $B_z = 1.1$ (middle) and $\mu = -3.5$, $d = 1/6$, $B_z = 0.3$ (right). The results were averaged over 10 disorder configurations (10 random values of ϕ in the quasi-periodic potential).

It is also of interest to see how the non trivial topology is manifested in the system with open boundary conditions. Figure 4.25 shows two in-gap states for the topological phase at the values $\mu = 1$, $d = 0.6$ and $B_z = 1.1$, for a system of size 41×41 with PBC in x and OBC in y. The states are presented for a value of $\lambda = 1.1$ but are illustrative of the typical states that are found within this phase. The state on the left (1) is a negative in-gap energy state which is localized only on the left edge and is an example of an edge state at finite energy. On the right, the first positive energy state (2) has a value of energy of about 10^{-6}. Taking into account the size of the system considered, it is likely that this represents a zero energy state that should tend to a true value of $E = 0$ as the system size is increased. There are two such states inside the gap, and they remain in the system throughout the phase characterized by $C = -1$, becoming slightly more localized as the disorder strength is increased. Interestingly, we see that this state is not truly localized at the edges, but rather sharply localized close to the edges. Also, the state is localized at both edges simultaneously. This behaviour is consistent throughout the topological phase.

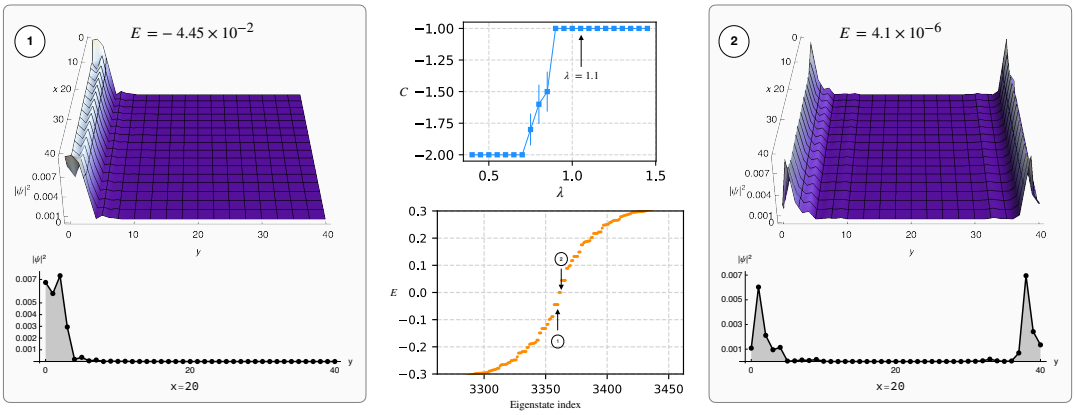

Figure 4.25: In-gap states at the topological phase with $C = -1$ for $\mu = 1$, $d = 0.6$, $B_z = 1.1$, and $\lambda = 1.1, \phi = 0$ in the quasi-periodic Aubry-André potential. The left panel (1) shows a state at $E = -4.45 \times 10^{-2}$ (top) and a one-dimensional cut of the wavefunction at $x = 20$ (bottom). The right panel (2) shows a state at $E = 4.1 \times 10^{-6}$ (top) and a one-dimensional cut of the wavefunction at $x = 20$ (bottom). The middle panel locates the value of λ within the topological phase (top) and locates the states (1) and (2) in the energy spectrum of the system (bottom).

We can now look at the transition from $C = 0$ to $C = -1$ that is depicted in the right panel of figure 4.24. Figure 4.26 shows two in-gap states for the topological phase at the values $\mu = 1$, $d = 0.6$ and $B_z = 1.1$, for a system of size 41×41 with PBC in x and OBC in y. We see that this case differs from the previous one since the in-gap states are poorly localized on the edges and show some oscillations along the bulk. This behaviour is verified throughout the whole topological region. There appears to be a lack of a clear bulk-edge correspondence, in the sense that the topological properties are not as clearly manifested in the edges as would be expected. Nevertheless, there is still some localization, which also appears to be not exactly at the edge layer but at the subsequent ones. It is important to note, however, that the lack of bulk-edge correspondence can be a finite size effect, and that in the thermodynamic limit the contributions of the wavefunctions towards the bulk can become smaller.

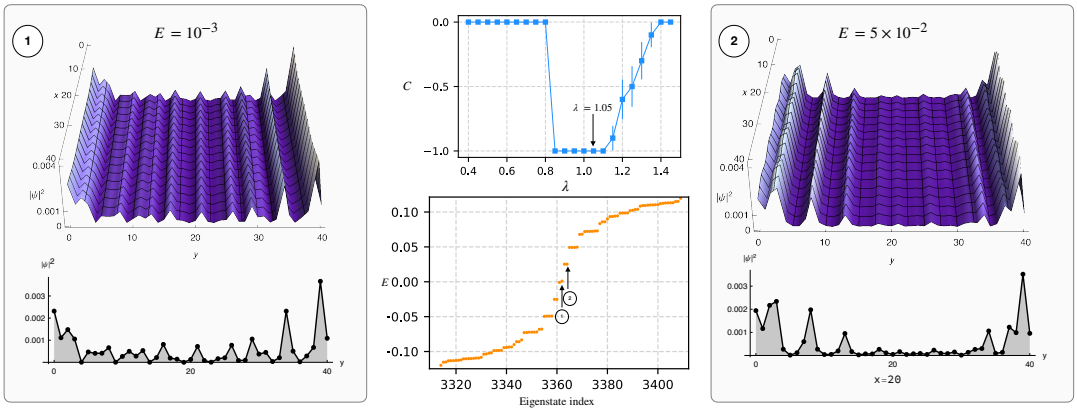

Figure 4.26: In-gap states at the topological phase with $C = -1$ for $\mu = -3.5$, $d = 1/6$, $B_z = 0.3$, and $\lambda = 1.05, \phi = 0$ in the quasi-periodic Aubry-André potential. The left panel (1) shows a state at $E = 10^{-3}$ (top) and a one-dimensional cut of the wavefunction at $x = 20$ (bottom). The right panel (2) shows a state at $E = 5 \times 10^{-2}$ (top) and a one-dimensional cut of the wavefunction at $x = 20$ (bottom). The middle panel locates the value of λ within the topological phase (top) and locates the states (1) and (2) in the energy spectrum of the system (bottom).

We can look at what happens to the edge states as disorder is introduced in a case with finite $I(k_y)$ and Chern equal to zero in the clean system. In figure 4.27 the lowest positive energy state of the system is shown for $\mu = -3.5$, $d = 1/6$, and $B_z = 0.3$ as a function of quasi-disorder strength, λ, for $\phi = 0$ in the quasi-periodic potential. The phases with $C = 0$ are represented in green and the phases with $C = -1$ are represented in blue. The first phase with $C = -1$ is the phase illustrated in figure 4.26 for the value $\lambda = 1.1$. Looking at the system's energy spectrum, we see that for low values of disorder there is no gap opening, and the low energy edge states remain in the system. As disorder is introduced, $I(k_y)$ loses its meaning due to the broken translational invariance of the system, so in this sense the states are no longer expected to be topologically protected. However, it is also possible that a real-space calculation of $I(k_y)$ (as with twisted boundary conditions) could show that the invariant remains quantized, protecting the edge states as disorder is increased.

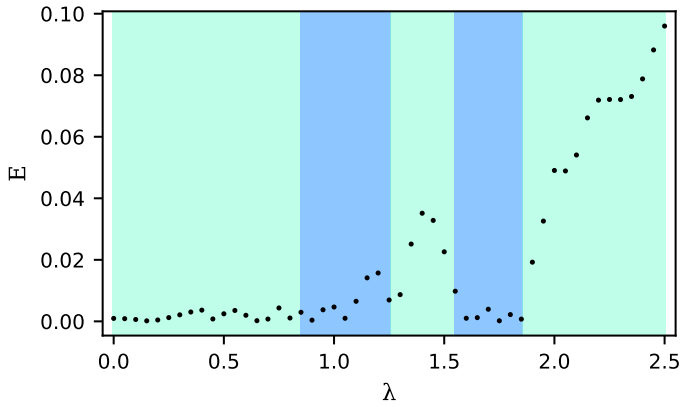

Figure 4.27: First positive energy state for a system of size 41×41 vs. disorder strength of the quasi-periodic potential, for the case $\phi = 0$, and for the parameters $\mu = -3.5$, $d = 1/6$, and $B_z = 0.3$ The phases with $C = 0$ are represented in green, and the phases with $C = -1$ are represented in blue.

4.2 Quasi-disorder and Anderson disorder effects in mixed space

We now want to study disorder in a mixed space (k_x, y) such that the Hamiltonian is written as in equation 3.7 and modified according to equations 4.5 and 4.6. Disorder of Type IV (Anderson disorder) and Type V (Aubry-André quasi-periodic potential) are considered. In both cases the disorder term depends on y and is the same for all k_x. The numerical study of the system now involves the diagonalization of a matrix of size $(4 \times N_y) \times (4 \times N_y)$ for each value of k_x and for each disorder configuration.

4.2.1 Energy spectra evolution and density of states

Anderson disorder

In figure 4.28 the energy spectra evolution for the parameter values $t = 1$, $d = t/6$, $\mu = 3d - 4t$, a) $B_y = 0.5d$, b) $B_y = d$, c) $B_y = d$, $\alpha = 0.2d$, $\Delta_s = 0.5d$ and d) $B_y = 4d$, $\alpha = 0.2d$ and $\Delta_s = 0.3d$ are shown, for several values of disorder strength λ. [2] Figure 4.29 shows the results for the density of states of the corresponding cases a)-d) of figure 4.28. Here the DOS is obtained from exact diagonalization of the system with size $N_y = 76$. It is such that a number of states $N(\Delta_E)$ is obtained for an energy interval Δ_E centered at an energy E, and normalized by the system size, as:

$$\rho(E) = \frac{N(\Delta_E)}{N_y \times N_k}, \tag{4.9}$$

where N_y is the number of y sites and N_k is the number of k_x points.

Figure 4.28 a) shows a case where the system has gapless edge states and the bulk gap is not closed by B_y, hence we are outside the shaded region depicted by figure 3.7. As λ is increased, the edge states lose their structure and the bulk gap is closed. Accordingly, there is an increase in the density of states at $E = 0$ and around zero energy as it can be seen in figure 4.29 a). Case b) corresponds to a gapless phase with both edge states and a range of k_x supporting Majorana flat bands. As disorder is increased, the bulk remains gapless and there is a sharp increase in the density of states at zero energy, as the bulk states come from finite energies to lower energies. The sharp peak in the DOS observed at E=0 is reminiscent of the characteristic behaviour of a two-dimensional disordered D class superconductor in the thermal metal regime [84] in which the density of states displays a logarithmic divergence at zero energy. One important remark is that the flat band states in b) are not lifted by Anderson disorder to finite energies. This is also verified for regimes with a higher value of B_y. This result is in accordance to what was observed in ref. [8] for Gaussian on-site disorder. In c), a finite value of spin-orbit coupling and of s-wave pairing are added to b), and the model describes a noncentrosymmetric superconductor. The time reversal-like symmetry $\mathcal{T}_{k_y}$ is preserved but the particle hole-like symmetry $\mathcal{P}_{k_y}$ is broken. There is an exception at the points $(k_x, k_y) = (n\pi, m\pi)$ with $m, n \in \mathbb{Z}$ where the symmetry remains valid. As a result, the energy spectrum for a fixed value of momentum loses the symmetry around $E = 0$, except at $k_x = 0$, where the symmetry is preserved. This also leads to a breaking of the chiral-like symmetry

[2] Note that, in any case, as disorder is increased the superconductivity may eventually be destroyed. However, we do not take this into account here, and the superconducting pairing parameters d and Δ_s are imposed and taken as fixed values.

$\mathcal{S}_{k_y}$ which protects the flat bands, and they are lifted to a finite energy. As disorder is introduced in the system in c), the edge states are destroyed and the considered energy range gets filled with bulk states, but the tilt of the spectrum is preserved. As a result, the flat bands which were previously lifted to finite energies do not collapse to zero energy. For high values of λ the density of states exhibits two peaks which result from the inclination of the bulk energy spectrum.

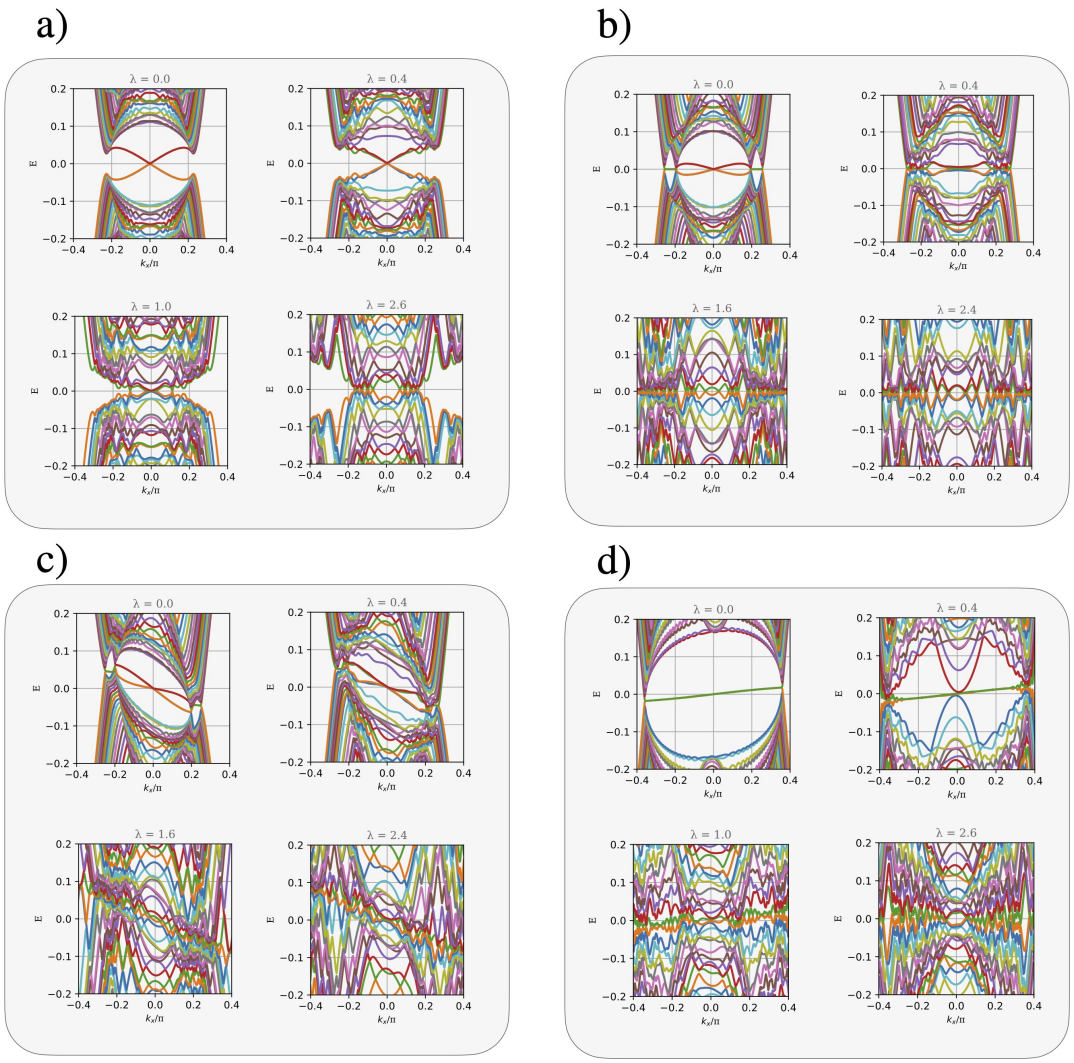

Figure 4.28: Energy spectra evolution with Anderson disorder for a) $B_y = 0.5d$, b) $B_y = d$, c) $B_y = d$, $\alpha = 0.2d$, $\Delta_s = 0.5d$, d) $B_y = 4d$, $\alpha = 0.2d$, $\Delta_s = 0.3d$.

In figure 4.28 d), the system also describes a noncentrosymmetric superconductor with mixed p and s-wave pairings. The values of the p-wave pairing and spin orbit term are kept constant in relation to case c), but the s-wave pairing term is decreased from $\Delta_s = 0.5d$ to $\Delta_s = 0.3d$ and the magnetic field is increased from $B_y = d$ to $B_y = 4d$. The system is in the regime where unidirectional MESs appear. The spectrum acquires a tilt in the opposite direction if compared to c), which is a result of the increased magnetic field. The Majorana edge states are robust to small values of disorder strength (as it can be seen in the figure for $\lambda = 0.4$) but as disorder increases the structure of the band is lost, as bulk states fill the lower energy values. This differs from case c) where the tilt of the spectrum is preserved even at

higher values of disorder. In d) as disorder is increased there is at first an increase in the value of the DOS at zero energy, which then decreases for higher values of disorder. This can be seen in figure 4.29 d). For $\lambda > 1.8$ the density of states becomes nearly constant in the considered range of $E \in [-0.4, 0.4]$.

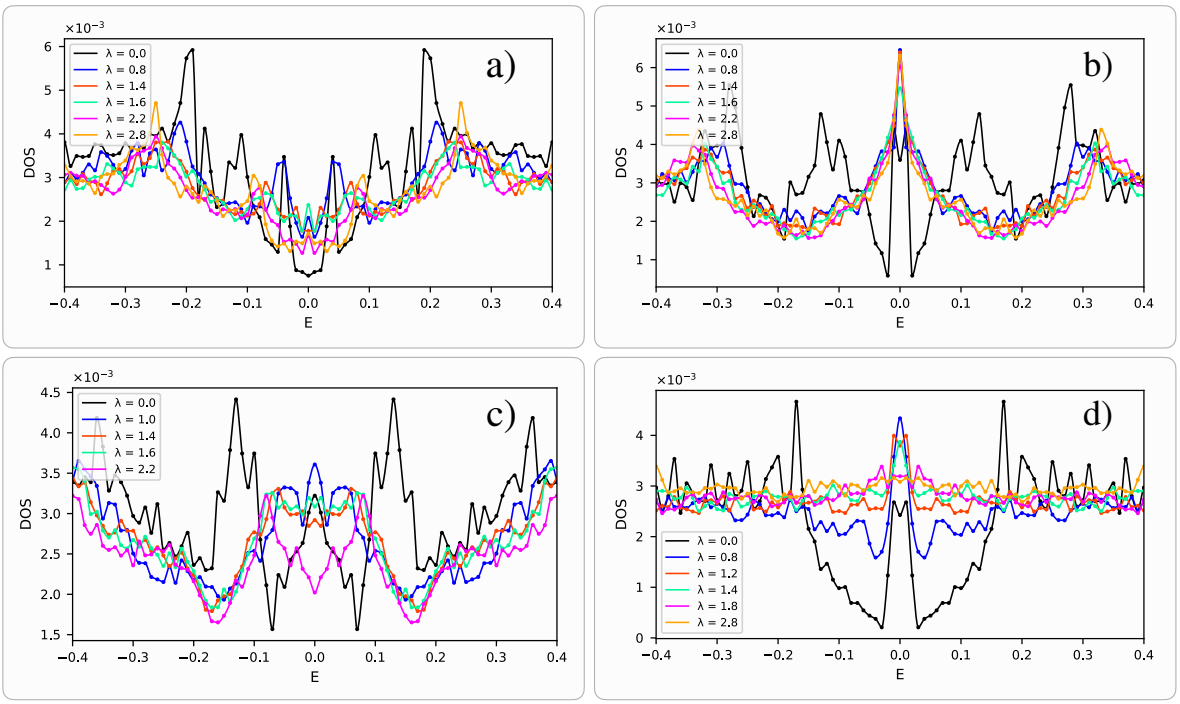

Figure 4.29: Density of states evolution with Anderson disorder for $E \in [-0.4, 0.4]$, for the parameter values a) $B_y = 0.5d$, b) $B_y = d$, c) $B_y = d$, $\alpha = 0.2d$, $\Delta_s = 0.5d$, d) $B_y = 4d$, $\alpha = 0.2d$, $\Delta_s = 0.3d$.

Aubry-André disorder

We now consider the same parameter values but with added Aubry-André disorder. Figures 4.30 a)-d) portrait the main results found.

Figure 4.30 a) shows a case where the system has gapless edge states and the bulk gap is not closed by B_y, hence we are outside the shaded region depicted by figure 3.7 and there are no flat bands before introducing quasi-disorder. These edge states remain robust for small values of the quasi-periodic potential strength ($\lambda < 0.8$). Around $\lambda = 1.2$ the bulk gap is closed and a new flat band appears, which then splits in two and disappears as a gap opens in the system for around $\lambda = 1.8$. Figure 4.31 shows the DOS for some values of disorder λ. The appearance of MFBs leads to an increase of the density of states at zero energy, as it can be seen in figure 4.31 a) for the value of $\lambda = 1.4$. At higher values of disorder, the system is gapped and the DOS at $E = 0$ goes to zero. The reopening of the gap contrasts with what was found for Anderson disorder in figure 4.28 a), where the bulk remains gapless as disorder is increased. Figure 4.32 shows the edge states of the clean system in a), and in b) the zero energy states inside the flat band that appears with increased disorder. In the two cases the states appear localized at both edges simultaneously. While the edge states of the clean system are localized symmetrically on both edges, the flat band states lose this symmetry and localize more near one of the edges. Near the edge on which a given state appears less localized, there is also a deviation from the

edge, and the state mostly localizes on the subsequent sites in y.

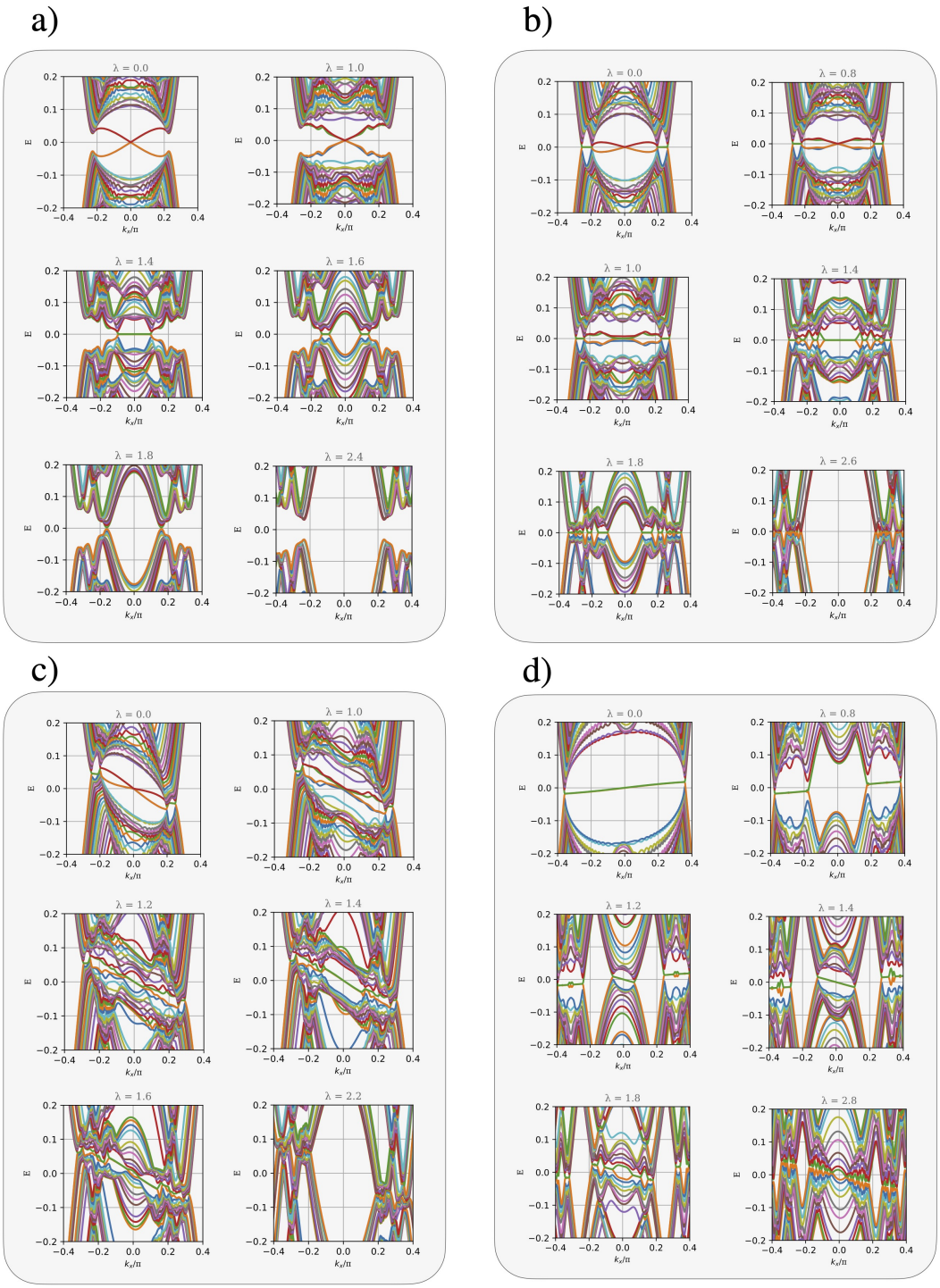

Figure 4.30: Energy spectra evolution with Aubry-André disorder for a) $B_y = 0.5d$, b) $B_y = d$, c) $B_y = d$, $\alpha = 0.2d$, $\Delta_s = 0.5d$, d) $B_y = 4d$, $\alpha = 0.2d$, $\Delta_s = 0.3d$. A more detailed evolution of the spectra, as well as more cases with different parameter values, can be found in Appendix C.

In figure 4.30 b) the clean system is in a gapless phase with both edge states and MFBs in the range where k_x is nontrivial. The edge states appear once again to be robust up until around $\lambda \approx 0.8$.

However, the MFBs which are present at $\lambda = 0$ are more robust if compared with the edge states, with the band staying at zero energy but the initial range of k_x hosting flat bands decreasing as λ increases. Simultaneously, flat bands appear for new values of k_x, as it can be seen in the figure for $\lambda = 1.4$, and accordingly, the density of states at zero energy increases. Note however that the behaviour of $\rho(E = 0)$ is not monotonic, as is the case in a). At higher values of disorder there is a collapse of states to lower energies and the density of states exhibits a peak at $E = 0$ which is reminiscent of the behaviour found for Anderson disorder (figure 4.29). Contrary to what is observed in a) for a lower magnetic field, there is no opening of the bulk gap for larger values of λ. When quasi-periodic disorder is introduced, it was seen that a gap will only open for larger values of λ if the bulk was gapped prior to introducing disorder, as in a), otherwise the bulk will remain gapless.

The cases c) and d) introduce spin-orbit coupling α and s-wave pairing, and as before, the model describes a noncentrosymmetric superconductor with mixed p and s-wave pairings. Case c) seems to have a similar evolution to b), except that the spectrum has a tilt resulting from the symmetry breaking that comes with the added spin orbit and s-wave terms. Instead of new flat band regimes, new unidirectional edge states appear. Unlike what happens for Anderson disorder, at high values of λ a gap opens for values of k_x around $k_x = 0$ (although the bulk as a whole remains gapless). This is reflected in the density of states, that drops around $E = 0$ for higher disorder values. Similarly to what was observed for Anderson disorder, the tilt of the energy spectrum is preserved as disorder increases.

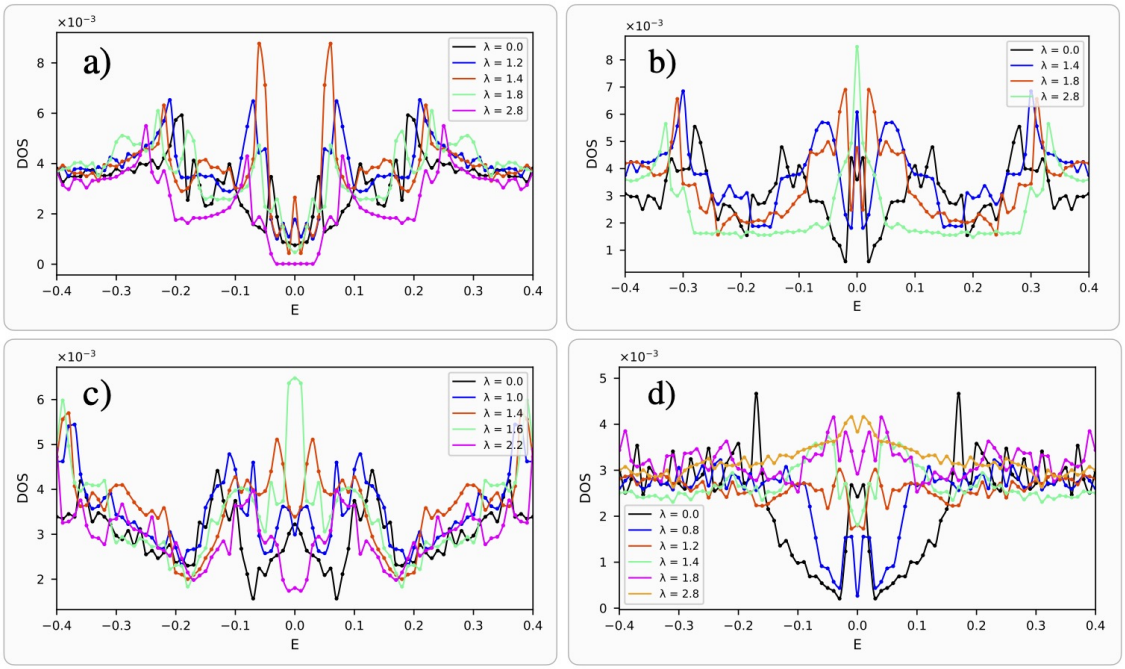

Figure 4.31: Density of states evolution with Aubry-André disorder for $E \in [-0.4, 0.4]$, for the parameter values a) $B_y = 0.5d$, b) $B_y = d$, c) $B_y = d$, $\alpha = 0.2d$, $\Delta_s = 0.5d$, d) $B_y = 4d$, $\alpha = 0.2d$, $\Delta_s = 0.3d$.

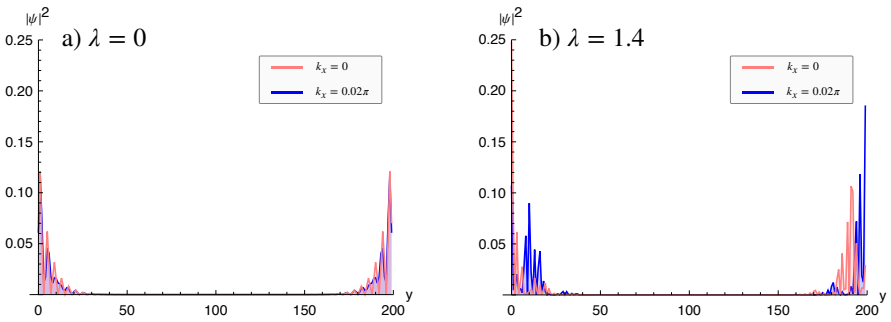

Figure 4.32: a) Edge states of the clean system with size $N_y = 200$ and magnetic field $B_y = 0.5d$, at $k_x = 0$ (zero energy state) and $k_x = 0.02\pi$ (finite energy state). b) Flat band zero energy states of the quasi-disordered system at $B_y = 0.5d$, $\lambda = 1.4$.

In d) the clean system possesses unidirectional edge states. When a certain value of disorder is reached, "flipped" unidirectional states appear in the system. This is seen clearly in 4.30 d) for the values of $\lambda = 1.2$ and $\lambda = 1.4$, as a band with negative slope appears for values of k_x around $k_x = 0$. At $\lambda = 1.2$ there is a coexistence of unidirectional "flipped" left-moving edge modes (with negative slope) around $k_x = 0$ and right-moving edge modes (with positive slope) for higher (absolute) values of k_x. As discussed in section 3.3.3, a backflow current that balances the current on the edges is created on the bulk: extra right or left moving modes will appear depending on the net current on the edges. Figure 4.33 shows a) a undirectional state of the clean system and b) a "flipped" state at $\lambda = 1.2$. Both wavefunctions are localized at both edges simultaneously and the disordered state is nearly symmetric on both edges, contrasting with the flat band states presented in 4.32. For $\lambda > 1.2$ the structure of the right-moving unidirectional states starts to be lost. At higher values of disorder the energy spectrum acquires a tilt in the opposite direction to that of the clean system.

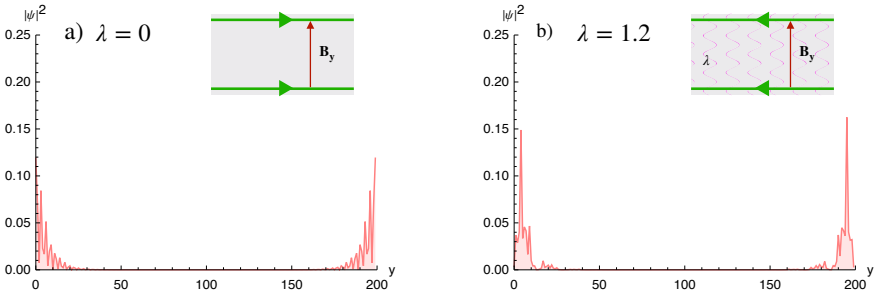

Figure 4.33: a) MES for $E = 0$, $k_x = 0$ and with no disorder, for a system with $N_y = 200$ and parameters corresponding to figure 4.30 d). b) State at $E = 0$, $k_x = 0$ with quasi-periodic potential of strength $\lambda = 1.2$ and a random value of ϕ. The state has a flipped velocity, as is seen in the energy spectrum.

4.2.2 Quasi-disorder induced Majorana Flat Bands

We want to investigate if the MFBs that arise in the presence of the quasi-periodic potential have a topological nature, such as in the case of the MFBs in the ordered system, as discussed in Section 3.3.1. One possibility is to calculate the winding number $\mathcal{W}$ in real space. An approach suitable for disordered systems is discussed in [85–87] and involves a reformulation of the k-space expression to real-space, to calculate a "non-commutative" winding number. This is done by writing the chiral symmetry matrix $\mathcal{S}$ in a real-space representation and writing the real-space Hamiltonian $\mathcal{H}$ in an anti-diagonal block form. The key point of this approach is the geometrical calculation of a commutator between the anti-diagonal block and the position operator. This however was not implemented here. Instead, since the Berry phase was found to be quantized to a value of π in the clean system in the region of MFBs, we calculate it here for the disordered case.

The Berry phase is obtained in real space using twisted boundary conditions, similarly to the approach to the calculation of the Chern number (Appendix B). Considering a twisted boundary phase θ_y we have:

$$\gamma = i \int_0^{2\pi} d\theta_y \langle \Psi(\theta_y) \mid \frac{\partial}{\partial \theta_y} \Psi(\theta_y) \rangle \tag{4.10}$$

where Ψ denotes the ground-state many body wavefunction, which is given by the Slater determinant of the single particle wavefunctions. We can represent the ground state wavefunction by an $M \times N$ matrix $\mathbf{\Psi}^{\theta_y}$ where N is the number of sites in y and M is the number of occupied states (negative energy states). Numerically, the twist variable is discretized into L points between 0 and 2π, such that θ_y is constrained to take the values $\theta_{y,n} = \frac{2\pi}{L} n$, with n an integer that goes from 0 to $L-1$. A link variable can then be defined as $U(\theta_{y,n}) = \det\left[\mathbf{\Psi}^{\dagger}_{\theta_{y,n}} \mathbf{\Psi}_{\theta_{y,n+1}}\right]$, and the Berry phase is obtained as

$$\gamma = -\mathrm{i} \sum_{n=1}^{L} \log U(\theta_{y,n}). \tag{4.11}$$

The results for two sets of parameters are presented in figures 4.34 and 4.35. Similarly to the ordered case, the MFBs that arise in the presence of the Aubry-André potential reveal a π-quantized Berry phase. Figure 4.34 concerns the case of $B_y = 0.5d$ where the system has a bulk gap previously to introducing the quasi-periodic potential and hence a transition to a π-quantized Berry phase occurs. For $\lambda = 1.4$ (left) we have a single band that then splits in two (middle) and at $\lambda = 1.8$ (right) the Majorana flat band has dissapeared as the gap reopens and the Berry phase is zero for all k_x. Figure 4.35 is the case of $B_y = d$ where the spectrum was already gapless but the quasi-periodic potential causes the appearance of new regions with MFBs. Similarly to the case of $B_y = 0.5d$ the center band splits in two with a gap opening at $k_x = 0$. Figures 4.34 and 4.35 are obtained for random values of ϕ in the Aubry-André potential. It was verified that the regimes of k_x for which the Berry phase becomes π-quantized are independent of ϕ, and the MFBs appear for any value of ϕ.

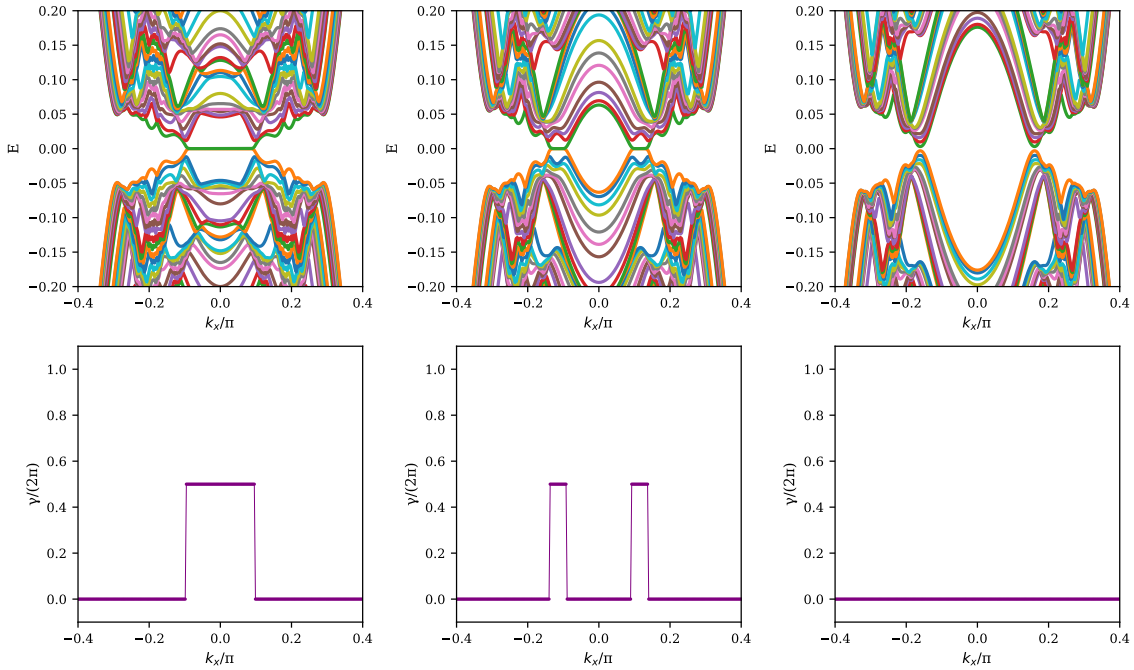

Figure 4.34: Energy spectrum evolution for a system with 76 sites in y for different values of λ vs. Berry phase normalized by 2π as a function of k_x, for a random value of ϕ in the quasi-disorder potential. The values of the parameters are $t = 1$, $d = t/6$, $\mu = 3d - 4t$, $By = 0.5d$ and $\lambda = 1.4$ (left), $\lambda = 1.6$ (middle), $\lambda = 1.8$ (right).

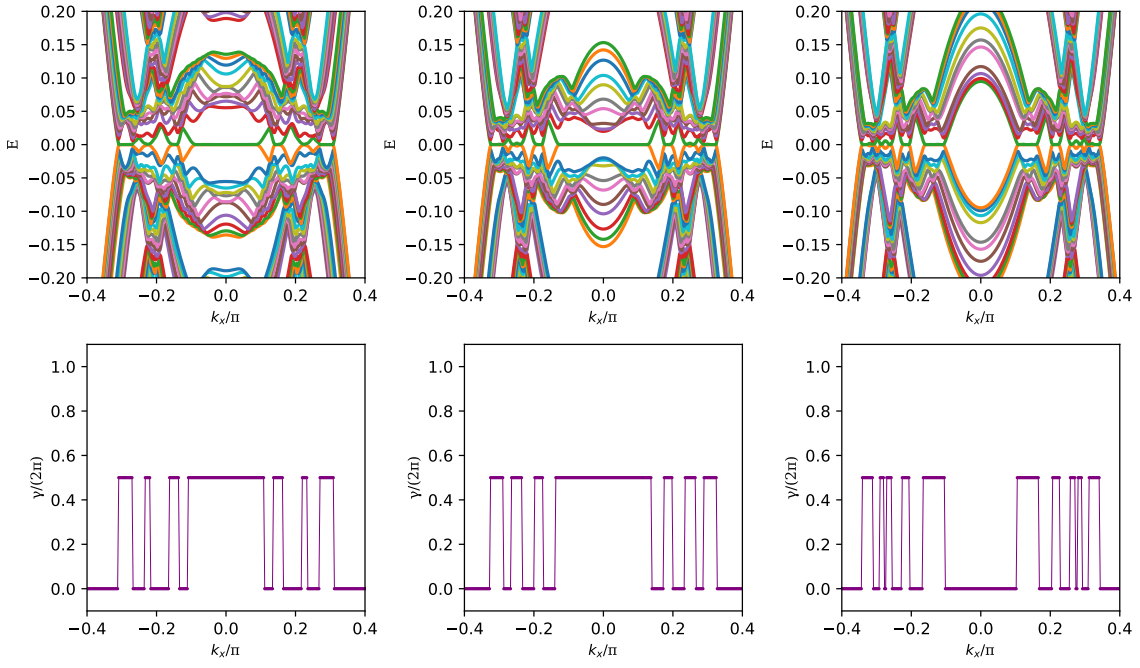

Figure 4.35: Energy spectrum evolution for a system with 76 sites in y for different values of λ vs. Berry phase normalized by 2π as a function of k_x, for a random value of ϕ in the quasi-disorder potential. The values of the parameters are $t = 1$, $d = t/6$, $\mu = 3d - 4t$, $By = d$ and $\lambda = 1.4$ (left), $\lambda = 1.6$ (middle), $\lambda = 1.8$ (right).

To quantify the induced bands at zero energy and study the transition to a π-quantized Berry phase,

we use the concept of Majorana pair density. This is defined as [88]

$$\rho_\gamma = \frac{N_\gamma}{N_k} \tag{4.12}$$

where N_k is the number of discrete points of k_x taken inside the interval $[-\pi, \pi]$, and N_γ is the number of such points which support MFBs at the edges. Numerically it is more convenient to consider the number of k_x points for which the Berry phase is quantized to π, N_π, since it was found that $N_\pi = N_\gamma$. A transition from $\rho_\gamma = 0$ to $\rho_\gamma \neq 0$ then signals a transition from a trivial to a topological regime (π-quantized Berry phase). Figure 4.36 a) shows the evolution of ρ_γ as a function of the quasi-disorder strength λ for the case $t = 1$, $d = t/6$, $\mu = 3d - 4t$ and $B_y = 0.5d$ (figure 4.30 a)), for the range $\lambda \in [1, 2]$ with a step 0.01 in λ. Outside this range, ρ_γ remains zero. A transition $\rho_\gamma = 0 \to \rho_\gamma \neq 0$ occurs between $\lambda = 1.22$ and $\lambda = 1.23$ at a certain critical value $\lambda_{C,1}$. The value of ρ_γ grows until 1.49 ± 0.01 when the flat band splits in two and the behaviour of ρ_γ changes, with an abrupt change in the sign of the second derivative. A second transition occurs between 1.79 and 1.8, at a critical value $\lambda_{C,2}$, where ρ_γ becomes zero. It is understood that both transitions should be continuous in the limit $N_k \to \infty$, where ρ_γ would grow continuously from zero. In figure 4.36 b) the density of states at zero energy $\rho(E = 0)$ (normalized by the system size) is shown, for the same parameters and system size as in figure 4.36 a), along with the corresponding contribution for the zero energy density of states which comes from the MFB, $\rho(E = 0)_\gamma$. Inside the topological phase, which is highlighted, we can see that the finite value of $\rho(E = 0)$ observed for the system with OBC comes almost entirely from the presence of flat bands.

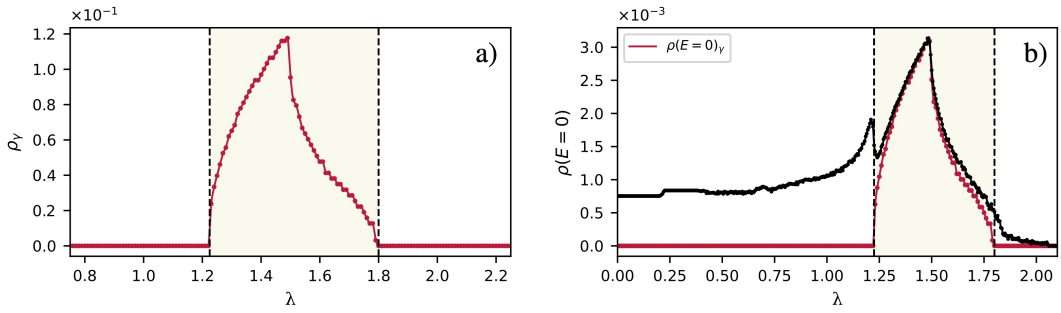

Figure 4.36: a) Values of ρ_γ for the case $t = 1$, $d = t/6$, $\mu = 3d - 4t$ and $B_y = 0.5d$ (figure 4.30 a)) vs. quasi-disorder strength λ. Obtained for a system with 76 sites in y. b) Value of the DOS at $E = 0$ for the same parameter values as in a), vs. quasi-disorder strength λ, and the contribution for $\rho(E = 0)$ which comes from the Majorana flat bands in the corresponding regime.

N_y	$\lambda_{C,1}$	$\lambda_{C,2}$
76	1.225 ± 0.005	1.800 ± 0.005
100	1.215 ± 0.005	1.775 ± 0.005
175	1.230 ± 0.005	1.805 ± 0.005
200	1.220 ± 0.005	1.800 ± 0.005
400	1.230 ± 0.005	1.805 ± 0.005
800	1.225 ± 0.005	1.805 ± 0.005

Table 4.1: Values of the critical exponents $\lambda_{C,1}$ and $\lambda_{C,2}$ for the system sizes $\{76, 100, 175, 200, 400, 800\}$.

Table 4.1 shows the values of $\lambda_{C,1}$ and $\lambda_{C,2}$ for several system sizes. These values were obtained for random values of the phase ϕ in the Aubry-André potential, and the uncertainty is taken as the minimum interval considered between values of λ. It is found that the values of the critical points show little variation with the system size.

4.2.3 Scaling of the density of states: critical exponents

A detour to the clean case

Let us first briefly consider the clean system, without disorder. For the clean case, it is possible to obtain the values of the dynamical exponent z and of the critical exponent ν analytically, for the transition that occurs as B_y is increased, corresponding to a transition from a winding number of 0 to 1 or a Berry phase of 0 to π. Here we consider the case of $\mu < -2t$ (such that the topological phase is within the region described by equation 3.38). At the topological transition to a gapless phase, the gap closing points in k_x, $k_{x,0}$, are given by

$$k_{x,0} = \pm \arccos\left[-\frac{2(t\mu + 2t^2)}{-d^2 + 4t^2}\right] + 2n\pi,\ n \in \mathbb{Z}. \tag{4.13}$$

The values of k_y for which the gap closes are given by $k_{y,0} = n\pi$, $n \in \mathbb{Z}$ (general solution). In this case the transition happens at $k_{y,0} = 2n\pi$, $n \in \mathbb{Z}$. The gap closes at a critical value of the magnetic field, B_{y_C}, which, fixing $k_y = k_{y,0}$, is defined from the value of $k_{x,0}$ as

$$B_{y_C}^2 = \left[\mu + 2t\left(\cos k_{x,0} + 1\right)\right]^2 + d^2 \sin^2 k_{x,0}. \tag{4.14}$$

We can now first expand the expressions for the bulk energy, 3.24, around $k_{x,0}$ to find the dependence of the energy on k_x. There are four energy bands, but the two middle bands (which have a lower energy, in absolute value) dictate the closing of the bulk gap. Close to the critical point, we assume $B_y^2 \sim \left[\mu + 2t\left(\cos k_x + 1\right)\right]^2 + d^2 \sin^2 k_x$. We only need to consider the first positive energy band, which as a function of k_x, and taking $k_y = k_{y,0}$ simplifies to:

$$E_+(k_x) = \sqrt{z_1 - 2\sqrt{z_2}} \tag{4.15}$$

with

$$z_1 = 2\alpha, \quad z_2 = \alpha^2 \tag{4.16}$$

and

$$\alpha = \left[\mu + 2t\left(\cos k_x + 1\right)\right]^2 + d^2 \sin^2 k_x. \tag{4.17}$$

Expanding $E_+(k_x)$ around $k_{x,0}$ shows $E_+(k_x) \propto (k_x - k_{x,0})$, implying a value of the dynamical exponent $z = 1$ for the transition, according to equation 2.50.

We can now take $k_x = k_{x,0}$ and see how the gap closes as a function of B_y. We find

$$E_+(k_x = k_{x,0}) = \sqrt{B_{yc}^2 + B_y^2 - 2\sqrt{B_{yc}^2 B_y^2}} = ||B_{yc}| - |B_y|| \,. \tag{4.18}$$

Therefore at $k_x = k_{x,0}$ the gap vanishes linearly, with an exponent $\nu z = 1$, according to equation 2.49. Since $z = 1$, this implies $\nu = 1$, and

$$z = 1, \quad \nu = 1. \tag{4.19}$$

We can now investigate if numerical and analytical results agree in the case of the trivial-topological transition. To do this, the results for the density of states at the first transition ($0 \to \pi$) and around it are obtained for a system of size $N_y = 400$. From equations 4.13 and 4.14 it is obtained that for the usual values of t, d and μ, the critical value of $B_{y,C}$ for the first transition is $B_{y,C} \approx 0.1097$. By inspection of the energy spectrum at the critical value of B_y we can see that we should seek a typical scaling behaviour of the density of states around $E \in [0, 0.025]$. This can be seen in figure 4.37, as outside this range, bulk states which do not contribute to the closing of the bulk gap will be accounted for in the DOS. This is not only seen from the energy spectrum but also from a change in the behaviour of the density of states at low energies. At the critical point the DOS is expected to behave according to equation 2.48. A fit is done to a function of the form

$$(C_1|E|)^{\frac{d}{z}-1} \tag{4.20}$$

where $d = 2$ and C_1 is a constant.

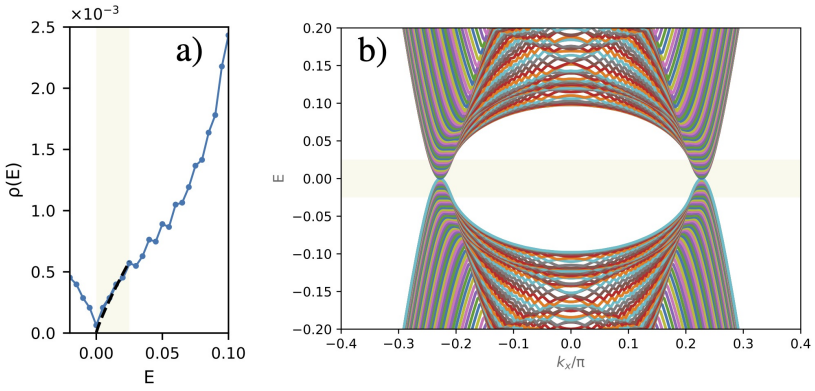

Figure 4.37: a) Density of states $\rho(E)$ at the critical value of the magnetic field, $B_{y,C}$, and fit of a function of the form of equation 4.20 to the energy range E $\in$ $[0.005, 0.025]$ (black dashed line). Obtained for a system with PBC with size $N_y = 400$, and using a number of k_x points $N_k = 629$. b) Energy spectrum for the same parameter values and the same system size as in a), with PBC. The energy region E $\in [-0.025, 0.025]$ is highlighted.

In figure 4.37 a) the density of states $\rho(E)$ at the gap closing point is presented for low energies, as well as the bulk spectrum in 4.37 b). Both figures are obtained for the system with periodic boundary conditions. The value of z obtained was of $z = 1.08 \pm 0.07$, which corresponds to a deviation of 8% from the analytical result of $z = 1$. Also, we can note in figure 4.20 a) that the value of the density of states at

zero energy, $\rho(E = 0)$, is not zero, which is not accounted for in equation 4.20. [3]

Now we are interested in obtaining the value of ν numerically. For values of B_y close to the critical point, which correspond to small values of δ, a collapse of the scaled values of the DOS according to equation 2.47 is expected. This should hold for small values of δ and also for energy values close to zero energy. From here the value of ν can be estimated. We take values of $B_y > B_{y,C}$, where the energy spectrum becomes gapless, as for $B_y < B_{y,C}$ the system is in a gapped phase.

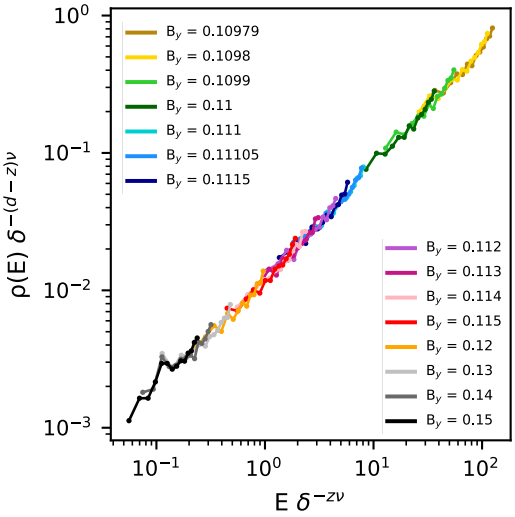

Figure 4.38: Density of states for $E \in [0.02, 0.09]$ and several values of B_y close to the critical value, $B_{y,C}$, scaled according to equation 2.47 for $z = 1.08$ and $\nu = 0.95$.

The results for the scaled density of states for several values of B_y close to the transition point are presented in figure 4.38, for the values $z = 1.08$ and $\nu = 0.95$. There is a good agreement with the analytical results and the gap closing exponent remains close to one, with $z\nu = 1.026$.

$B_{y,C}$	z	ν
0.1097	1.08 ± 0.07	0.95 ± 0.05

Table 4.2: Values of z and ν obtained numerically for the topological transition in the clean case.

Aubry-André: numerical determination of z and ν

Going back to the disordered case, we now want to investigate the scaling properties around the topological transitions $(0 \to \pi)$ and $(\pi \to 0)$. A numerical approach is now necessary. First, to estimate the values of the dynamical exponents z for both transitions, the density of states is obtained at the critical values of disorder obtained in the previous section for the system size $N_y = 800$. The values of t, d, μ and B_y remain constant and only the value of the quasi-disorder strength, λ, is varied.

Figures 4.39 and 4.40 show the density of states at the critical points $\lambda_C = 1.225$ and $\lambda_C = 1.805$, respectively, along with the bulk spectra. A region of interest, where a characteristic behaviour of $\rho(E)$

[3] At the gap closing point, the DOS calculated for the interval around zero energy will have a small contribution of the bulk states of lowest absolute finite energy. Since in the thermodynamic limit and exactly at the critical point $\rho(E = 0)$ should be zero the choice was made as to exclude the point $E = 0$ from the fit.

should be seen, is found close to zero energy for $E \in [-0.025, 0.025]$. This is seen both in the graphs of $\rho(E)$ and by inspection of the energy spectra. Figures 4.39 a) and 4.40 a) show a fit of the density of states according to equation 4.20, again excluding the point $\rho(E = 0)$. We obtain for the first transition at $\lambda_{C,1} = 1.225$ a value of the dynamical critical exponent $z = 1.27 \pm 0.04$ and for the second transition at $\lambda_{C,2} = 1.805$ a value of $z = 1.23 \pm 0.03$.

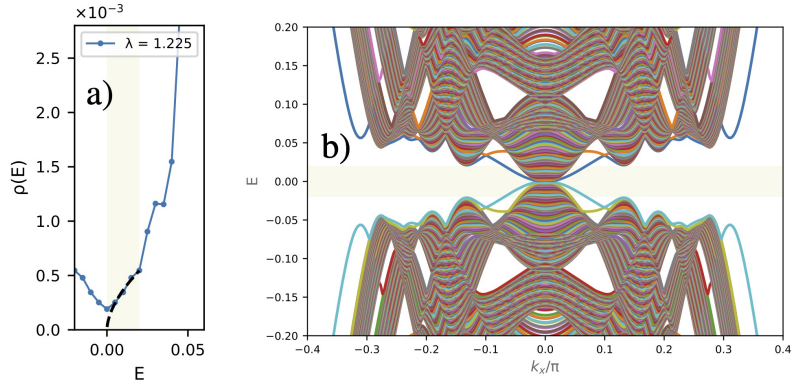

Figure 4.39: a) Density of states $\rho(E)$ at the critical value of the disorder strength, $\lambda_{C,1} = 1.225$, and fit of a function of the form of equation 4.20 to the energy range $E \in [0.005, 0.025]$ (black dashed line). Obtained for a system with PBC with size $N_y = 800$, and using a number of k_x points $N_k = 629$ and averaged over 10 disorder configurations. b) Energy spectrum for the same parameter values and the same system size as in a), with PBC and $\phi = 0$ in the quasi-periodic potential. The energy region $E \in [-0.025, 0.025]$ is highlighted.

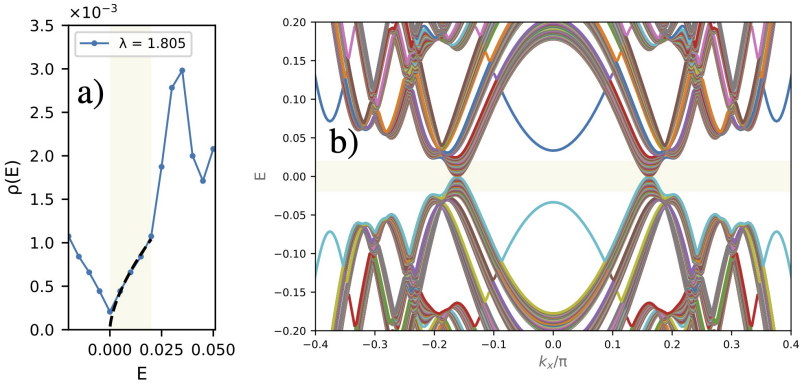

Figure 4.40: a) Density of states $\rho(E)$ at the critical value of the disorder strength, $\lambda_{C,2} = 1.805$, and fit of a function of the form of equation 4.20 to the energy range $E \in [0.005, 0.025]$ (black dashed line). Obtained for a system with PBC with size $N_y = 800$, and using a number of k_x points $N_k = 629$ and averaged over 10 disorder configurations. b) Energy spectrum for the same parameter values and the same system size as in a), with PBC and $\phi = 0$ in the quasi-periodic potential. The energy region $E \in [-0.025, 0.025]$ is highlighted.

We now want to determine the value of ν. We take values of λ inside the topological (gapless) phase, $\lambda > 1.225$ and $\lambda < 1.805$, and obtain the density of states close to zero energy.

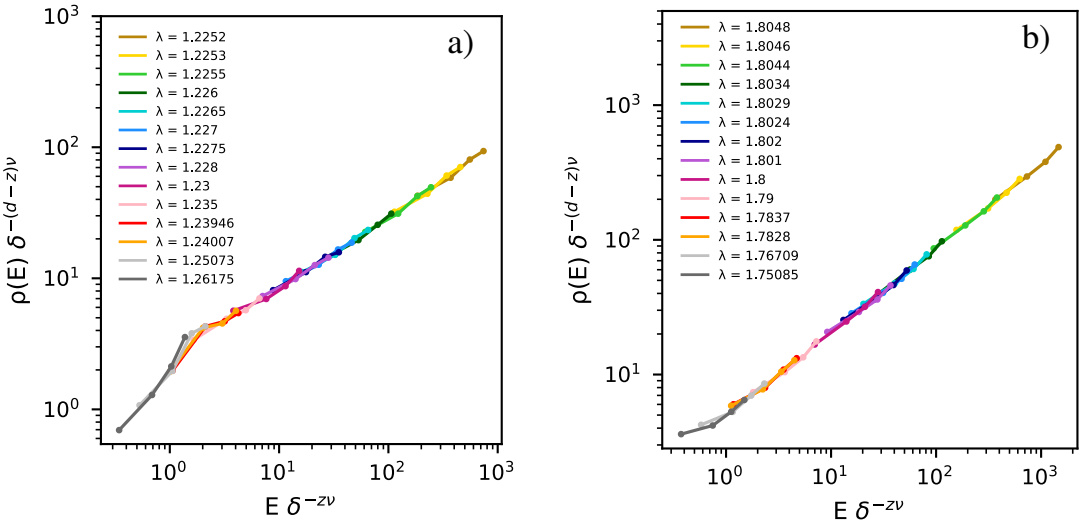

Figure 4.41: Density of states for $E \in [0.005, 0.025]$ and several values of λ close to the critical values, a) $\lambda_{C,1} = 1.225$ and b) $\lambda_{C,2} = 1.805$, scaled according to Equation 2.47 for a) $z = 1.27$, $\nu = 0.95$ and b) $z = 1.23$, $\nu = 1.00$.

In figure 4.41 we show the results for scaled the density of states for: a) values close to the first transition at $\lambda_{C,1} = 1.225$, and b) values close to the second transition at $\lambda_{C,2} = 1.805$. The density of states shows a collapse for a) $z = 1.27$, $\nu = 0.95$ and b) $z = 1.23$, $\nu = 1.00$. Since a bigger system size is considered in relation to what was studied in the clean case we achieve a better agreement in behaviour of the density of states and expect these numerical results to be more accurate.

The quantum phase transitions in the disordered regime are therefore in a different universality class than that of the clean case, which was found to behave with $z = \nu = 1$. The obtained values also differ significantly from the known results for the Anderson or the Aubry-André transitions in one dimension, the first belonging to an universality class with with $\nu = 2$ and $z = 2/3$, and the second case with critical exponents $\nu = 1$ and $z = 2.375$ [89]. Recent results show that for a one dimensional system with p-wave superconductivity subject to an Aubry-André potential the quasi-disorder driven transitions also deviate from the normal Aubry-André class. For the localized-critical transition line and when the p-wave pairing term is finite, the correlation length exponent was obtained as $\nu = 0.997$ and the dynamical exponent as $z = 1.373$ in [40], and as $\nu = 1.000$, $z = 1.388$ in [41]. Note, however, that the referred results are for $d = 1$ while we are studying a two dimensional system, and also concern systems with no applied magnetic field. Up to numerical errors, the values of ν obtained for the disordered driven transitions coincide with that of the Aubry-André transition; nevertheless the value of z deviates from that of the known classes, which suggests these transitions belong to novel universality classes. The identified transitions, where MFBs appear as a result of a quasi-disorder induced gap closing, and the subsequent opening of the bulk gap, are found to happen for other values of the imposed parameters. Taking μ, t and d at the same fixed values, as long as $B_y < B_{y,C}$ (when the bulk is gapless) with $B_{y,C}$ is defined as in equation 4.14) the same type of transitions will take place with the increase of λ. It is likely that the obtained values apply to the whole transition line in the (λ, B_y) phase diagram space, and that the fixed

value of B_y does not confer any loss of generality. It is important to note, however, that the bulk gap will not close as a result of increased quasi-disorder if the applied magnetic field in the y direction is zero. This can be seen in the appendix figure C.1.

λ_C	z	ν
1.225	1.27 ± 0.04	0.95 ± 0.05
1.805	1.23 ± 0.03	1.00 ± 0.05

Table 4.3: Values of z and ν obtained numerically for the topological transitions in the disordered case.

4.2.4 Fractal analysis

As discussed in Chapter 2, the scaling of the generalized IPR can be used to obtain information about the fractal nature of the wavefunctions, through the values of the exponent $\tau(q)$ defined in equation 2.39, and the generalized dimension $D(q)$. Here k_x is taken at fixed values, such that system is reduced to an effective one dimension. The IPR as a function of q is calculated and averaged within a certain energy range. We fix the parameters $t = 1$, $d = t/6$, $\mu = 3d - 4t$ and $B_y = 0.5d$ and consider both the cases of Aubry-André disorder and Anderson disorder.

Anderson disorder

First we want to study the Anderson disorder case. We consider bulk states at low energies, and exclude the edge states. For states within a fixed energy range $E \in [0.05, 1]$ the IPR is obtained and averaged over, for several system sizes. The number of states in each disorder configuration varies, but we know the states are within the selected range. For each value of q, and each value of disorder strength, the averaged value of the IPR is fitted to a function of the form

$$\mathcal{IPR}(q) = CL^{\tau(q)} \tag{4.21}$$

where L is the system size, which here corresponds to the number of sites in y, N_y, and C is a constant. The sizes of the system considered are $L \in \{75, 100, 150, 175, 200, 255, 275, 400, 475, 600, 675, 800\}$ and we fix the values of k_x.

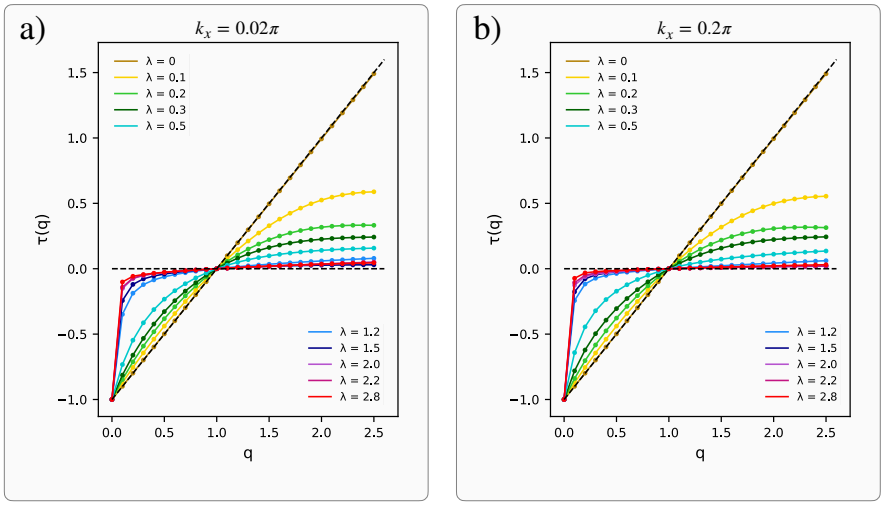

Figure 4.42: Results of τ vs. q, for several values of Anderson disorder strength, λ, for a) $k_x = 0.02\pi$ and b) $k_x = 0.2\pi$. The IPR is averaged for the states within the energy range $E \in [0.05, 1]$.

Figure 4.42 shows the values of $\tau(q)$ for $k_x = 0.02\pi$ and $k_x = 0.2\pi$, for several values of disorder strength λ and considering all the values within the interval for the system size, L. The results are obtained for states within the energy range $E \in [0.05, 1]$. We recall that in the clean system the bulk gap is of the order of $E \approx 0.04$ (although the value of the gap is not the same for each k_x). One thing that

can be immediately noticed is that for the clean system, $\lambda = 0$, the values of $\tau(q)$ closely follow the line $\tau(q) = (q-1)$, indicating that $D(q)$ is $q-$independent and equal to 1. This is the expected behaviour of the clean system (taking a fixed k_x where the system is reduced the one dimension) and reveals that the bulk states are extended in the y direction. For higher values of disorder, $\tau(q)$ approaches the line $\tau(q) = 0$, where $D(q) = 0$, suggesting the states are localized and possess a single-fractal nature, with $D(q)$ being close to zero for all q. For other values of disorder strength, starting at $\lambda = 0.1$, $\tau(q)$ does not follow a behaviour characteristic either of $D(q) = 1$ or $D(q) = 0$. In order to take a conclusion, it is necessary to evaluate $\tau(q)$ as the system size tends to infinity. To do this, several subintervals of L are considered, to which a fit of equation 4.21 is done:

$$\begin{aligned} L_1 &= \{75, 100, 150, 175, 200, 255, 275, 400, 475, 600, 675, 800\}, \\ L_2 &= \{150, 175, 200, 255, 275, 400, 475, 600, 675, 800\}, \\ L_3 &= \{200, 255, 275, 400, 475, 600, 675, 800\}, \\ L_4 &= \{275, 400, 475, 600, 675, 800\}. \end{aligned} \tag{4.22}$$

Figure 4.42 corresponds to a fit to interval L_1. It is found that for the values $\lambda = 0.1$ and above, as larger values of L are considered, the curves $\tau(q)$ approach $\tau(q) = 0$. This not only suggests a single fractal nature but also a localization of the bulk states in the thermodynamic limit for small values of disorder. It is known that for one dimensional systems all states are localized for any finite value of uncorrelated disorder. By taking k_x at a fixed value, we are also reducing the problem to an effective one dimension and this suggests that the states will become localized along the y direction for small values of disorder as the system size tends to infinity. With the simplification of studying the system at a fixed value of k_x we can only take conclusions about the nature of the states along the y direction in real space.

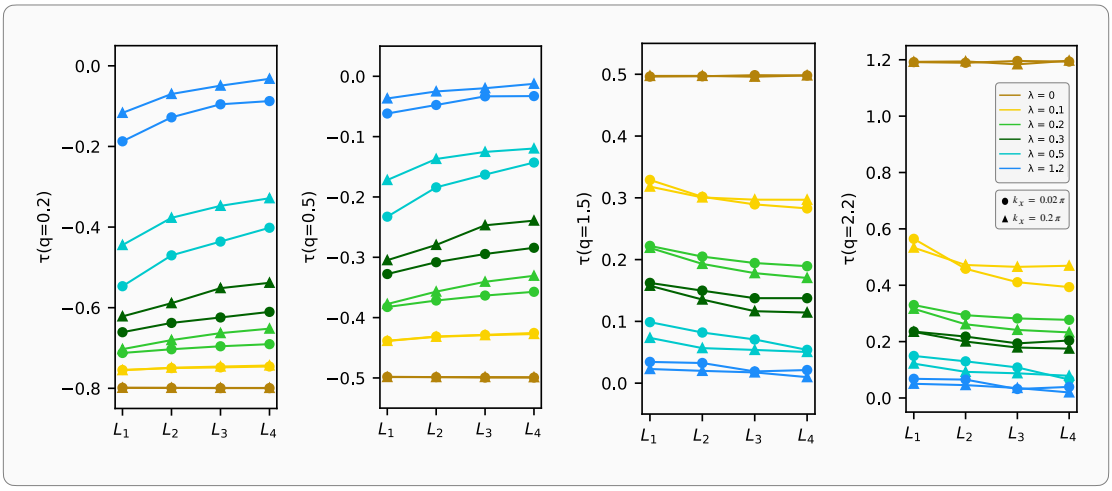

Figure 4.43: Values of τ at different values of q and disorder strength λ, for $k_x = 0.02\pi$ (●) and $k_x = 0.2\pi$ (▲). The IPR is averaged for the states within the energy range $E \in [0.05, 1]$.

In figure 4.43 several values of $\tau(q)$ are presented, for different values of disorder strength λ, obtained with fits of the IPR for the several values of the system size in 4.22. For $\lambda = 0$ the values of $\tau(q)$ follow the values of $q - 1$ for any interval of L. On the other hand, for finite values of disorder strength $\lambda \neq 0$, $\tau(q)$ tends to higher values if $q < 1$ and for lower values if $q > 1$ as the system size is increased, which is consistent with a single-fractal behaviour.

Aubry-André disorder

We take the same system sizes and intervals and the same fixed values of k_x and introduce Aubry-André quasi-periodic disorder. Figure 4.44 shows the values of $\tau(q)$ for $k_x = 0.02\pi$ and $k_x = 0.2\pi$, for several values of quasi-disorder strength λ for the size interval L_1. The results are obtained for states within the energy range $E \in [0.05, 1]$. Unlike the previous case with Anderson disorder we see that the results differ for each k_x, and that for some values of disorder strength $\tau(q)$ follows the line $q - 1$ closely until some value of q where the behaviour suddenly changes.

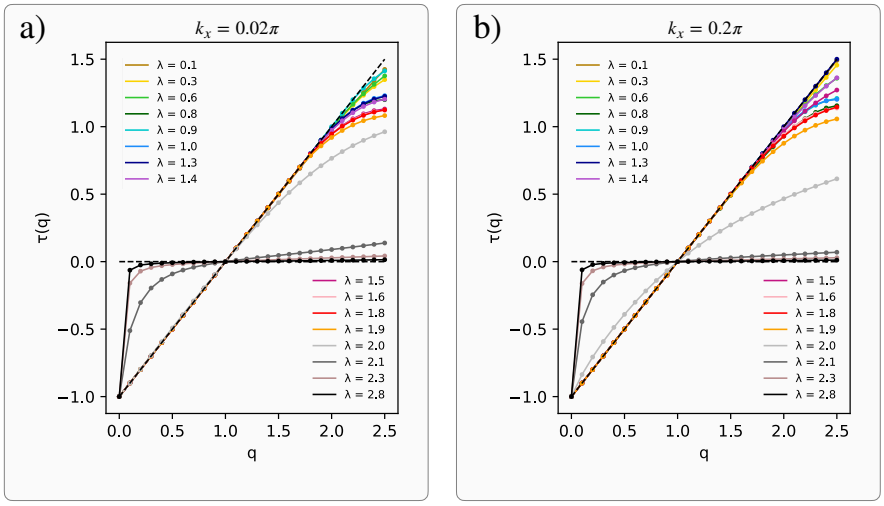

Figure 4.44: Results of τ vs. q, for several values of quasi-periodic disorder strength, λ, for a) $k_x = 0.02\pi$ and b) $k_x = 0.2\pi$. The IPR is averaged for the states within the energy range $E \in [0.05, 1]$.

Figure 4.45 shows the values of $\tau(q)$ fitted for the considered size intervals. It is seen that for lower values of q, τ remains at the values defined by the equation $\tau(q) = D(q)(q-1)$ with $D(q) = 1$. However, at higher values of q, this behaviour changes. Contrary to the case in 4.43, there is no clear tendency of $\tau(q)$ at increased system sizes, and the behaviour also depends on the value of q. This deviation from the $D(q) = 1$ line is verified as soon as disorder is introduced, and suggests the system is in a multifractal regime. From inspection of 4.44 and of the corresponding values of $\tau(q)$ at larger system sizes, we identify a transition to a single-fractal phase around $\lambda \in [2.0, 2, 1]$. Note that this does not coincide with the identified value of λ for the topological-trivial transition. Figure 4.46 illustrates the phases of the system. Examples of a) an extended, b) a critical, and c) a localized state, are shown. Note that between figures a), b) and c) the scale of the y axis changes by a factor of 10.

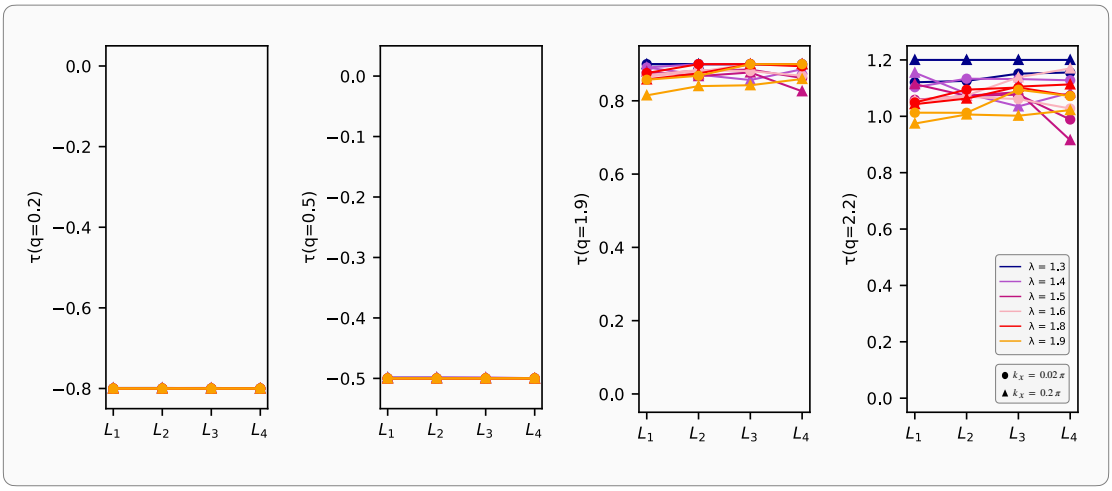

Figure 4.45: Values of τ at different values of q and disorder strength λ, for $k_x = 0.02\pi$ (●) and $k_x = 0.2\pi$ (▲). The IPR is averaged for the states within the energy range $E \in [0.05, 1]$.

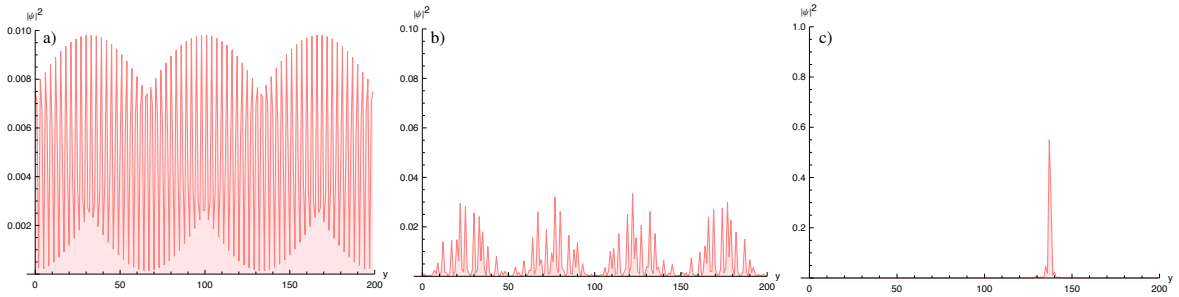

Figure 4.46: Example of wavefunctions on the different phases, at a fixed value $k_x = 0.02\pi$, for a system with 200 sites in y. a) Extended wavefunction at $E = 0.63$, $\lambda = 0$, b) critical wavefunction at $E = 0.67$, $\lambda = 1.6$, c) localized wavefunction at $E = 0.7$, $\lambda = 2.6$. Obtained for random values of ϕ in the quasi-periodic potential. Note that for each figure the scale of the y axis changes by a factor of 10.

5

Discussion, conclusions and future work

In this work we studied a model of a two-dimensional topological superconductor in the presence of a magnetic field. We introduced disorder and quasi-disorder in the system with the aim of studying the effects on topological and localization properties.

The system was first studied on a real space approach, and under a parallel magnetic field. We discussed the case where Anderson disorder is added to the edges, and then the case of Aubry-André edge disorder. For both cases, we obtained the result that the IPR of the bulk states remains nearly constant, and the system as a whole is essentially unaffected, while the edge states significantly localize. For the lowest energy states, the behaviour of the IPR as a function of λ is different for Anderson or Aubry-André edge disorder: in the first case, it grows continuously (meaning the states continuously localize) as disorder is increased; in the second case, we see a threshold behaviour where the states' IPR remains nearly constant until a certain value of λ, after which the IPR shows a significant increase. In both cases, we find that the lowest energy states for $B_y = 0.5d$ are more vulnerable to the edge disorder in the sense that the IPR shows a bigger increase compared with the other parameter sets considered. We also showed that the local edge disorder affects the modulation of the lowest energy wavefunctions on the bulk layers near the edges.

We then studied the cases of bulk disorder, with three different spatial configurations: Anderson disorder, Anderson disorder with x periodicity and Aubry-André disorder, modulated in the y direction and with x periodicity. In the first case (Anderson disorder), we found that the average IPR of the system increases with an exponential behaviour as a function of λ for $\lambda > 1.5$. We also observed that the IPR of the lowest energy states increases less than the average IPR of the system. From observation of the wavefunctions, we saw that the lowest energy states are removed from the edges and localize inside the bulk. In the second case (Anderson disorder with x periodicity), we found that the average IPR of the system differs greatly from the previously considered case, increasing linearly as a function of λ for $\lambda > 0.5$, and the behaviour of the lowest energy states' IPR shows no significant difference from that of the average IPR. The low energy states are removed from the edges for around $\lambda = 0.6$ and the states become increasingly localized in the y direction, remaining periodic in the x direction. For Aubry-André disorder, the behaviour of the average IPR of the system reveals the existence of two different regimes. In the fisrt the average IPR shows a slow increase with λ, and in the second the IPR greatly increases. The transition between two regimes is located around $\lambda = 2$. In this case, the edge states are robust to

the introduction of disorder, in the sense that they remain localized at or near the edges. For the case that was looked into with more detail, of $B_y = 0.5d$, we found that the edge states are removed around $\lambda = 1.8$, with an opening of the bulk gap. As disorder is increased, the states become sharply localized in the y direction. Also in this case, the bulk states present a critical-like behaviour in the y-direction, for intermediate values of disorder. For higher disorder values, $\lambda > 2$, the states become localized in the y-direction while still maintaining a periodic behaviour in the x direction. In any disorder case considered, we found that the average IPR behaves in the same way for $B_y = 0.5d$ or $B_y = 3.5d$ as a function of λ. For the case with $B_y = 4d$, with added spin-orbit coupling $\alpha = 0.2d$ and singlet s-wave pairing $\Delta_s = 0.3d$ the system has a different behaviour with a value of the average IPR which is consistently lower for all disorder cases.

The real space system was also studied under a perpendicular magnetic field B_z with introduced Anderson and Aubry-André disorder with periodicity in the x direction. We observed that the response of the topological phases of the system differ to the introduced types of disorder, and that quasi-disorder induces topological phases in new regions of B_z, characterized by integer values of the Chern number C. The critical points at these phase boundaries were shown to not change significantly as the system size increases, allowing us to conclude that the obtained phase diagrams should apply to bigger system sizes. Two of these new topological regimes were looked into with more detail, and they were found to be qualitatively different. Although both phases are characterized by a Chern number $C = -1$, one was found to show sharply localized edge states, while the other phase appears to lack a clear bulk-edge correspondence in the sense that the modes are not as sharply localized as expected, and have a finite contribution inside the bulk. However, the size of the system considered is a constraint that can not be neglected since the absence of sharply localized states can be a finite size effect. For some low values of magnetic field we also found that both x-periodic Anderson disorder and true completely random Anderson disorder induce some small regions of topology, in a region of magnetic field for which, in the clean system, the Chern number is zero and $I(k_y)$ is different from zero. In the same regions, new topological regions appear for added quasi-disorder. These observed phenomena were hypothesized to be related to the invariant $I(k_y)$. In the scope of this discussion we showed that the introduction of quasi-disorder does not remove the edge modes that in the clean system are protected by $I(k_y)$ when $C = 0$.

We also studied the system in a mixed (k_x, y) space with an applied parallel magnetic field. The clean superconducting system is known to possess flat bands in the gapless regime. At the corresponding values of k_x these have a winding number $\mathcal{W}$ of 1, which is defined from reducing the two dimensional system to an effective one dimension. We showed that these are also characterized by a π-quantized Berry phase at the same values of k_x. From the definition of winding number $\mathcal{W}$ we also obtained the expressions for the topological regions of the superconductor. These coincide with the gapless phases with Majorana flat bands.

We have shown that the introduction of quasi-disorder in the system induces gapless phases. For the p-wave system subject to a parallel magnetic field this leads to new regimes with Majorana flat bands. This is not only true for phases with a gapless bulk but also for gapped phases, where quasi-disorder

closes the bulk gap and Majorana flat bands appear. We then obtained the Berry phase with twisted boundary conditions and concluded that the quasi-disorder induced MFBs also have a quantized Berry phase of π. For the noncentrosymmetric superconductor with added s-wave superconducting pairing and Rashba spin orbit coupling, we found that new regimes with unidirectional Majorana edge states appear. In particular, we showed that for a phase where right-moving unidirectional edge states were present in the system, the introduction of quasi-disorder leads to the appearance of edge modes in the opposite moving direction, and for a certain quasi-disorder range these modes coexist in the system.

The identification of the quasi-disorder induced flat bands with a Berry phase with a quantized value of π allowed us to identify and study two topological transitions in detail, for the p-wave superconductor with a parallel applied magnetic field B_y. The two critical points were identified and studied by obtaining the density of induced Majorana bound states in relation to k_x points. We found that the values of the critical points show almost no variation with the system size for systems bigger than 76 sites in y. The values of the dynamical critical exponents and correlation length critical exponents were obtained as $z = 1.27 \pm 0.04$ and $\nu = 0.95 \pm 0.05$ for the first critical point $\lambda_{C,1} = 1.225$, and $z = 1.23 \pm 0.03$, $\nu = 1.00 \pm 0.05$ for the second critical point $\lambda_{C,2} = 1.805$, which puts this transition in a novel universality class. We then investigated the fractal nature of the wavefunctions by calculating the values of $\tau(q)$ from the IPR values at several values of disorder, at the same parameter values as those in which the topological transitions were studied. From the behaviour as the thermodynamic limit is approached, we concluded that the introduction of quasi-disorder induces multifractality in the system, and, accordingly, we see the appearance of critical states. A transition to a single-fractal regime was identified for $\lambda \in [2.0, 2.1]$. The same analysis was made for the system with Anderson disorder. The behaviour of $\tau(q)$ as the system size tends to infinity suggests that the introduction of Anderson disorder will drive the system to a localized, single-fractal phase (in the thermodynamic limit).

We remark that, recently, it was shown that multifractality can enhance not only the critical temperature but also the superconducting pairing amplitude [90]. The difference between isolated flat bands and flat bands with band touchings was also recently discussed [11] and it was shown that flat bands with band touchings greatly increase the critical temperature for superconductivity. Taking this into account and our results it is suggested that quasi-disorder can, in this case, surge as a possible way to enhance superconductivity and, with the appearance of flat bands with band touchings, contribute towards a higher value of the critical temperature.

Future work

Some interesting topics could be addressed in the future:

- When the real space system was studied, we considered the modulation of the quasi-periodic disorder potential in the y direction. Another idea could be to study a potential which is introduced at an angle in relation to the edges and study the localization properties as a function of such angle.

- As a complement to the study of the effects of quasi-disorder on the superconductor under a

perpendicular magnetic field, and to the obtained Chern numbers, it would be interesting to search for a real-space definition of the invariant $I(k_y)$. Defining $I(k_y)$ in real space, as with twisted boundary conditions, would allow us to understand if this invariant protects the edge states that remain when $C = 0$, as disorder is introduced.

- In the study of the system in a mixed (k_x, y) space, the clean and quasi-disorder induced flat bands were found to have a quantized Berry phase of π. A question that was raised is whether the flat bands in the disorder regime also have a quantized winding number of 1. A future task would then be to implement the winding number in a real space description following the methods described in [85–87].

- It would be interesting to study the transport properties of the edge states in the regimes where quasi-disorder induces MFBs, and also in the new regime with unidirectional edge states. For the flat bands that are induced by a magnetic field in the clean system, the ZBC was calculated and found to be quantized [8]. It would be interesting to see if this holds for the quasi-disorder induced MFBs, particularly since they share the topological properties with MFBs on the clean system. It would also be interesting to obtain the results for the ”flipped” Majorana edge states that appear with the increase of quasi-disorder, especially in the regime where we found unidirectional edge states in both directions in the system.

- Finally, we identified a quasi-disorder driven topological transition and obtained two critical points of λ. In reality there are two transition lines (λ, B_y), which would be interesting to obtain, as well as the critical exponents along these transition lines.

Bibliography

[1] C. Beenakker, "Search for Majorana Fermions in Superconductors", *Annual Review of Condensed Matter Physics* **2013**, *4*, 113–136.

[2] X.-L. Qi, S.-C. Zhang, "Topological insulators and superconductors", *Reviews of Modern Physics* **2011**, *83*, 1057–1110.

[3] M. Z. Hasan, C. L. Kane, "Topological Insulators", *Reviews of Modern Physics* **2010**, *82*, 3045–3067.

[4] M. Sato, Y. Ando, "Topological superconductors: a review", *Reports on Progress in Physics* **2017**, *80*, 076501.

[5] J. Alicea, "New directions in the pursuit of Majorana fermions in solid state systems", *Reports on Progress in Physics* **2012**, *75*, 076501.

[6] M. Sato, Y. Tanaka, K. Yada, T. Yokoyama, "Topology of Andreev bound states with flat dispersion", *Physical Review B* **2011**, *83*, 224511.

[7] Y. Tanaka, Y. Mizuno, T. Yokoyama, K. Yada, M. Sato, "Anomalous Andreev Bound State in Noncentrosymmetric Superconductors", *Physical Review Letters* **2010**, *105*, 097002.

[8] C. L. M. Wong, J. Liu, K. T. Law, P. A. Lee, "Majorana flat bands and unidirectional Majorana edge states in gapless topological superconductors", *Physical Review B* **2013**, *88*, DOI 10.1103/PhysRevB.88.060504.

[9] A. P. Schnyder, S. Ryu, "Topological phases and surface flat bands in superconductors without inversion symmetry", *Physical Review B* **2011**, *84*, 060504.

[10] A. P. Schnyder, P. M. R. Brydon, C. Timm, "Types of topological surface states in nodal noncentrosymmetric superconductors", *Physical Review B* **2012**, *85*, 024522.

[11] K.-E. Huhtinen, J. Herzog-Arbeitman, A. Chew, B. A. Bernevig, P. Törmä, "Revisiting flat band superconductivity: dependence on minimal quantum metric and band touchings", **2022**, DOI 10.48550/ARXIV.2203.11133.

[12] M. Sato, S. Fujimoto, "Majorana Fermions and Topology in Superconductors", *Journal of the Physical Society of Japan* **2016**, *85*, 072001.

[13] R. M. Lutchyn, J. D. Sau, S. Das Sarma, "Majorana Fermions and a Topological Phase Transition in Semiconductor-Superconductor Heterostructures", *Physical Review Letters*, *105*, DOI 10.1103/PhysRevLett.105.077001.

[14] V. Mourik, K. Zuo, S. M. Frolov, S. R. Plissard, E. P. A. M. Bakkers, L. P. Kouwenhoven, "Signatures of Majorana Fermions in Hybrid Superconductor-Semiconductor Nanowire Devices", *Science* **2012**, *336*, 1003–1007.

[15] S. Nadj-Perge, I. K. Drozdov, J. Li, H. Chen, S. Jeon, J. Seo, A. H. MacDonald, B. A. Bernevig, A. Yazdani, "Observation of Majorana fermions in ferromagnetic atomic chains on a superconductor", *Science* **2014**, *346*, 602–607.

[16] S. Aubry, G. André, "Analyticity breaking and Anderson localization in incommensurate lattices", *Ann. Israel Phys. Soc* **1980**, *3*, 18.

[17] F. Evers, A. D. Mirlin, "Anderson transitions", *Reviews of Modern Physics* **2008**, *80*, 1355–1417.

[18] D. R. Hofstadter, "Energy levels and wave functions of Bloch electrons in rational and irrational magnetic fields", *Physical Review B* **1976**, *14*, 2239–2249.

[19] M. Rossignolo, L. Dell'Anna, "Localization transitions and mobility edges in coupled Aubry-André chains", *Physical Review B* **2019**, *99*, 054211.

[20] B. Huang, W. V. Liu, "Moiré localization in two-dimensional quasiperiodic systems", *Physical Review B* **2019**, *100*, 144202.

[21] M. J. Park, H. S. Kim, S. Lee, "Emergent localization in dodecagonal bilayer quasicrystals", *Physical Review B*, *99*, DOI 10.1103/PhysRevB.99.245401.

[22] D. Mao, T. Senthil, "Quasiperiodicity, band topology, and moiré graphene", *Physical Review B* **2021**, *103*, DOI 10.1103/physrevb.103.115110.

[23] M. Gonçalves, H. Z. Olyaei, B. Amorim, R. Mondaini, P. Ribeiro, E. V. Castro, "Incommensurability-induced sub-ballistic narrow-band-states in twisted bilayer graphene", *2D Materials* **2021**, *9*, 011001.

[24] J. M. B. Lopes dos Santos, N. M. R. Peres, A. H. Castro Neto, "Graphene Bilayer with a Twist: Electronic Structure", *Physical Review Letters* **2007**, *99*, 256802.

[25] R. Bistritzer, A. H. MacDonald, "Moiré bands in twisted double-layer graphene", *Proceedings of the National Academy of Sciences* **2011**, *108*, 12233–12237.

[26] J. M. B. Lopes dos Santos, N. M. R. Peres, A. H. Castro Neto, "Continuum model of the twisted graphene bilayer", *Physical Review B* **2012**, *86*, 155449.

[27] V. Goblot, A. Štrkalj, N. Pernet, J. L. Lado, C. Dorow, A. Lemaître, L. L. Gratiet, A. Harouri, I. Sagnes, S. Ravets, et al., "Emergence of criticality through a cascade of delocalization transitions in quasiperiodic chains", *Nature Physics* **2020**, *16*, 832–836.

[28] J. H. Pixley, J. H. Wilson, D. A. Huse, S. Gopalakrishnan, "Weyl Semimetal to Metal Phase Transitions Driven by Quasiperiodic Potentials", *Physical Review Letters* **2018**, *120*, DOI 10.1103/physrevlett.120.207604.

[29] Y. E. Kraus, Y. Lahini, Z. Ringel, M. Verbin, O. Zilberberg, "Topological States and Adiabatic Pumping in Quasicrystals", *Phys. Rev. Lett.* **2012**, *109*, 106402.

[30] L.-J. Lang, X. Cai, S. Chen, "Edge States and Topological Phases in One-Dimensional Optical Superlattices", *Physical Review Letters* **2012**, *108*, 220401.

[31] Y. E. Kraus, Y. Lahini, Z. Ringel, M. Verbin, O. Zilberberg, "Topological States and Adiabatic Pumping in Quasicrystals", *Physical Review Letters* **2012**, *109*, 106402.

[32] Y. Fu, E. J. König, J. H. Wilson, Y.-Z. Chou, J. H. Pixley, "Magic-angle semimetals", *npj Quantum Materials* **2020**, *5*, 71.

[33] F. A. An, E. J. Meier, B. Gadway, "Engineering a Flux-Dependent Mobility Edge in Disordered Zigzag Chains", *Physical Review X* **2018**, *8*, 031045.

[34] G. Roati, C. D'Errico, L. Fallani, M. Fattori, C. Fort, M. Zaccanti, G. Modugno, M. Modugno, M. Inguscio, "Anderson localization of a non-interacting Bose–Einstein condensate", *Nature* **2008**, *453*, 895–898.

[35] L. Guidoni, C. Triché, P. Verkerk, G. Grynberg, "Quasiperiodic Optical Lattices", *Phys. Rev. Lett.* **1997**, *79*, 3363–3366.

[36] H. P. Lüschen, S. Scherg, T. Kohlert, M. Schreiber, P. Bordia, X. Li, S. Das Sarma, I. Bloch, "Single-Particle Mobility Edge in a One-Dimensional Quasiperiodic Optical Lattice", *Physical Review Letters* **2018**, *120*, 160404.

[37] Y. Lahini, R. Pugatch, F. Pozzi, M. Sorel, R. Morandotti, N. Davidson, Y. Silberberg, "Observation of a Localization Transition in Quasiperiodic Photonic Lattices", *Physical Review Letters* **2009**, *103*, 013901.

[38] J. Wang, X.-J. Liu, G. Xianlong, H. Hu, "Phase diagram of a non-Abelian Aubry-André-Harper model withp-wave superfluidity", *Physical Review B* **2016**, *93*, DOI 10.1103/physrevb.93.104504.

[39] J. Fraxanet, U. Bhattacharya, T. Grass, D. Rakshit, M. Lewenstein, A. Dauphin, "Topological properties of the long-range Kitaev chain with Aubry-André-Harper modulation", *Physical Review Research* **2021**, *3*, DOI 10.1103/physrevresearch.3.013148.

[40] X. Tong, Y.-M. Meng, X. Jiang, C. Lee, G. D. D. M. Neto, G. Xianlong, "Dynamics of a quantum phase transition in the Aubry-André-Harper model with p-wave superconductivity", *Physical Review B* **2021**, *103*, DOI 10.1103/physrevb.103.104202.

[41] T. Lv, T.-C. Yi, L. Li, G. Sun, W.-L. You, "Quantum criticality and universality in the p -wave-paired Aubry-André-Harper model", *Physical Review A* **2022**, *105*, 013315.

[42] W. DeGottardi, D. Sen, S. Vishveshwara, "Majorana Fermions in Superconducting 1D Systems Having Periodic, Quasiperiodic, and Disordered Potentials", *Physical Review Letters* **2013**, *110*, 146404.

[43] X. Cai, L.-J. Lang, S. Chen, Y. Wang, "Topological Superconductor to Anderson Localization Transition in One-Dimensional Incommensurate Lattices", *Physical Review Letters* **2013**, *110*, 176403.

[44] X. Cai, "Quantum phase transitions and phase diagram for a one-dimensional p-wave superconductor with an incommensurate potential", *Journal of Physics: Condensed Matter* **2014**, *26*, 155701.

[45] M. Tezuka, N. Kawakami, "Reentrant topological transitions in a quantum wire/superconductor system with quasiperiodic lattice modulation", *Physical Review B* **2012**, *85*, 140508.

[46] R. Queiroz, A. P. Schnyder, "Stability of flat-band edge states in topological superconductors without inversion center", *Physical Review B* **2014**, *89*, DOI 10.1103/physrevb.89.054501.

[47] T. Čadez, R. Mondaini, E. Castro, P. Sacramento, "Static and Dynamic Disorder in Topological Systems: Localized, Critical and Extended States", *Acta Physica Polonica A* **2019**, *135*, 1180–1190.

[48] A. P. Mackenzie, Y. Maeno, "The superconductivity of Sr_2RuO_4 and the physics of spin-triplet pairing", *Reviews of Modern Physics* **2003**, *75*, 657–712.

[49] R. Joynt, L. Taillefer, "The superconducting phases of UPt_3", *Reviews of Modern Physics* **2002**, *74*, 235–294.

[50] K. Matano, M. Kriener, K. Segawa, Y. Ando, G.-q. Zheng, "Spin-Rotation Symmetry Breaking in the Superconducting State of $Cu_xBi_2Se_3$", *Nature Physics* **2016**, *12*, 852–854.

[51] E. Bauer, G. Hilscher, H. Michor, C. Paul, E. W. Scheidt, A. Gribanov, Y. Seropegin, H. Noël, M. Sigrist, P. Rogl, "Heavy Fermion Superconductivity and Magnetic Order in Noncentrosymmetric $CePt_3Si$", *Physical Review Letters* **2004**, *92*, 027003.

[52] I. Sugitani, Y. Okuda, H. Shishido, T. Yamada, A. Thamizhavel, E. Yamamoto, T. D. Matsuda, Y. Haga, T. Takeuchi, R. Settai, Y. Ōnuki, "Pressure-Induced Heavy-Fermion Superconductivity in Antiferromagnet $CeIrSi_3$ without Inversion Symmetry", *Journal of the Physical Society of Japan* **2006**, *75*, 043703.

[53] N. Kimura, K. Ito, K. Saitoh, Y. Umeda, H. Aoki, T. Terashima, "Pressure-Induced Superconductivity in Noncentrosymmetric Heavy-Fermion $CeRhSi_3$", *Physical Review Letters* **2005**, *95*, 247004.

[54] P. A. Frigeri, D. F. Agterberg, A. Koga, M. Sigrist, "Superconductivity without Inversion Symmetry: MnSi versus $CePt_3Si$", *Physical Review Letters* **2004**, *92*, 097001.

[55] S. Fujimoto, "Electron Correlation and Pairing States in Superconductors without Inversion Symmetry", *Journal of the Physical Society of Japan* **2007**, *76*, 051008.

[56] M. Sato, S. Fujimoto, "Topological phases of noncentrosymmetric superconductors: Edge states, Majorana fermions, and non-Abelian statistics", *Physical Review B* **2009**, *79*, DOI 10.1103/PhysRevB.79.094504.

[57] M. Berry, "Quantal phase factors accompanying adiabatic changes", *Proceedings of the Royal Society of London. A. Mathematical and Physical Sciences* **1984**, *392*, 45–57.

[58] W. A. Benalcazar, B. A. Bernevig, T. L. Hughes, "Electric multipole moments, topological multipole moment pumping, and chiral hinge states in crystalline insulators", *Physical Review B* **2017**, *96*, DOI 10.1103/physrevb.96.245115.

[59] D. J. Thouless, M. Kohmoto, M. P. Nightingale, M. den Nijs, "Quantized Hall Conductance in a Two-Dimensional Periodic Potential", *Physical Review Letters* **1982**, *49*, 405–408.

[60] K. v. Klitzing, G. Dorda, M. Pepper, “New Method for High-Accuracy Determination of the Fine-Structure Constant Based on Quantized Hall Resistance”, *Physical Review Letters* **1980**, *45*, 494–497.

[61] M. A. N. Araújo, P. D. Sacramento, *Topologia em Matéria Condensada: Uma Introdução*, 1st ed., IST Press, **2020**.

[62] M. A. N. Araújo, P. D. Sacramento, *Topology in condensed matter: an introduction*, World Scientific, **2021**.

[63] R. S. K. Mong, V. Shivamoggi, “Edge states and the bulk-boundary correspondence in Dirac Hamiltonians”, *Physical Review B* **2011**, *83*, DOI 10.1103/physrevb.83.125109.

[64] W. P. Su, J. R. Schrieffer, A. J. Heeger, “Solitons in Polyacetylene”, *Physical Review Letters* **1979**, *42*, 1698–1701.

[65] J. K. Asbóth, L. Oroszlány, A. Pályi, “A Short Course on Topological Insulators”, *Lecture Notes in Physics* **2016**, DOI 10.1007/978-3-319-25607-8.

[66] H. Onnes, “The Resistance of Pure Mercury at Helium Temperatures”, *Communications of the Physical Laboratory of the University of Leiden* **1911**.

[67] V. Ginzburg, L. Landau, “On the Theory of superconductivity”, *Zh. Eksp. Teor. Fiz.* **1950**, *20*, 1064–1082.

[68] J. Bardeen, L. N. Cooper, J. R. Schrieffer, “Theory of Superconductivity”, *Phys. Rev.* **1957**, *108*, 1175–1204.

[69] P.-G. d. Gennes, *Superconductivity of metals and alloys*, Advanced Book Program, Perseus Books, **1999**.

[70] M. Sigrist, K. Ueda, “Phenomenological theory of unconventional superconductivity”, *Reviews of Modern Physics* **1991**, *63*, 239–311.

[71] A. Y. Kitaev, “Unpaired Majorana fermions in quantum wires”, *Physics-Uspekhi* **2001**, *44*, 131–136.

[72] M. Leijnse, K. Flensberg, “Introduction to topological superconductivity and Majorana fermions”, *Semiconductor Science and Technology* **2012**, *27*, 124003.

[73] D. Thouless, “Electrons in disordered systems and the theory of localization”, *Physics Reports* **1974**, *13*, 93–142.

[74] P. W. Anderson, “Absence of Diffusion in Certain Random Lattices”, *Phys. Rev.* **1958**, *109*, 1492–1505.

[75] A. Altland, M. R. Zirnbauer, “Nonstandard symmetry classes in mesoscopic normal-superconducting hybrid structures”, *Phys. Rev. B* **1997**, *55*, 1142–1161.

[76] F. Wegner, “Inverse participation ratio in $2+\varepsilon$ dimensions”, *Zeitschrift für Physik B Condensed Matter and Quanta* **1980**, *36*, 209–214.

[77] M. Janssen, "Multifractal Analysis Of Broadly-Distributed Observables At Criticality", *International Journal of Modern Physics B* **1994**, *08*, 943–984.

[78] K. Kobayashi, T. Ohtsuki, K.-I. Imura, I. F. Herbut, "Density of States Scaling at the Semimetal to Metal Transition in Three Dimensional Topological Insulators", *Physical Review Letters* **2014**, *112*, DOI 10.1103/physrevlett.112.016402.

[79] M. Gonçalves, P. Ribeiro, E. V. Castro, M. A. N. Araújo, "Disorder-Driven Multifractality Transition in Weyl Nodal Loops", *Physical Review Letters* **2020**, *124*, DOI 10.1103/physrevlett.124.136405.

[80] S. Sachdev, *Quantum phase transitions*, Second edition, Cambridge University Press, Cambridge ; New York, **2011**.

[81] P. D. Sacramento, "Fate of Majorana fermions and Chern numbers after a quantum quench", *Physical Review E* **2014**, *90*, DOI 10.1103/physreve.90.032138.

[82] X. Wen, A. Zee, "Winding number, family index theorem, and electron hopping in a magnetic field", *Nuclear Physics B* **1989**, *316*, 641–662.

[83] H.-X. Wang, G.-Y. Guo, J.-H. Jiang, "Band topology in classical waves: Wilson-loop approach to topological numbers and fragile topology", *New Journal of Physics* **2019**, *21*, 093029.

[84] A. Mildenberger, F. Evers, A. D. Mirlin, J. T. Chalker, "Density of quasiparticle states for a two-dimensional disordered system: Metallic, insulating, and critical behavior in the class-D thermal quantum Hall effect", *Physical Review B* **2007**, *75*, 245321.

[85] I. Mondragon-Shem, T. L. Hughes, J. Song, E. Prodan, "Topological Criticality in the Chiral-Symmetric AIII Class at Strong Disorder", *Physical Review Letters* **2014**, *113*, DOI 10.1103/physrevlett.113.046802.

[86] J. Song, E. Prodan, "AIII and BDI topological systems at strong disorder", *Physical Review B* **2014**, *89*, DOI 10.1103/physrevb.89.224203.

[87] L. Lin, Y. Ke, C. Lee, "Real-space representation of the winding number for a one-dimensional chiral-symmetric topological insulator", *Physical Review B* **2021**, *103*, DOI 10.1103/physrevb.103.224208.

[88] N. Sedlmayr, J. M. Aguiar-Hualde, C. Bena, "Flat Majorana bands in two-dimensional lattices with inhomogeneous magnetic fields: Topology and stability", *Physical Review B* **2015**, *91*, DOI 10.1103/physrevb.91.115415.

[89] J. C. C. Cestari, A. Foerster, M. A. Gusmão, M. Continentino, "Critical exponents of the disorder-driven superfluid-insulator transition in one-dimensional Bose-Einstein condensates", *Physical Review A* **2011**, *84*, DOI 10.1103/PhysRevA.84.055601.

[90] X. Zhang, M. S. Foster, "Enhanced Amplitude for Superconductivity due to Spectrum-wide Wave Function Criticality in Quasiperiodic and Power-law Random Hopping Models", *arXiv:2204.02996 [cond-mat]* **2022**.

[91] A. P. Schnyder, S. Ryu, A. Furusaki, A. W. W. Ludwig, "Classification of topological insulators and superconductors in three spatial dimensions", *Physical Review B* **2008**, *78*, DOI 10.1103/physrevb.78.195125.

[92] S. Ryu, A. P. Schnyder, A. Furusaki, A. W. W. Ludwig, "Topological insulators and superconductors: tenfold way and dimensional hierarchy", *New Journal of Physics* **2010**, *12*, 065010.

[93] R. Haydock, "The recursive solution of the Schrödinger equation", *Computer Physics Communications* **1980**, *20*, 11–16.

[94] C. Lanczos, "An iteration method for the solution of the eigenvalue problem of linear differential and integral operators", *Journal of Research of the National Bureau of Standards* **1950**, *45*, 255.

[95] "Density of states extracted from modified recursion relations", *Physics Letters A* **2007**, *367*, 162–172.

[96] A. Alhaidari, "Density of states engineering: normalized energy density of states band structure using the tridiagonal representation approach", *Canadian Journal of Physics* **2018**, *96*, 275–286.

[97] M. Gonçalves, MA thesis, Instituto Superior Técnico, **2018**.

[98] Y.-F. Zhang, Y.-Y. Yang, Y. Ju, L. Sheng, R. Shen, D.-N. Sheng, D.-Y. Xing, "Coupling-matrix approach to the Chern number calculation in disordered systems", *Chinese Physics B* **2013**, *22*, 117312.

[99] *Advanced Topological Insulators*, 1st ed., (Ed.: H. Luo), Wiley, **2019**.

[100] J. Wang, S.-C. Zhang, "Topological states of condensed matter", *Nature Materials* **2017**, *16*, 1062–1067.

[101] A. Y. Kitaev, "Unpaired Majorana fermions in quantum wires", *Physics-Uspekhi* **2001**, *44*, 131–136.

[102] S. Fujimoto, "Electron Correlation and Pairing States in Superconductors without Inversion Symmetry", *Journal of the Physical Society of Japan* **2007**, *76*, 051008.

[103] Y. Tanaka, M. Sato, N. Nagaosa, "Symmetry and Topology in Superconductors –Odd-Frequency Pairing and Edge States", *Journal of the Physical Society of Japan* **2012**, *81*, 011013.

[104] M. Sato, S. Fujimoto, "Majorana Fermions and Topology in Superconductors", *Journal of the Physical Society of Japan* **2016**, *85*, 072001.

[105] R. Haydock, "The Recursive Solution of the Schrodinger Equation", *Solid State Physics* **1980**, 215–294.

[106] N. Sedlmayr, J. M. Aguiar-Hualde, C. Bena, "Flat Majorana bands in two-dimensional lattices with inhomogeneous magnetic fields: Topology and stability", *Physical Review B* **2015**, *91*, DOI 10.1103/physrevb.91.115415.

[107] H. Guo, S.-Q. Shen, S. Feng, "Fractional topological phase in one-dimensional flat bands with nontrivial topology", *Physical Review B* **2012**, *86*, DOI 10.1103/physrevb.86.085124.

[108] H. Guo, S.-Q. Shen, "Topological phase in a one-dimensional interacting fermion system", *Physical Review B* **2011**, *84*, DOI 10.1103/physrevb.84.195107.

[109] W. C. Yu, Y. C. Li, P. D. Sacramento, H.-Q. Lin, "Reduced density matrix and order parameters of a topological insulator", *Physical Review B* **2016**, *94*, DOI 10.1103/physrevb.94.245123.

[110] J. H. Pixley, J. H. Wilson, D. A. Huse, S. Gopalakrishnan, "Weyl Semimetal to Metal Phase Transitions Driven by Quasiperiodic Potentials", *Phys. Rev. Lett.* **2018**, *120*, 207604.

A

Symmetry Classification of Topological Systems

The topological symmetry classification of one, two and three-dimensional systems with respect to time-reversal symmetry, particle hole symmetry and chiral symmetry is presented [91, 92]. This classification determines whether the system possesses a topological invariant, and the type of topological invariant, which can be an integer ($\mathbb{Z}$) or a $\mathbb{Z}_2$ quantity. For the corresponding operators $\mathcal{T}$, $\mathcal{P}$ and $\mathcal{S}$, for a Hamiltonian $\mathcal{H}(\mathbf{k})$ defined in momentum space, the symmetries are such that the following relations are satisfied:

- Time-reversal Symmetry (TRS)

$$\mathcal{T}\mathcal{H}^*(-\mathbf{k})\mathcal{T}^\dagger = \mathcal{H}(\mathbf{k}) \tag{A.1}$$

- Particle Hole Symmetry (PHS)

$$\mathcal{P}\mathcal{H}(\mathbf{k})\mathcal{P}^\dagger = -\mathcal{H}^*(-\mathbf{k}) \tag{A.2}$$

- Chiral Symmetry (CS)

$$\mathcal{S}\mathcal{H}(\mathbf{k})\mathcal{S}^\dagger = -\mathcal{H}(\mathbf{k}) \tag{A.3}$$

		TRS	PHS	CS	$d=1$	$d=2$	$d=3$
Standard	A (unitary)	0	0	0	$-$	$\mathbb{Z}$	$-$
(Wigner-Dyson)	AI (orthogonal)	$+1$	0	0	$-$	$-$	$-$
	AII (symplectic)	-1	0	0	$-$	$\mathbb{Z}_2$	$\mathbb{Z}_2$
Chiral	AIII (chiral unitary)	0	0	1	$\mathbb{Z}$	$-$	$\mathbb{Z}$
(sublattice)	BDI (chiral orthogonal)	$+1$	$+1$	1	$\mathbb{Z}$	$-$	$-$
	CII (chiral symplectic)	-1	-1	1	$\mathbb{Z}$	$-$	$\mathbb{Z}_2$
BdG	D	0	$+1$	0	$\mathbb{Z}_2$	$\mathbb{Z}$	$-$
	C	0	-1	0	$-$	$\mathbb{Z}$	$-$
	DIII	-1	$+1$	1	$\mathbb{Z}_2$	$\mathbb{Z}_2$	$\mathbb{Z}$
	CI	$+1$	-1	1	$-$	$-$	$\mathbb{Z}$

Table A.1: The symmetry classes of single particle Hamiltonians, in terms of time reversal-symmetry, particle-hole symmetry, chiral symmetry, and number of dimensions. The presence of symmetry is denoted by "+1" or "-1" depending on whether the symmetry operator squares to +1 or -1. "0" denotes the absence of symmetry. The last three columns indicate the type of topological invariant that characterizes the system with regards to the dimension d. Table taken from [91].

B

Numerical Methods

B.1 Recursive Green's Function

The Recursive Green's Function (RGF) method allows the calculation of the density of states (DOS) of the system in a way that is more computationally efficient than the direct calculation from the exact diagonalization of the Hamiltonian. The method was first developed by Haydock [93], based on the Lanczos method [94]. The idea is to construct a basis which tridiagonalizes an Hamiltonian $\mathcal{H}$, and then use a continued fraction expansion to compute the Green's function, and then the density of states [95].

To construct the tridiagonal basis, we go through an iteractive procedure:

- We start with an initial normalized state $|\psi_1\rangle$ for which we will obtain the local density of states (LDOS).
  - Compute a_1 as $a_1 = \langle\psi_1|\mathcal{H}|\psi_1\rangle$.
  - Define a new state $|\tilde{\psi}_2\rangle$, orthogonal to $|\psi_1\rangle$, as $|\tilde{\psi}_2\rangle = \mathcal{H}\,|\psi_1\rangle - a_1\,|\psi_1\rangle$.
  - Obtain the norm of $|\tilde{\psi}_2\rangle$, $b_1 = \sqrt{\langle\tilde{\psi}_2 \mid \tilde{\psi}_2\rangle}$ and normalize the state, $|\psi_2\rangle = \frac{1}{b_1}|\tilde{\psi}_2\rangle$.
- All the other iteractive steps are identical and can be summarized as:

$$\begin{aligned} a_n &= \langle\psi_n|\hat{\mathcal{H}}|\psi_n\rangle \\ |\tilde{\psi}_{n+1}\rangle &= \hat{\mathcal{H}}|\psi_n\rangle - a_n|\psi_n\rangle - b_{n-1}|\psi_{n-1}\rangle \\ b_n &= \sqrt{\langle\tilde{\psi}_{n+1} \mid \tilde{\psi}_{n+1}\rangle} \\ |\psi_{n+1}\rangle &= \frac{1}{b_n}|\tilde{\psi}_{n+1}\rangle \end{aligned} \tag{B.1}$$

After N steps, we obtain the tridiagonal basis $\{|\,\psi_1\rangle\ |\,\psi_2\rangle ...,|\,\psi_N\rangle\}$ and the sets of coefficients $\{a_n\}$ and $\{b_n\}$ which are, respectively, the diagonal and off-diagonal elements of the Hamiltonian representation $\tilde{\mathcal{H}}$ in the new basis, which has a size $N \times N$.

The Green's function is obtained as

$$G(E) = (E - \mathcal{H})^{-1} \tag{B.2}$$

and in terms of the Hamiltonian $\tilde{\mathcal{H}}$ in the new tridiagonal basis, we can write

$$\tilde{G}(E) = (E - \tilde{\mathcal{H}})^{-1} = \begin{pmatrix} E - a_1 & -b_1 & & & \\ -b_1 & E - a_2 & -b_2 & & \\ & -b_2 & \ddots & \ddots & \\ & & \ddots & \ddots & -b_{N-1} \\ & & & -b_{N-1} & E - a_N \end{pmatrix}^{-1}. \tag{B.3}$$

We can now obtain $\langle \psi_1 | \tilde{G}(E) | \psi_1 \rangle \equiv \tilde{G}_1(E)$, which defines the Green's function for the initial state $|\psi_1\rangle$. From equation B.3 we obtain a continued fraction representation

$$\tilde{G}_1(E) = \cfrac{1}{E - a_1 - \cfrac{b_1^2}{E - a_2 - \cfrac{b_2^2}{E - a_3 - \cdots \cfrac{b_{N-1}^2}{E - a_N}}}}. \tag{B.4}$$

It should be verified that as $N \to \infty$, $\tilde{G}_1(E)$ tends to the real solution for $G_1(E)$. However, performing an exceedingly large number of iterations is not practical. Also, it is verified that the values of a_n and b_n converge relatively quickly to asymptotic values. This allows us to introduce a cutoff, a terminator ($T(E)$), to compute B.4:

$$\tilde{G}_1(E) = \cfrac{1}{E - a_1 - \cfrac{b_1^2}{E - a_2 - \cfrac{b_2^2}{E - a_3 - \cdots \cfrac{b_{N-1}^2}{E - a_N - T(E)}}}}. \tag{B.5}$$

The correct form of $T(E)$ depends on the band structure of the system [96]. For the case of one energy density band, where a_n and b_n converge to the values a_∞ and b_∞, the terminator obeys

$$T(E) = \frac{b_\infty^2}{E - a_\infty - T(E)}. \tag{B.6}$$

Keeping only the solution for which $T(E)$ tends to zero as $E \to \infty$, we obtain for $T(E)$:

$$T(E) = \frac{(E - a_\infty) - \sqrt{(E - a_\infty)^2 - 4b_\infty^2}}{2}. \tag{B.7}$$

This corresponds to a density of states for a single band with boundaries at $E = a_\infty \pm 2b_\infty$. The shape of the band will depend on the form of the recursion coefficients $\{a_n\}$ and $\{b_n\}$.

If the case is such that the system has two energy bands and a gap, the recursion coefficients will converge to two sets of alternate values, $a_{1,\infty}$, $a_{2,\infty}$ and $b_{1,\infty}$, $b_{2,\infty}$. The terminator will then obey:

$$T(E) = b_{1,\infty}^2 \left[E - a_{1,\infty} - \frac{b_{2,\infty}^2}{E - a_{2,\infty} - T(E)} \right]^{-1}, \tag{B.8}$$

which gives

$$T(E) = \frac{(E - a_{1,\infty})(E - a_{2,\infty}) + b_{1,\infty}^2 - b_{2,\infty}^2}{2(E - a_{1,\infty})} - \sqrt{\left[\frac{(E - a_{1,\infty})(E - a_{2,\infty}) + b_{1,\infty}^2 - b_{2,\infty}^2}{2(E - a_{1,\infty})}\right]^2 - b_{1,\infty}^2 \frac{(E - a_{2,\infty})}{(E - a_{1,\infty})}}. \tag{B.9}$$

After writing the Hamiltonian in a tridiagonal basis and computing the Green's function, we want to obtain the density of states. The density of states projected on state $|\mathbf{r}\rangle$ (local density of states, LDOS, on site $\mathbf{r}$) of the local site basis is given by

$$\rho_{\mathbf{r}}(E) = \sum_m |\langle \psi_m \mid \mathbf{r} \rangle|^2 \delta\left(E - E_m\right), \tag{B.10}$$

where the sum goes over all eigenstates $|\psi_m\rangle$ of the system with corresponding eigenvalues E_m. The projected density of states is related to the Green's function by

$$\rho_{\mathbf{r}}(E) = -\frac{1}{\pi} \lim_{\eta \to 0} \left[\mathrm{Im} \left\langle \mathbf{r} \left| \frac{1}{E + i\eta - \mathcal{H}} \right| \mathbf{r} \right\rangle \right] = \frac{1}{\pi} \lim_{\eta \to 0} \left[\mathrm{Im}\, G_{\mathbf{r}}(E + i\eta) \right] = \frac{1}{\pi} G_{\mathbf{r}}^R(E) \tag{B.11}$$

with $G_{\mathbf{r}}(E) \equiv \langle \mathbf{r}|G(E)|\mathbf{r}\rangle$ and where $G_{\mathbf{r}}^R(E)$ is the retarded Green's function.

The total density of states (DOS) can be obtained by summing and averaging over all the projected density of states on all sites of the system,

$$\rho(E) = \frac{1}{N} \sum_{\mathbf{r}=1}^{N} \rho_{\mathbf{r}}(E). \tag{B.12}$$

In translational invariant systems, it is sufficient to compute the LDOS. However, if this is not the case, summing over all local sites as in equation B.12 can be time-consuming and thus an alternative is needed. A solution is to create a state $|\phi\rangle$ which is a linear combination of all the local states $|\mathbf{r}\rangle$, where each has a random contribution $\phi_{\mathbf{r}}$:

$$|\Phi\rangle = \sum_{\mathbf{r}} \phi_{\mathbf{r}} |\mathbf{r}\rangle. \tag{B.13}$$

The values of $\phi_{\mathbf{r}}$ are assumed to be real and are constrained so that the state $|\Phi\rangle$ is normalized. The density of states can then be obtained by going through the iteractive procedure for several random initial states $|\Phi\rangle$ which correspond to different sets of random variables $\{\phi_{\mathbf{r}}\}$ [97]. This approach is particularly useful for disordered systems.

B.2 Chern Number in real space

When disorder is introduced in a system, since the translational invariance is broken, it is not possible to perform calculations in momentum space (a direct transformation between real and reciprocal space no longer exists). In this case, we need to use twisted boundary conditions in real space [97–99]:

$$\psi_n^{\boldsymbol{\theta}}(\mathbf{r} + N_i \mathbf{a}_i) = \mathrm{e}^{\mathrm{i}\theta_i} \psi_n^{\boldsymbol{\theta}}(\mathbf{r}) \tag{B.14}$$

where $\boldsymbol{\theta} = (\theta_1, \theta_2)$ defines the space of twists and each component θ_i takes values between 0 and 2π, the vectors $\mathbf{a}_i$ are the basis vectors of the lattice, and $\psi_n^{\boldsymbol{\theta}}(\mathbf{r}) = \langle \mathbf{r} | \psi_n^{\boldsymbol{\theta}} \rangle$.

To perform the calculation we must use the ground-state wavefunction of the many body system, $| \Psi^{\theta} \rangle$, which is given by the Slater determinant of the single particle wavefunctions $| \psi_n^{\boldsymbol{\theta}} \rangle$ on M occupied states:

$$| \Psi^{\theta} \rangle = \prod_{n=1}^{M} c_n^{\dagger} |0\rangle = \prod_{n=1}^{M} | \psi_n^{\boldsymbol{\theta}} \rangle. \tag{B.15}$$

Noting that we can write the single-particle wavefunctions $| \psi_n^{\boldsymbol{\theta}} \rangle$ as an expansion in terms of the basis $| \mathbf{r}_i \rangle$ as $| \psi_n^{\boldsymbol{\theta}} \rangle = \sum_{\mathbf{r}_i} \varphi_{r_i}^{n,\theta} | \mathbf{r}_i \rangle$, we can represent the ground state wavefunction as a matrix $\boldsymbol{\Phi}_{\theta}$ of the expansion coefficients:

$$\boldsymbol{\Phi}_{\theta} = \begin{pmatrix} \varphi_{\mathrm{r}_1}^{1,\theta} & \varphi_{\mathrm{r}}^{2,\theta} & \cdots & \varphi_{\mathrm{r}}^{\mathrm{M},\theta} \\ \varphi_{\mathrm{r}_2}^{1,\theta} & \varphi_{\mathrm{r}_2}^{2,\theta} & \cdots & \varphi_{\mathrm{r}}^{\mathrm{M},\theta} \\ \vdots & \vdots & & \vdots \\ \varphi_{\mathrm{r}_N}^{1,\theta} & \varphi_{\mathrm{r}_N}^{2,\theta} & \cdots & \varphi_{\mathrm{r}_N}^{\mathrm{M},\theta} \end{pmatrix} \tag{B.16}$$

with $N = N_1 \times N_2$ the total number of sites.

We can then write the Berry connection in the space of twists as

$$\boldsymbol{\mathcal{A}}_{\boldsymbol{n}}(\theta) = i \left\langle \Psi^{\theta} \mid \boldsymbol{\partial}_{\theta} \Psi^{\theta} \right\rangle. \tag{B.17}$$

The integral in equation 2.8 is now taken in a surface S in the space of twists where the variables θ_1 and θ_2 are discretized into L_1 and L_2 points, such that they are constrained to take the values $\theta_i = \frac{2\pi}{L_i} n$, with n an integer that goes from 1 to L_i. Equation B.17 can be simplified if we consider the sum of the flux of individual plaquettes on the surface S with $L = L_1 \times L_2$ points. In this case, the Chern number becomes

$$C = \frac{1}{2\pi} \sum_{l=1}^{L} \arg\left(\left\langle \Psi^{\theta_l} \mid \Psi^{\theta_l + \mathbf{1}} \right\rangle \left\langle \Psi^{\theta_l + \mathbf{1}} \mid \Psi^{\theta_l + \mathbf{1} + \mathbf{2}} \right\rangle \left\langle \Psi^{\theta_l + \mathbf{1} + \mathbf{2}} \mid \Psi^{\theta_l + \mathbf{2}} \right\rangle \left\langle \Psi^{\theta_l + \mathbf{2}} \mid \Psi^{\theta_l} \right\rangle \right) \tag{B.18}$$

and the overlap between two states $| \Psi^{\theta} \rangle$ and $| \Psi^{\theta'} \rangle$ with different values θ and θ' of the twist variable is given by:

$$\langle \Psi^{\theta} \mid \Psi^{\theta'} \rangle = \det[\boldsymbol{\Phi}_{\theta}^{\dagger} \boldsymbol{\Phi}_{\theta'}]. \tag{B.19}$$

It is then possible to rewrite equation B.18 in its final form:

$$C = \frac{1}{2\pi} \sum_{l=1}^{L} \arg(\lambda_l) \tag{B.20}$$

where $\{\lambda_l\}$ are the eigenvalues of the matrix product

$$\prod_{l=1}^{L} \mathbf{\Phi}^{\dagger}_{\theta_l} \mathbf{\Phi}_{\theta_l+\mathbf{1}} \mathbf{\Phi}^{\dagger}_{\theta_l+\mathbf{1}} \mathbf{\Phi}_{\theta_l+\mathbf{1}+\mathbf{2}} \mathbf{\Phi}^{\dagger}_{\theta_l+\mathbf{1}+\mathbf{2}} \mathbf{\Phi}_{\theta_l+\mathbf{2}} \mathbf{\Phi}^{\dagger}_{\theta_l+\mathbf{2}} \mathbf{\Phi}_{\theta_l}. \tag{B.21}$$

This procedure is useful but time consuming, since it is necessary to perform the diagonalization of the Hamiltonian L times, one for each value of the periodic boundary conditions. It was shown [98] that the method can be simplified further, and it is only required to perform one diagonalization of the Hamiltonian with periodic boundary conditions.

The Chern number can then be calculated in the same way as in equation B.20, but the eigenvalues are obtained from the diagonalization of the matrix (with dimensions $M \times M$):

$$F = C_{\mathbf{q_0}\mathbf{q_1}} C_{\mathbf{q_1}\mathbf{q_2}} C_{\mathbf{q_2}\mathbf{q_3}} C_{\mathbf{q_3}\mathbf{q_0}} \tag{B.22}$$

where $\mathbf{q_0}$, $\mathbf{q_1}$, $\mathbf{q_2}$ and $\mathbf{q_3}$ define the corners of a plaquette in momentum space,

$$\mathbf{q_0} = (0,0), \mathbf{q_1} = (2\pi/N_1, 0), \mathbf{q_2} = (0, 2\pi/N_2), \mathbf{q_3} = (2\pi/N_1, 2\pi/N_2) \tag{B.23}$$

and the matrices $C_{\mathbf{q}\mathbf{q}'}$ are given by

$$C^{mn}_{\boldsymbol{q},\boldsymbol{q}'} = \sum_{\boldsymbol{r}_i} \left(\phi^{m,\theta=0}_{\boldsymbol{r}_i}\right)^* e^{i\left(\boldsymbol{q}-\boldsymbol{q}'\right)\cdot \boldsymbol{r}_i} \phi^{n,\theta=0}_{\boldsymbol{r}_i} \tag{B.24}$$

with $\{\phi^{\theta=0}_{\boldsymbol{r}}\}$ the set of eigenvectors obtained from the diagonalization of the Hamiltonian with periodic boundary conditions ($\boldsymbol{\theta} = 0$) in real space.

C

Evolution of energy spectra with a quasi-periodic potential

A more detailed evolution of the obtained energy spectra discussed in chapter 4 with Aubry-André disorder is presented, as well as more examples. The figures are presented for sequential values of λ where λ is the strength of the quasi-periodic potential defined as $\Lambda(y) = \lambda\cos(2\pi\alpha y + \phi)$, with α the inverse golden ratio. Here we take $\phi = 0$.

The cases shown in figure 4.30 a)-d) correspond, respectively, to figures C.2, C.3, C.5 and C.6. Figures C.1 and C.4 are not discussed previously in the thesis but also concern the parameter values $t = 1$, $d = t/6$, $\mu = 3d - 4t$, as in the main considered cases. In figure C.1 the system has no magnetic field, and the bulk gap does not close as disorder is increased. In figure C.4 the system has an added magnetic field in the y direction of $B_y = 3d$.

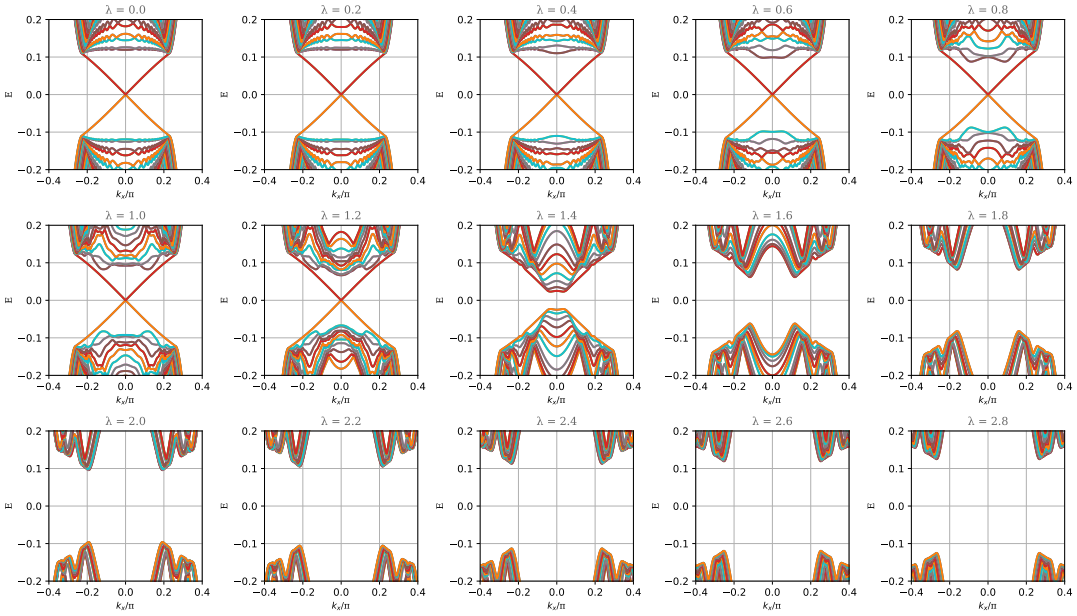

Figure C.1: Energy spectrum evolution for a system with 76 sites in y and edges at $y = 0$ and $y = 75$ for different values of λ as a function of k_x, for $\phi = 0$ in the quasi-periodic potential. The values of the parameters are $t = 1$, $d = t/6$, $\mu = 3d - 4t$, $B_y = 0$.

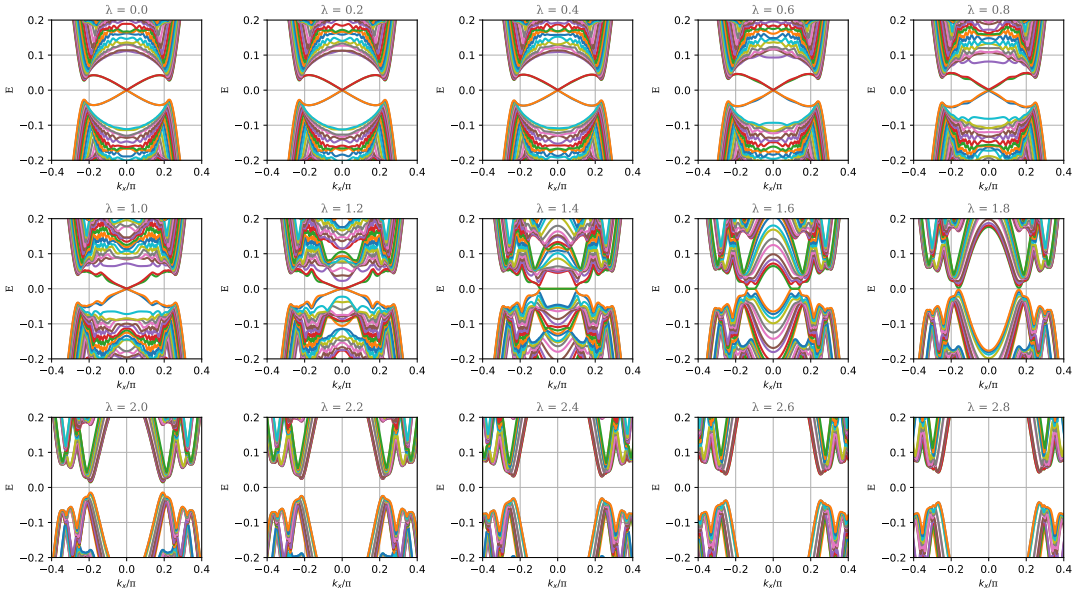

Figure C.2: Energy spectrum evolution for a system with 76 sites in y and edges at $y = 0$ and $y = 75$ for different values of λ as a function of k_x, for $\phi = 0$ in the quasi-periodic potential. The values of the parameters are $t = 1$, $d = t/6$, $\mu = 3d - 4t$, $By = 0.5d$.

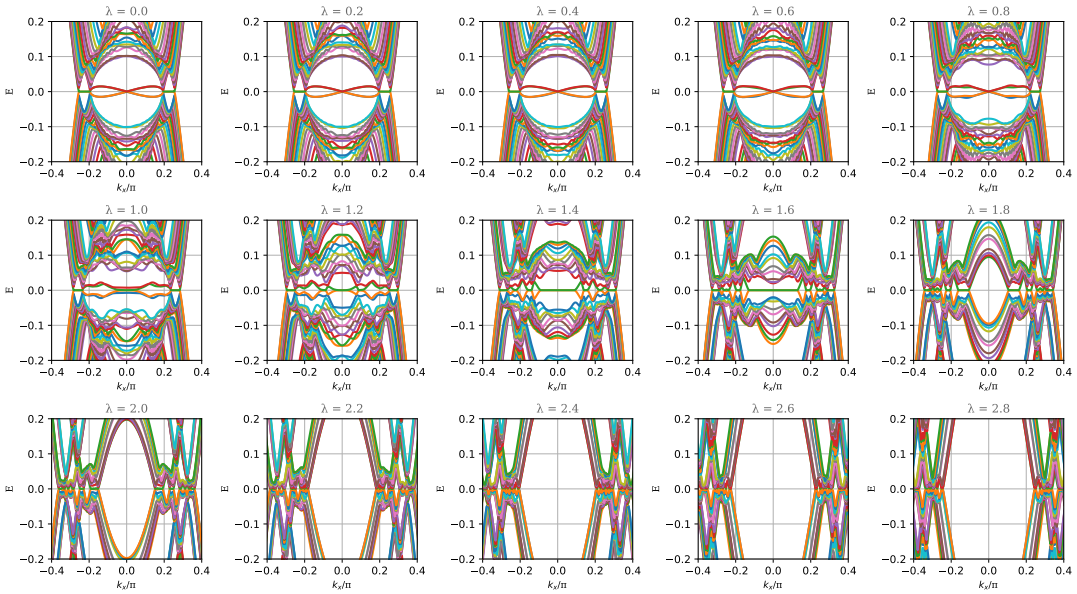

Figure C.3: Energy spectrum evolution for a system with 76 sites in y and edges at $y = 0$ and $y = 75$ for different values of λ as a function of k_x, for $\phi = 0$ in the quasi-periodic potential. The values of the parameters are $t = 1$, $d = t/6$, $\mu = 3d - 4t$, $B_y = d$.

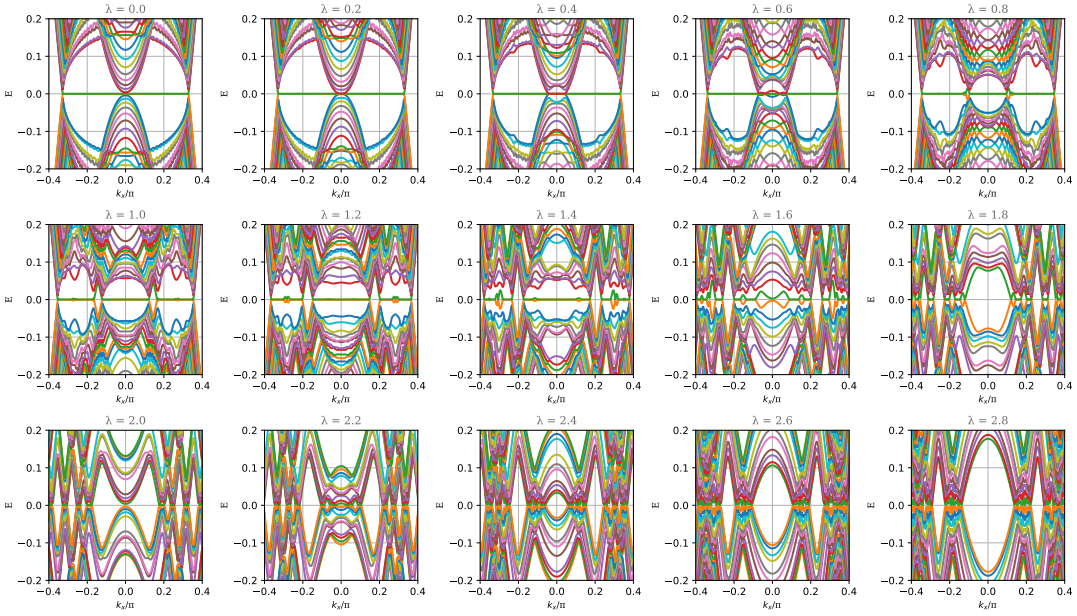

Figure C.4: Energy spectrum evolution for a system with 76 sites in y and edges at $y = 0$ and $y = 75$ for different values of λ as a function of k_x, for $\phi = 0$ in the quasi-periodic potential. The values of the parameters are $t = 1$, $d = t/6$, $\mu = 3d - 4t$, $B_y = 3d$.

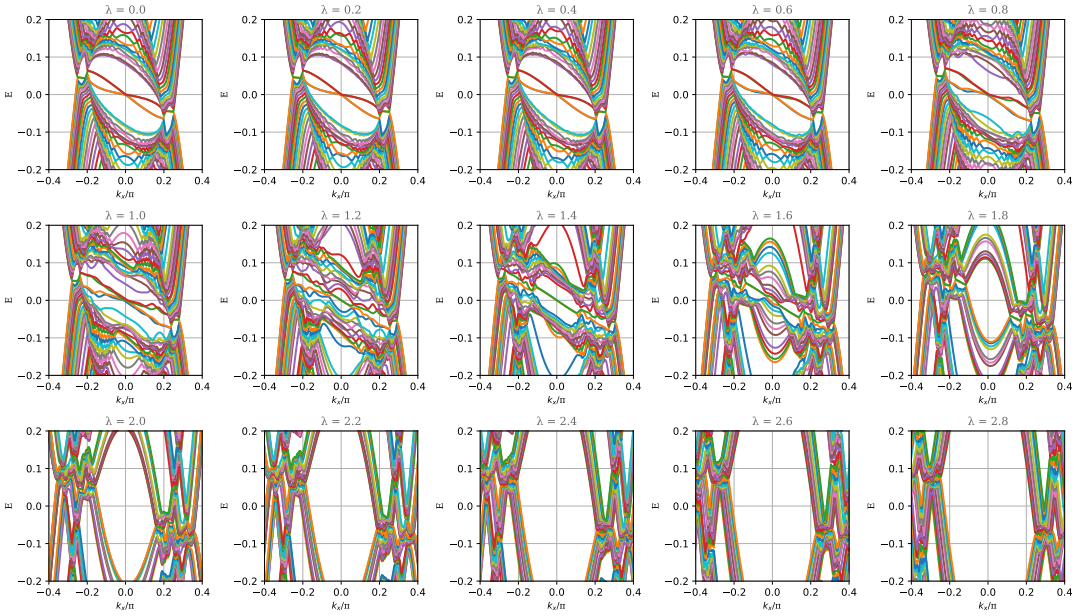

Figure C.5: Energy spectrum evolution for a system with 76 sites in y and edges at $y = 0$ and $y = 75$ for different values of λ as a function of k_x, for $\phi = 0$ in the quasi-periodic potential. The values of the parameters are $t = 1$, $d = t/6$, $\mu = 3d - 4t$, $B_y = d$, $\alpha = 0.2d$, $\Delta_s = 0.5d$.

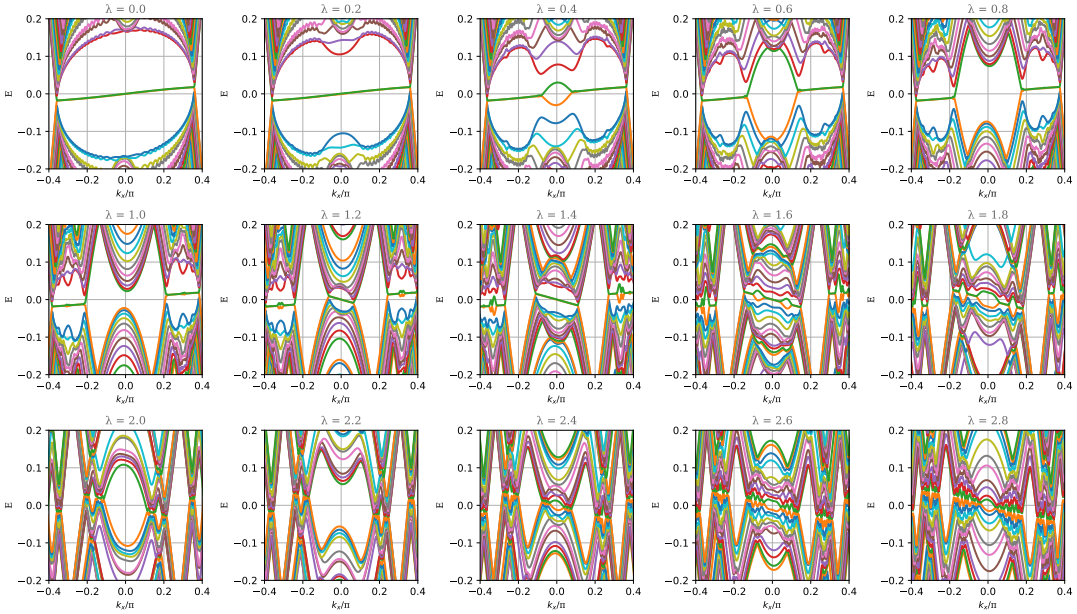

Figure C.6: Energy spectrum evolution for a system with 76 sites in y and edges at $y = 0$ and $y = 75$ for different values of λ as a function of k_x, for $\phi = 0$ in the quasi-periodic potential. The values of the parameters are $t = 1$, $d = t/6$, $\mu = 3d - 4t$, $B_y = 4d$, $\alpha = 0.2d$, $\Delta_s = 0.3d$.